2021

The Investigation of the Underlying Microstructure Associated with Fracture Features in 6061 Cold Sprayed Aluminum

Justin White
University of North Florida, n00973902@unf.edu

“The Investigation of the Underlying Microstructure Associated with Fracture Features in 6061 Cold Sprayed Aluminum”

By

Justin White

A thesis submitted to the School of Engineering

in partial fulfillment of the requirements for the degree of

Master of Science in Mechanical Engineering

University of North Florida

COLLEGE OF COMPUTING, ENGINEERING, and CONSTRUCTION

April 2021

The thesis "The Investigation of the Underlying Microstructure Associated with Fracture Features in 6061 Cold Sprayed Aluminum" submitted by Justin White in partial fulfillment of the requirements for the degree of Master of Science in Mechanical Engineering has been

Approved by the thesis committee: **Date**

_____ _____

Dr. Paul Eason

Thesis Advisor and Committee Chairperson

_____ _____

Dr. Stephen Stagon

_____ _____

Dr. Grant Bevill

Accepted for the School of Engineering:

_____ _____

Dr. Osama Jadaan

Director of the School of Engineering

Accepted for the College of Computing, Engineering, and Construction:

_____ _____

Dr. William Klostermeyer

Dean of the College

Accepted for the University:

_____ _____

Dr. John Kantner

Dean of the Graduate School

Dedication

This work is dedicated to my father and grandfather Jeffrey P. Levine and Leeman A. White.

Acknowledgements

I would like acknowledge Dr. Albina Mikhaylova and Dr. Brian Wingender for their continued personal and professional support. I would also like to acknowledge the faculty and staff of the mechanical engineering department at the University of North Florida who have help and guided me along this journey. The ride has been great.

Symbols and Abbreviations

ARL – ARMY Research Lab

AR – As Received

ASTM – American Society for Testing and Materials

CS – Cold Spray

DE – Deposition Efficiency

HAGB – High Angle Grain Boundaries

HDR – High Deformation Regime

HVOF – High Velocity Oxygen Fuel

IPD – Interim Deformation Regime

ITAR – International Traffic in Arms Regulations

JCPDS-ICDD - Joint Committee on Powder Diffraction-International Centre for Diffraction Data

LAGB – Low Angle Grain Boundaries

LDR – Low Deformation Regime

MDR – Medium Deformation Regime

MSERF – Materials Science and Engineering Research Facility

PM – Powder Metallurgy

SE – Secondary Electron

SEM – Scanning Electron Microscope

SPD – Severe Plastic Deformation

UFG – Ultra Fine Grain

XRD – X-Ray Diffraction

Table of Figures

Abstract

Cold gas dynamic spraying more commonly known as cold spray is a process currently used for restoration, re-tolerancing, and application of coatings. With additional resources allocated towards the development of a through process model aimed at predicting the properties of bulk material produced via the Cold Spray process, more lab testing and investigation must be done to capture the effects of the varying microstructure in CS materials. The properties of ultra-fine-grained materials are derived from data collected from coarse grained materials and processes that do not accurately capture the effects as elevated strain rates and ultra-fine-grained materials. The lack of property data in the is made worse by the complete absence of studies on the fracture behavior of bulk CS components.

This study aims to investigate the underlying microstructure and its effect on fracture morphology in cold sprayed 6061 Al. Samples excised from bulk consolidated material were subsequently subjected to low temperature heat treatment for various time lengths prior to characterization to gain understanding of the possible benefits of low temperature heat treatment. After heat treatment samples were notched and subjected to mode 1 failure. Microstructure is investigated through metallographically prepared samples as well as on bulk samples in orthogonal directions as well as perpendicular cross sections of fracture surfaces. The correlation of fracture features, microstructure, and electron back scattered diffraction techniques presented in the research are shown to provide a method for optimizing the investigation of the failure behavior close to primary, secondary, and tertiary cracking. It was

observed that low temperature heat treatment of 6061 CS aluminum drives recrystallization within the regions of higher deformation in the microstructure and alters crack path propagation through these fine-grained regions. These fine-grained regions coarsen into textured regimes after low temperature, resulting in failure occurring along the boundaries of high misorientation between the textured regions.

Chapter 1: Introduction

Aluminum (Al) and its alloys are commonly utilized materials in engineering design and have been heavily implemented in aero-space, applications due to their formability, low density and high relative strength. The Cold gas-dynamic spray process, more commonly known as Cold Spray (CS) is a method of depositing pre-processed powder particles onto a substrate through high velocity particle-substrate and particle-particle impact [1]. This production methodology is known to produce coatings which exhibit bonding through the creation of adiabatic shear jets and mechanical adhesion via inter-particle impingent [2]. Since its discovery in mid-1980's many investigations into the structure-process-property relationship of numerous metals including Al and its alloys have been conducted revealing some of the benefits as well as limitations of the CS production methodology [1]-[5]. Face centered cubic (FCC) materials and aluminum are of great interest due to their low densities, passivating oxide layers, and good workability. The bulk aluminum microstructure imparted by the CS process produces potentially desirable nano-scaled grains [6]-[8]. The rise of additive manufacturing techniques, and more specifically solid-state metal additive manufacturing processes have brought cold spray back into the forefront of scientific advancement. Currently CS Al is used in accordance with military specification and guidelines for repair and restoration of dimensional tolerances on magnesium components within the aerospace industry, but more research must be conducted to fully understand the holistic behavior of CS aluminum bulk materials [9], [10]. Until recently most of the research into cold spray has been on particle impact and bonding through modeling [5], [11]-[13]. A

Department of Defense initiative into applicable CS technologies has pushed researchers into development of a through-process model for CS to help produce consolidated materials with predictable microstructures and material properties. The primary goal of the model is to predict the microstructural properties of CS material however, the models is unreliable when used in conjunction with the extreme strain rates of those used in the CS process [5].

Few studies into the tensile behavior of bulk CS materials exist with even less about bulk Z direction properties. This study aims to build off prior works conducted by the research group in the XY direction and delves into the as-sprayed direction of bulk CS deposited 6061 aluminum samples heat treated to 200°C for various time increments. The as-sprayed direction is identified as the z direction which is parallel to the CS stream and perpendicular with the substrate. The investigation intends to correlate microscopic fracture features to the non-homogenous bulk microstructures observed through SEM micrographs and grain orientation maps produced through Electron Back Scattered Diffraction (EBSD). Mechanical evaluation of microstructural regimes within the CS microstructure are conducted through microhardness array indentation to support conclusions, with the intent to provide initial insight into the microstructural features associated with bulk material failure after low temperature heat treatment.

Chapter 2 contains all the relevant literature with respect to the project including structure process properties relationship, information about 6061 aluminum, the effects of heat treatment, and current information regarding the fracture surface of wrought and CS 6061 aluminum. Chapter 3 describes the methodology of the sample preparation and instrumentation

used for the study. Chapter 4 is the results and discussion section and chapter 5 is the conclusion and future works of the study.

All preparation and experimentation of CS deposited samples received from the ARMY research lab (ARL) were conducted at the University of North Florida's (UNF) Materials Science and Research Facility (MSERF) in accordance with ITAR compliance and regulations [14] .

Chapter 2: Literature Review

2.1 Cold Spray

2.1.1 Process

CS process has primarily been utilized to provide coatings for surface repair, wear resistance, and self-lubricating coatings [15]-[17]. More recently CS has been utilized as a dimensional tolerance restoration process for magnesium components primarily utilized by the U.S. military. The application of CS technology presents a unique set of benefits which include coupling dissimilar materials without the introduction of undesirable intermetallic phases , reduction in overspray eliminating the need for masking and the ability to produce thick coatings [18] with low porosity (99%), and high deposition efficiency (DE) [11], [19]. The CS process also offers a novel approach to dimensional tolerance restoration and preventative maintenance along with the benefits added from increased material deposition rates [20].

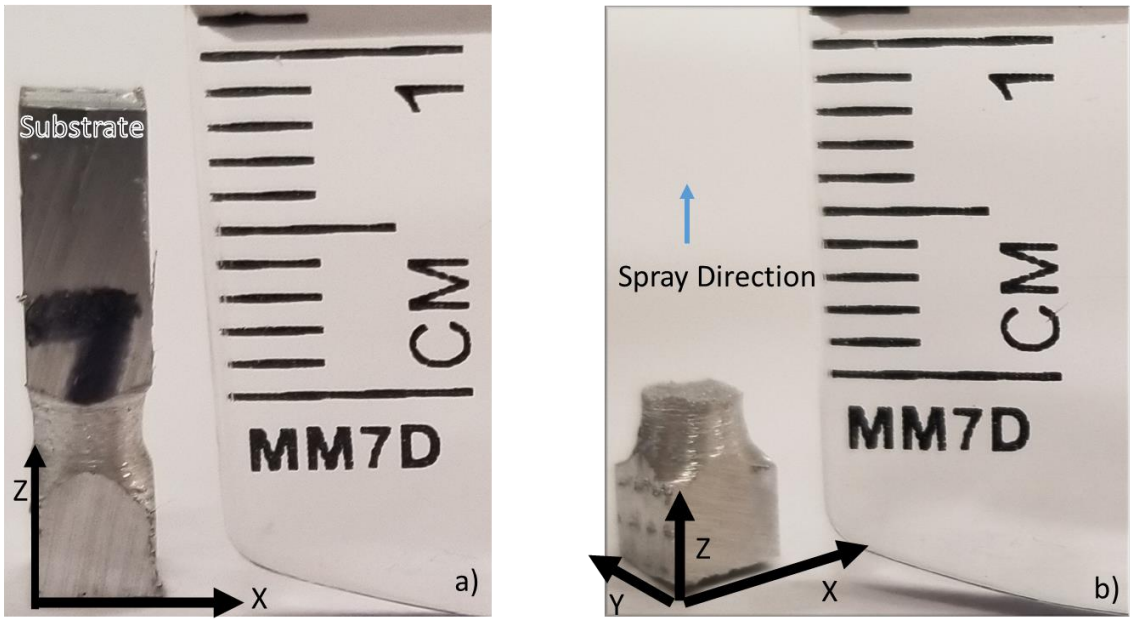

Figure 1 Sample during the sample production process. Image a) show notched samples prior to fracture and show the sample orientation. Image b) shows a fractured sample and shows the orientation of the sample with respect to the spray direction

A simplified version of the CS apparatus is shown in Figure 2, where critical aspects of the process are highlighted to shows the areas in which the process parameters for CS can be altered. These process parameters include the critical velocity, process gas, and temperature all of which influence the resulting microstructure produced from the CS process.

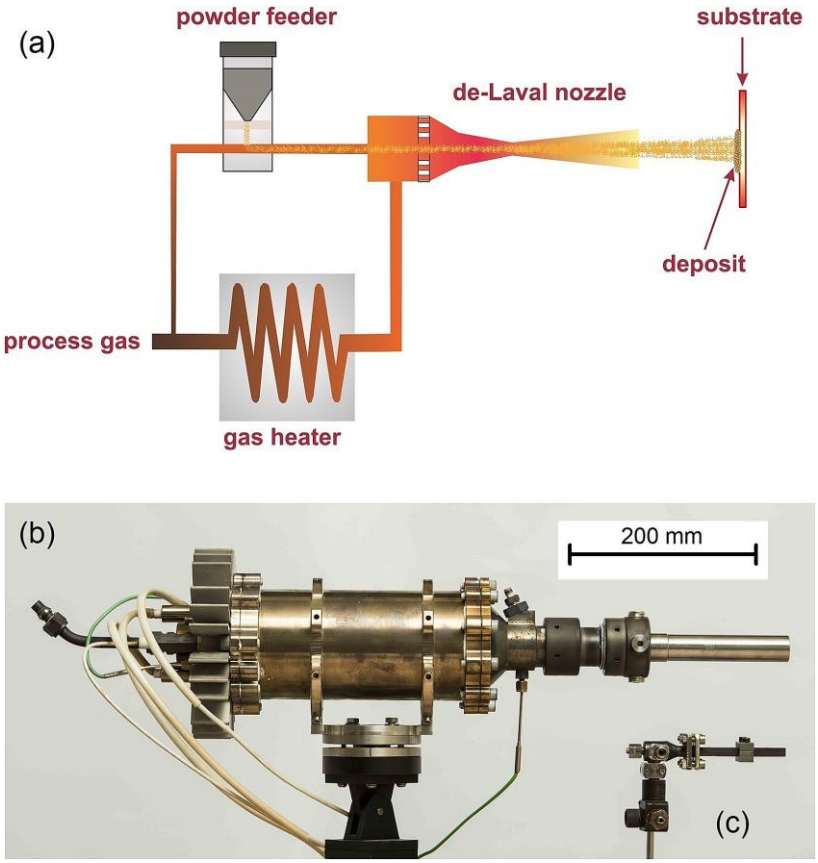

Figure 2 An overview of the cold spray system with a) illustrating a simplified schematics of the main components that comprise the original system highlighting critical process parameters, b) a commercialized cold spray gun/nozzle, designed at Helmut Schmidt University, and c) a model of the original gun/nozzle developed by Anatolii Papyrin. The guns labelled (b) and (c) are in the same photo and have equal distances from the camera [21].

Literature shows that the microstructures and material properties produced during CS are intrinsically linked to the process parameters [1], [3], [13], [19], [22]. Process parameters heavily influence the microstructural development during the CS process by influencing bonding between the particle-substrate bonding, particle-particle bonding, porosity, and deposition efficiency [5], [23], [24].

The De Laval Nozzle (Figure 2) is a converging-diverging nozzle that allows subsonic fluid to accelerate to supersonic conditions by taking advantage of geometry transitions in

conjunction with shockwaves [25]. Originally designed to increase the velocity of steam jets produced for impulse steam turbines, the technology was adopted in the mid-20th century by the aerospace industry where it found its most notable success as a nozzle for modern rocket engine propulsion [26]. Calculations for the process parameters are typically taken before entering and after exiting the De Laval nozzle where P_0 and P represent the stagnation and exit pressures, respectively. This upstream configuration entrains the process powder into the gas stream prior to entering the de Laval Nozzle, providing the particles a longer time to accelerate. Issues with respect to flow-ability arise as geometric constraints at the choke point of the nozzle which causes an increase of interparticle collisions and limit the material deposition rates [27].The downstream implementation removes the possibility of obstructing the nozzle but can limit the ability to pre-heat the process powder which reduces the overall energy captured [1].

Deposition efficiency, the mass ratio of material deposited on the substrate to material sprayed, is a widely used quantitative measurement due to the ease of pre and post spray mass measurements [28]. This measurement is directly related to the critical velocity range at which deposition begins and ends as well as potential spray production cost. Porosity is the second quantitative measurement, as porosity is directly related to the thermal, electrical, and mechanical properties of the resultant coating or bulk structure [2], [4]. The intrinsic relationship between deposition velocity and quantitative measurements can be seen below in Figure 3.

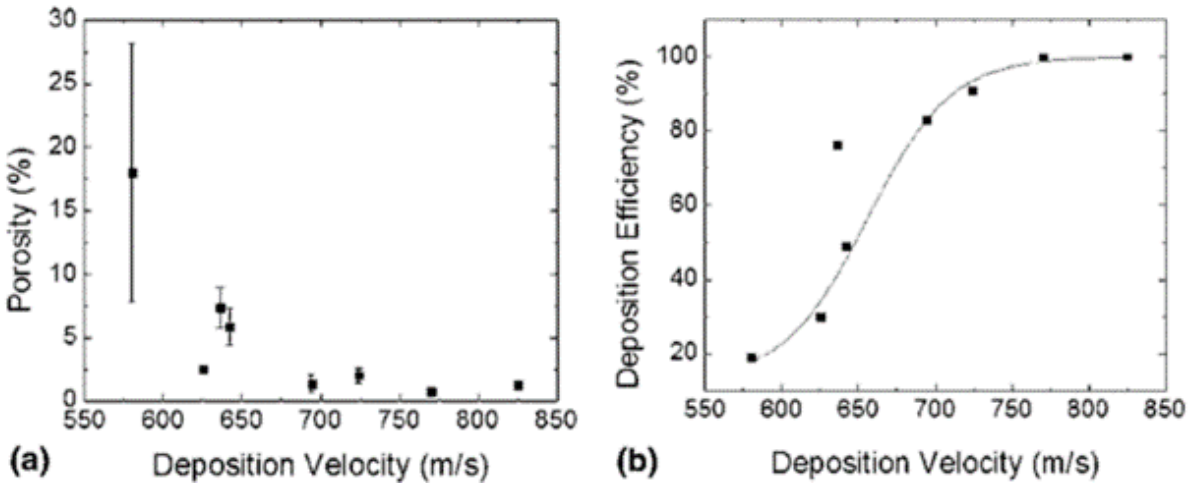

Figure 3 The porosity and deposition efficiency as a function of deposition velocity for commercially pure titanium [4].

The critical velocity for a given particle is defined as the velocity that a particle must achieve such that upon impact with a substrate the particle adheres through severe plastic deformation (SPD) rather than eroding of the substrate surface as seen in the process of shot peening. The critical velocity is influenced by material density, particle size, and particle morphology. Smaller diameter particles accelerate faster in the gas-solid two-phase flow and are also capable of achieving velocities greater than the critical velocity. Although smaller particles tend to achieve a higher impact velocity they are decelerated before impact by the presence of a bow shock wave which is inversely proportional to the diameter of the particle as well as exhibiting issues with respect to retained internal strain energy as particle size decreases [29]. Particles of lower density require less energy to accelerate and tend to achieve higher velocities. Research shows that particle morphology has a strong impact on critical velocity as particles of irregular morphology tend to accelerate slower due to drag [30]-[32]. Particles that do not achieve the necessary velocity for deposition can become entrapped within the coating. Without

enough kinetic energy particles undergo little or no SPD which should be visible in micrographs of the fracture surface. The optimal particle size for deposition can be seen in Figure 4 within the deposition window, or the particle size in which particle velocity exceeds critical velocity. The average particle sized used during production of the CS consolidated bulk was approximately 35 µm [33].

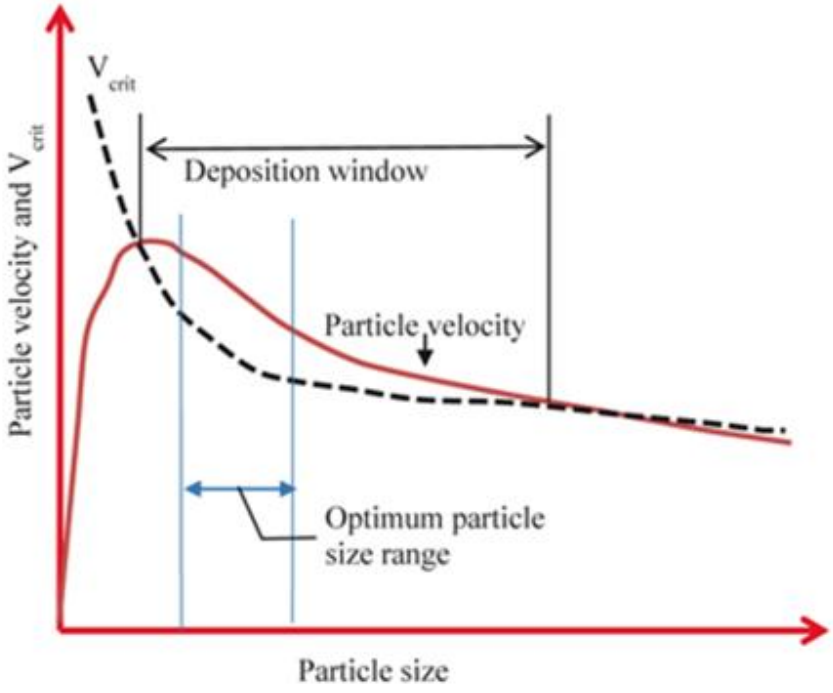

Figure 4 Velocity vs particle size compared to the velocity required to achieve deposition. Only a small portion of feedstock powder can attain the critical velocity [27].

The second phase of the two-phase flow is the process gas which should accelerate the feedstock powder without adversely influencing the material before impact. While the most cost-effective choice is atmospheric air, the presence of oxygen allows for the formation of oxides on the process powder surface, resulting in reduced deposition efficiency or increased porosity. Therefore, the use of an inert gas is preferred for the CS process, resulting in either the

selection of helium or nitrogen. Currently, helium produces superior coatings as compared to its heavier counterpart but has been cost prohibitive leaving nitrogen as a more feasible and cost-effective alternative [1], [3], [15], [28].

Thermal softening of the material encourages deformation by increasing the internal energy of the particles prior to impact. Operation at elevated temperatures, but well below the melting point of the feed stock material, eliminates problems associated with oxidation as well as phase transformation as seen in other processes such as thermal spray or high velocity oxygen fuel (HOVF) spray [27]. During conventional thermal spraying processes, the feedstock material experiences extreme temperature changes resulting in full or partial melting the precursor materials. This promotes the growth of oxides that becomes entrained into the film, or the development of undesirable intermetallic species through temperature induced phase transformations. Preheating the feedstock increases the internal energy of individual particles which is preferential for deformation and creation of peripheral jets theorized to provide metallurgical bonding similarly seen in processes like explosive welding [34]. Figure 5 shows how gas temperature and particle velocity influence the deposition efficiency when utilizing both helium and nitrogen as the process gas.

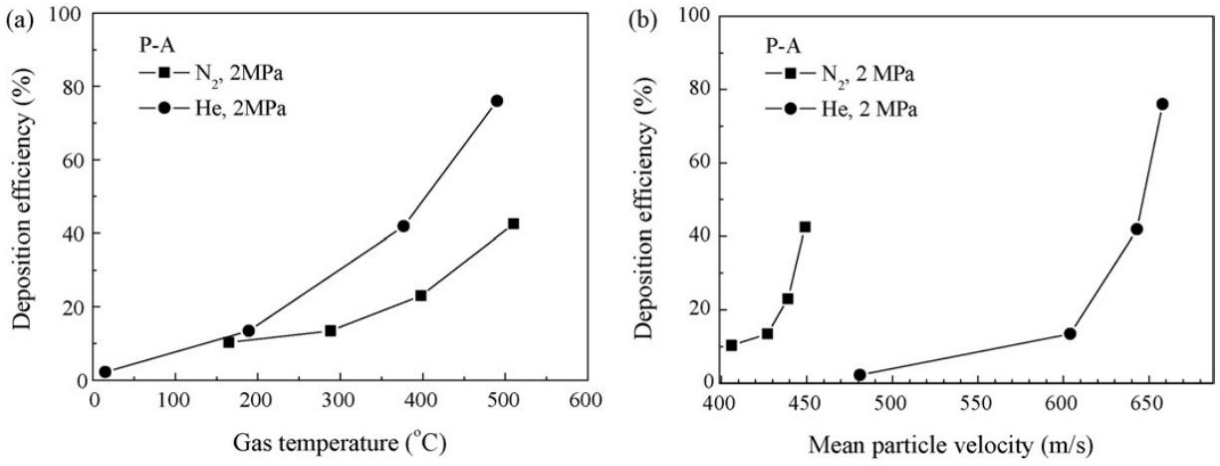

Figure 5 Effect of gas temperature and type on deposition efficiency and (b) change in deposition efficiency with mean particle velocity [35].

2.1.2 Microstructure of Cold Sprayed Materials

Micrographs produced from scanning electron microscopes (SEM) showing cross sections from within the bulk of a CS sample highlight the nature of the nonhomogeneous microstructure imparted by the CS process. The secondary electron (SE) micrographs taken in the XY direction, orthogonal to the direction of spray, show the characteristic morphology resulting in the creation of three grain size regimes identified in Figure 6 as low (LDR) deformation regimes, medium (MDR), and high (HDR) which are labeled 1,2, and 3 respectively [33].

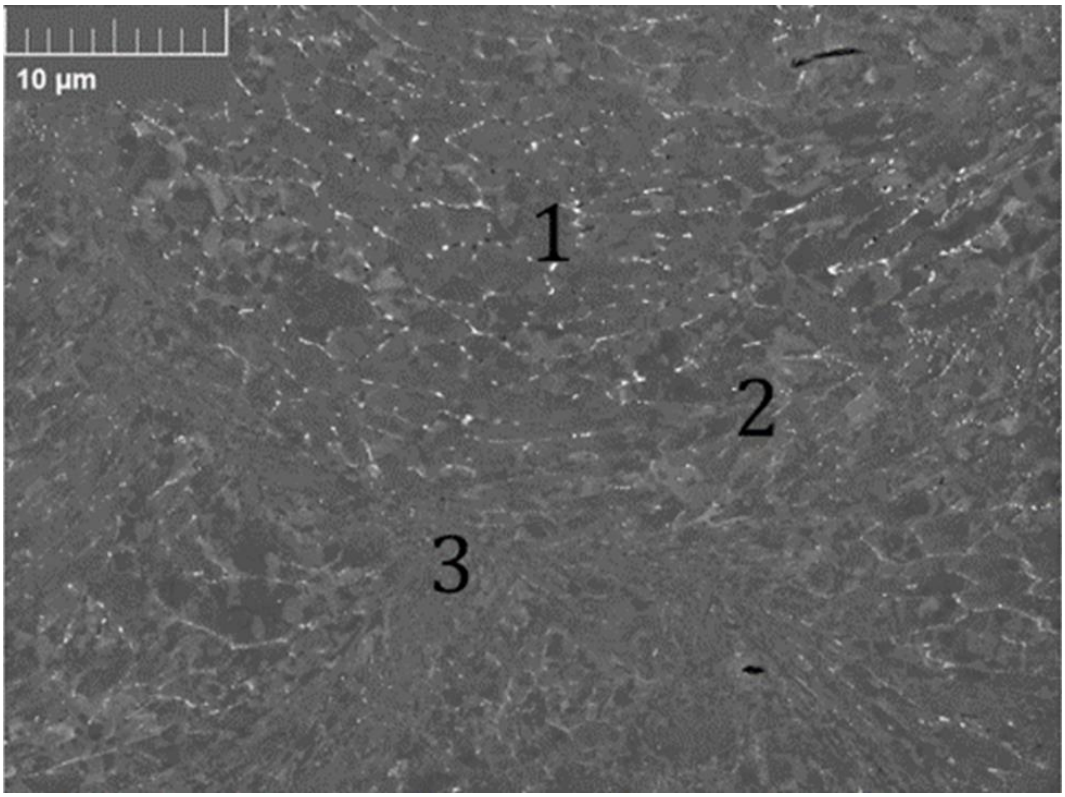

Figure 6 SEM micrograph showing the three distinct regions produced by the CS process. 1) low deformation (LDR) 2) medium (MDR) deformation 3) (HDR) high deformation [33].

Extreme pressure, temperature, and stacking fault energy dictate the average grain size as well as the degree of mechanical disorientation, but are heavily influenced by particle impact [36]. Upon impact with a free surface, the flattening of the particle tends to produce three characteristic grain regimes. The low deformation areas are typically seen proximal to the point of orthogonal impact. Low deformation zones are most characteristic of the feed stock material as it experiences the least amount of mechanical disruption. Medium deformation areas are characterized by moderate mechanical disruption, and the smallest of the grains are seen in the high deformation areas near the initial impact and jetting sites which are reported as being sub-micron in nature [33], [37], [38]. Adiabatic shear instability, extremely localized heating due to

plastic deformation at high strain rates, and the SPD phenomenon seen at extremely high strain rates ($\dot{\varepsilon}$) are believed to be responsible for the creation of UFG through extreme mechanical disruption of the microstructure [12].

Particle interaction can be divided into two categories Particle-Interface interaction, in which the incoming feed stock particle impinges upon the substrate surface, or the Particle-Particle interaction, in which the incoming feedstock particle makes direct impact with a previously deposited particle [39], [40].

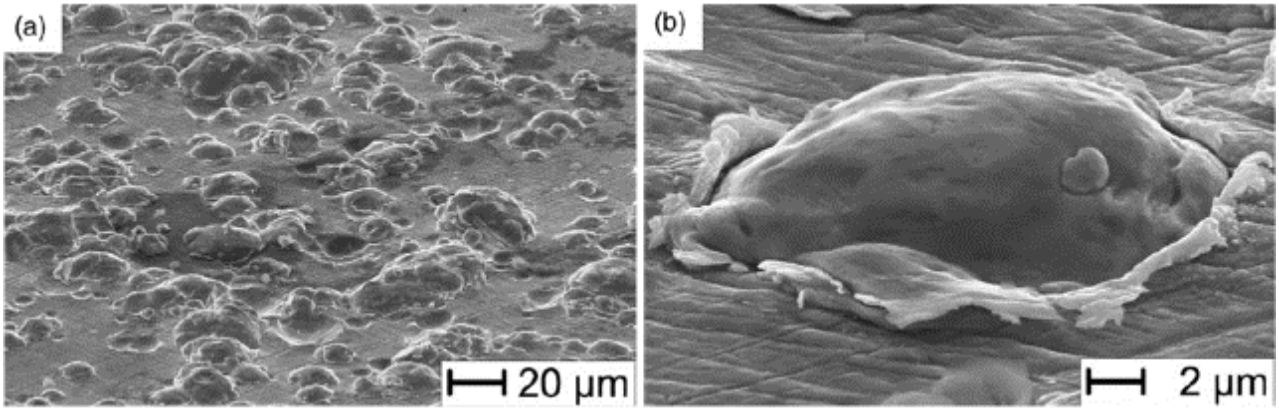

Figure 7 SEM micrographs of impacted copper particle onto a copper substrate. The formation of jets which indicate metallurgical bonding can be seen [13].

One aspect of CS bonding is the mechanical interlocking of impinged particles that occur as particles impact the substrate and previously deposited particles. This overlapping results in the intertwining of particles which provides the primary source of mechanical adhesion or keying. Upon impact particles embed themselves then tend to flatten out often extruding material out from around the peripheral edges producing “jets” commonly associated with strong metallurgical bonding.

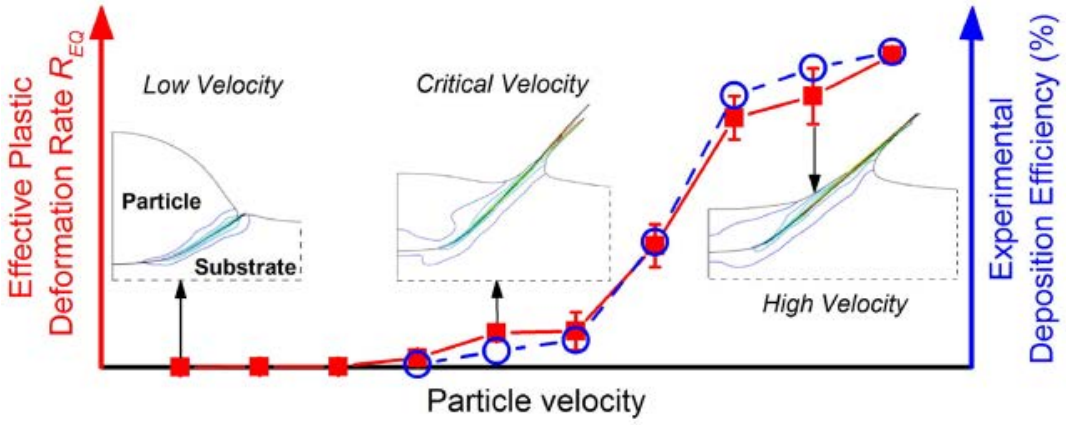

Figure 8 Graphically shown is the relationship between critical velocity and the creation of material jetting [11].

Adiabatic shear stress has been identified as a significant mechanism by which strong metallurgical bonds form and is one of the phenomena responsible for creation of the material jetting. Upon impact with the surface, extreme localized strain at the point of initial impact produce an outward moving layer of higher energy material which is ejected radially from the center of impact towards the edges. Results from research in strain localization indicate the rapid increase in temperature attributed with the formation of jets [12].

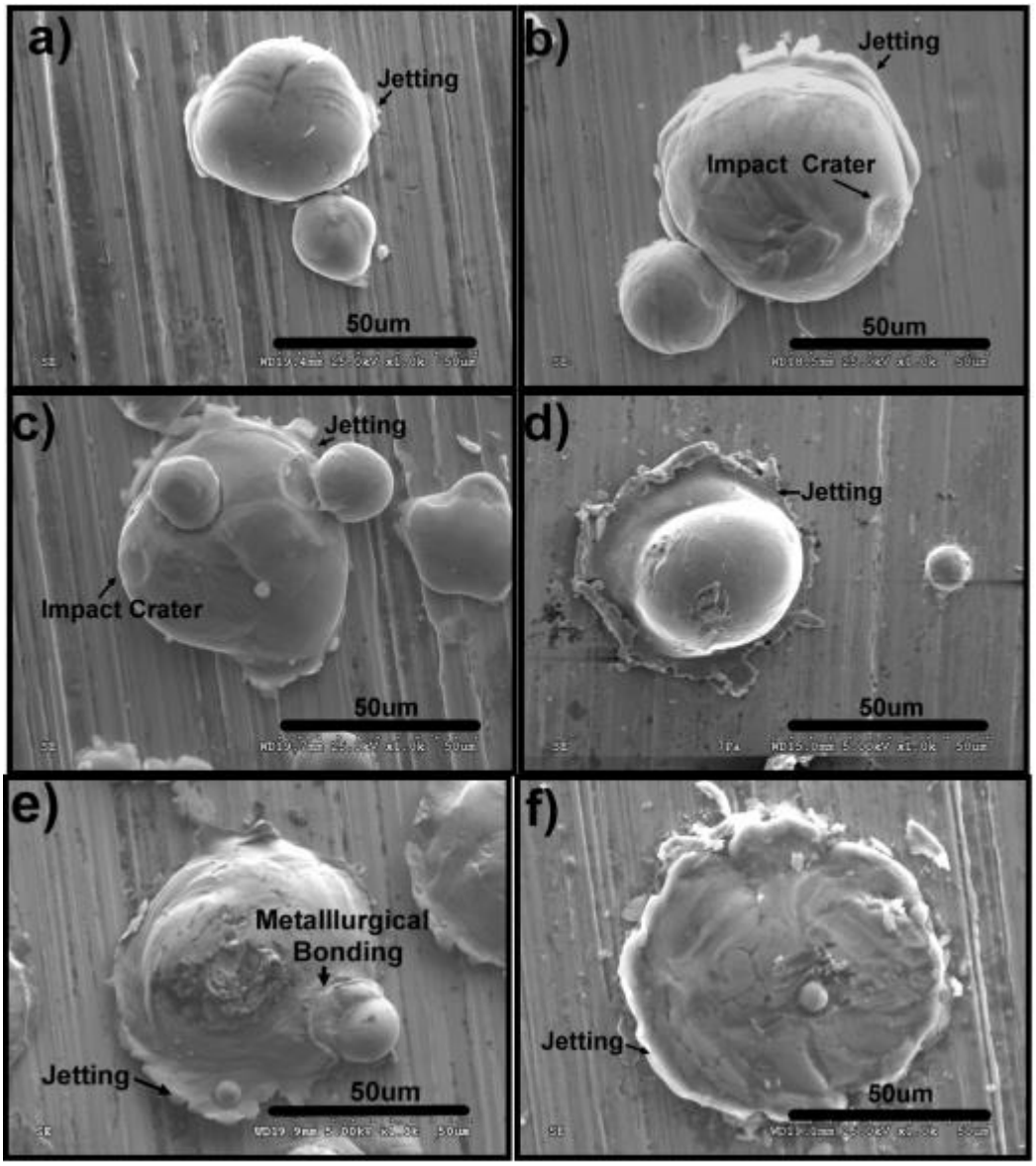

Figure 9 SEM micrographs of Cp Ti splats deposited at a) 300°C, 2MPa (580 m/s), b) 300°C, 4MPa (642 m/s), c) 500°C. 2 MPa (724 m/s), e) 750°C, 3MPa (770 m/s) and f) 800°C, 4 MPa (825m/s). Gas preheat, gas pressure, and particle velocity [4].

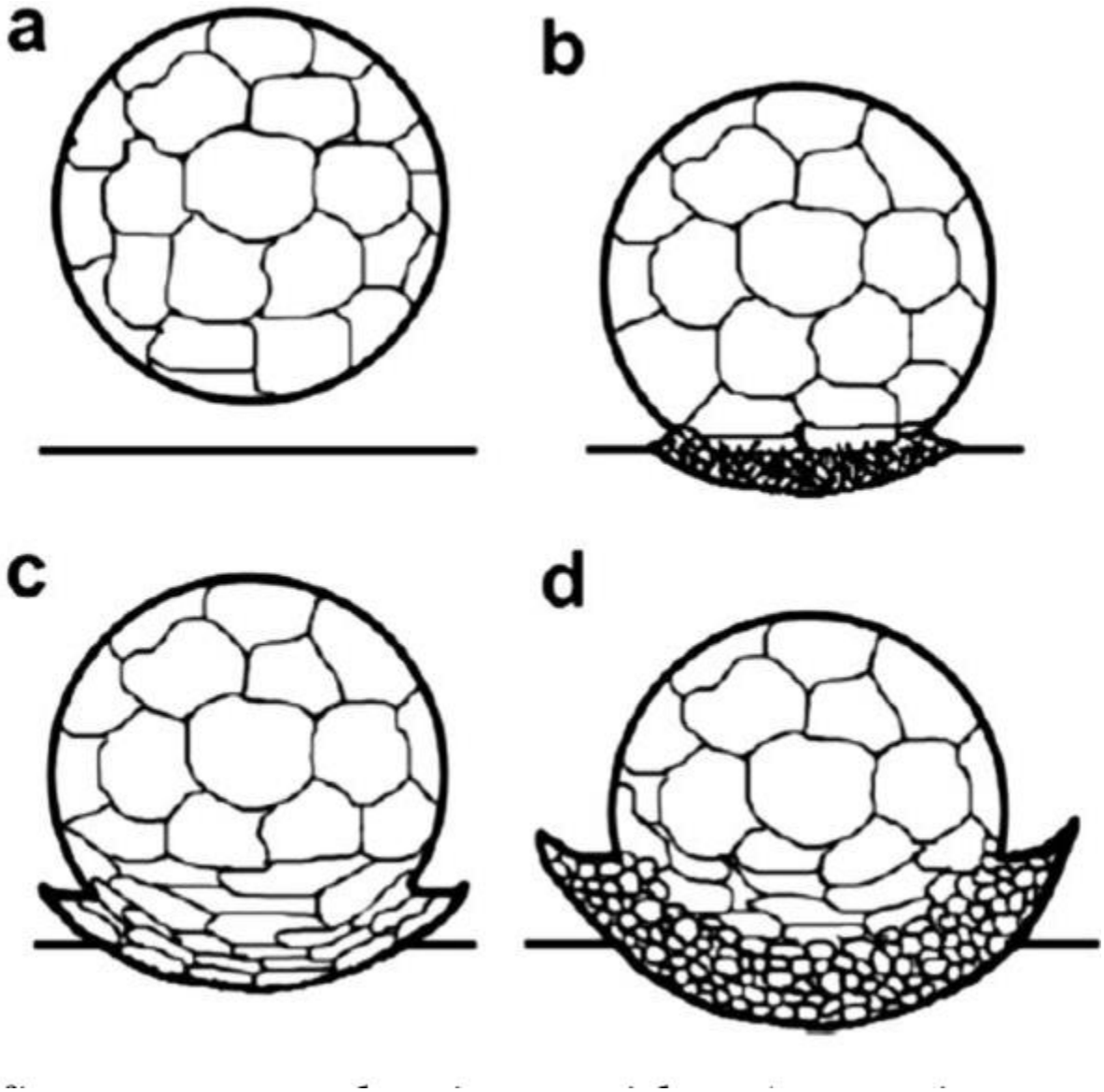

Figure 10 Grain refinement mechanism with a) pre-impact feedstock powder, b) entanglement of dislocations upon impact, c) formation of persistent dislocation cells and re-elongation and d) brake-up, rotation and recrystallization of sub-grains [41].

Prior investigation by the research group into CS 6061 Al has shown a complex microstructure exhibiting a wide range of grain morphologies which can be considered as multimodal. Research into bimodal microstructures provides initial insight into the nature of

materials with complex microstructures such as CS Al which display a wide range of grain size. By incorporating the high strength and toughness attributes of UFG materials with the superior ductility of larger grained counterparts, the bimodal microstructure studies show promise in combining multiple microstructural regimes in order obtain superior strength and toughness with reduced losses to ductility [42]-[44]. Many methods for producing UFG materials exist, but processes limit the quantities of bulk materials produced. The extrusion type processes are typically batch process and produce small amounts of bulk material. The most common extrusion process currently used is equal channel angular pressing (ECAP) which is a technique that is used to create UFG bulk materials through extreme mechanical deformation [45]. In ECAP, small amounts of ductile material are pushed through dies consisting of up to a ninety degree turn in which the material experiences extreme deformation and the UFG microstructure is produced. It is common practice to use extrusion processes in tandem with torsional methods to enhance the mechanical disruption of the microstructure. Extrusion processes can produce bulk materials that may be suitable in the production of UFG structured wire [46]. Rolling techniques typically involve passing ductile material through a series of guide and feed rollers [37]. Accumulative roll bonding requires the use of surface treatments and degreasing to bond stacks of material through a series of successive decreasing rolling operations. Rolling techniques provide a suitable process for producing UFG bulk sheets [47].

2.1.3 Mechanical Properties of Cold Sprayed Materials

The Hall-Petch equation is a well-known model used to predict the microstructural effect of average grain size on yield stress. While this model accurately predicts the effects of grain coarsening in large grain materials, the model does not capture the effect of UFG and extremely high strain rates [48], [49]. Differences in simulated data and empirical observation suggest that there is minimum grain size range at which Hall-Petch no longer produces adequate models. Experimental studies conducted by Haque et al into aluminum showed that in sputter created free standing tensile film specimens the Hall-Petch model began to break down at an average grain diameter of 50 nm with similar investigations by Whang et al into CP copper which have confirmed this behavior within the range of 20-30 nm [50], [51]. This reduction in yield strength due to the reduction in average grain size is referred to as the inverse Hall-Petch relationship [52]. The inverse Hall-Petch relationship is accompanied by a sharp decrease in ductility which is theorized to be attributed to the loss of strain hardening mechanisms as grain size decreases [53]. This phenomenon is delineated by a rapid decline in the flow stress of the material, the instantaneous value of stress required to continue plastically deforming a material, suggesting that dislocation pile up is no longer occurring within the grains and dislocation creep along grain boundaries becomes the primary mechanism by which strain energy is alleviated from within the bulk [54].

While some of the literature suggests the rise of the inverse Hall-Petch phenomenon within the UFG grain regime, there still exists some debate as to the grain size related to the

transition as well as the mechanisms by which the Hall-Petch relationship begins to break down. Differences in data collected through experimentation when compared to data produced through empirical modeling could be attributed to sample production number, production processes, and inadequate modeling of metal nano-mechanics [52]. The small population of bulk samples and research across multiple UFG production methodologies lead to lack of confidence in experimental values.

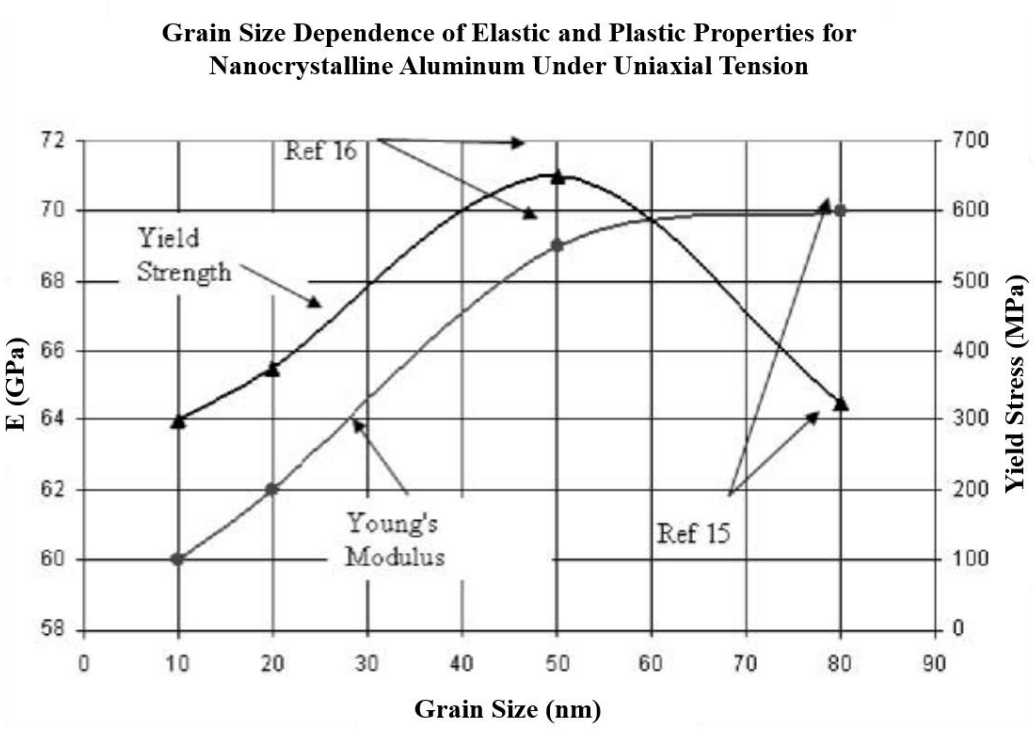

Figure 11 Grain size dependence of the Young's modulus and yield strength of nano-crystalline aluminum under uniaxial tension [51].

The literature does however suggest that the CS microstructure shows areas of high, medium, and low deformation with potential varying values of hardness consistent with the amount of mechanical deformation associated with their respective regimes [23], [33]. Increased

hardness or resistance to penetration has been seen in many UFG microstructures and has been attributed to an increase in surface defects or grain boundaries [24], [48], [55] . Previous investigation by the research group into the microhardness of bulk CS materials have shown slight differences in Vickers microhardness with respect to heat treatment time. The AR samples produced the highest average hardness (~105HV) and 100HR samples producing the least (~78HV). little work has been done to delineate the portion of microstructural regime captured within the individual microhardness indent, but mechanical evaluation of the microstructure can help support correlations of microscopic fracture features to potential microstructural regime. Similar mechanical testing has been conducted on Ti coatings which shows differences in the microhardness of coatings, but no significant variations within the coating [4].

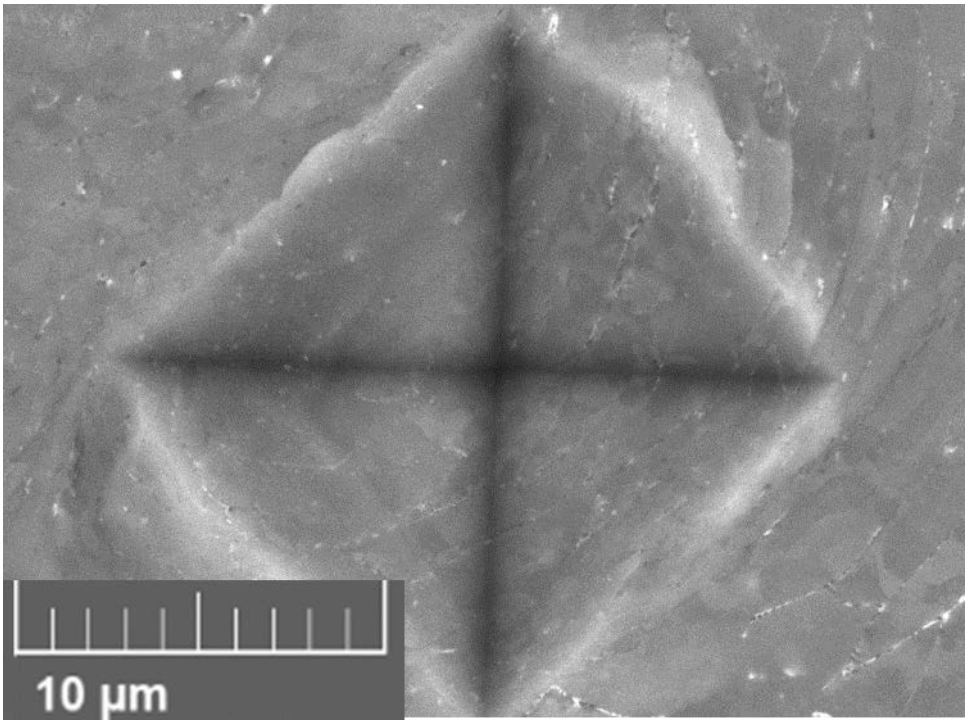

Figure 12 Taken in SE mode is a microhardness indent capturing multiple grain size regimes with multiple sub-grains visible within the indent. No microstructural information was taken prior to indentation. [33].

2.2 Aluminum Powder Used for Cold Spray

The process of powder metallurgy (PM) has existed since the end of the 18th century, but initially the high cost of powder production limited its uses. Today PM is used for a broad range of applications in many research and industrial processes such as 3D printing as well as the growing use in CS technology. Materials that do not exhibit plastic deformation, non-reversible change of shape in response to mechanical stimuli, cannot be used in the CS process therefore

traditional CS materials including copper (Cu), Nickle (Ni), titanium (Ti) and aluminum (Al) [31], [54], [56], [57]. Aluminum and its alloys are of specific interest because of their lower densities, relatively low critical velocities, and a passivating oxide layer (Al_2O_3) that inhibits the formation of oxides and increases corrosion resistance [54], [58]. The 6xxx series of Al alloys are identified by their primary alloying constituents silicon (Si) and magnesium (Mg) with 6061 specifically be tabulated below.

Table 1 the chemistry of 6061 with its allowable weight percentages of constituent elements.

Primary	Min Wt.%	Max Wt.%		Secondary	Min Wt.%	Max Wt.%
Mg	0.8	1.2		Cr	0.04	0.35
Si	0.4	0.8		Zn	0	0.25
Cu	0.15	0.4		Ti	0	0.25
Fe	0	0.07		Mn	0	0.15

The Al process powder used during CS is intrinsically linked to the material properties of the resultant coating or bulk sample. To achieve the required critical velocity for deposition, CS relies on finely processed powders ranging from 20-30 microns in diameter which are smaller than those used in conventional spray coating methods [1], [27]. Many methods for production of micron scaled particles exist, including gas atomization, cryo-milling, and spray drying. Gas atomization of Al produces the most spherical particles which are the preferred geometry for creating Al 6061 process powder or for modeling and research applications [59]. During atomization, liquid metal is disrupted by the flow of high-pressure inert gas to form droplets that solidify into individual particles. This rapid solidification process (~10^4 °C/s) produces the small fine-grained powder required for the CS process.

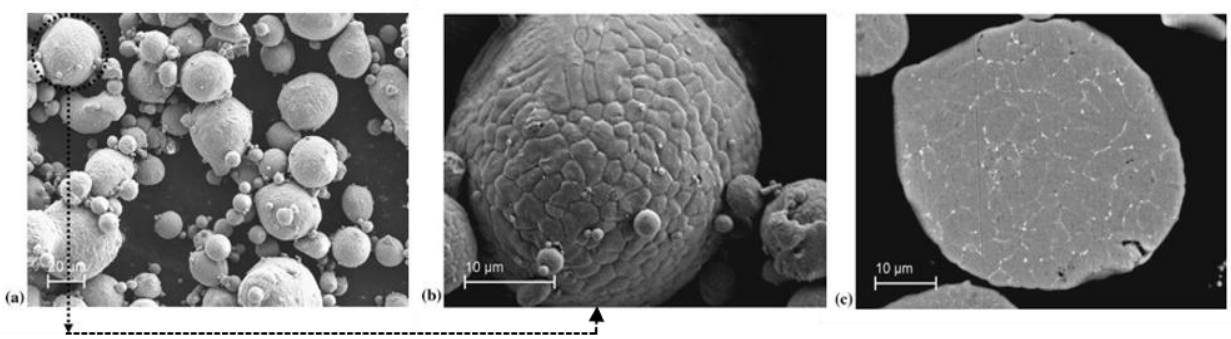

Figure 13 SEM micrographs of typical as-received 6061 gas atomized aluminum (a) low magnification micrograph of particle size, distribution and spherical morphology,(b) rough sub-micron grained surface of ~30 micron particle, (c) cross section of a similarly sized particle reviling the internal of the sub-micron grain structure and nature of the GB solutes [23].

In Figure 13 (b) the surface morphology of the approximately 30µm 6061 Al powder particle can be seen, the micrograph shows the submicron grains that make up the particle. The constituent alloying elements can also be seen along the grain boundaries (GB) in 6 c) which consists primarily of Mg, Si, Cu, and Fe. These small grains are mechanically disrupted upon impact, with areas that experience the greatest amount of deformation producing the UFG (Ultra Fine Grain) microstructure as defined by region 3. Smaller particles seen in the micrograph are known as satellite particles and are a byproduct of the gas atomization process. Figure 14,below, shows micrographs taken by the research group of as received (AR) 6061 aluminum process powder which show similar morphological characteristics to the gas atomized powders characterized by other groups [23].

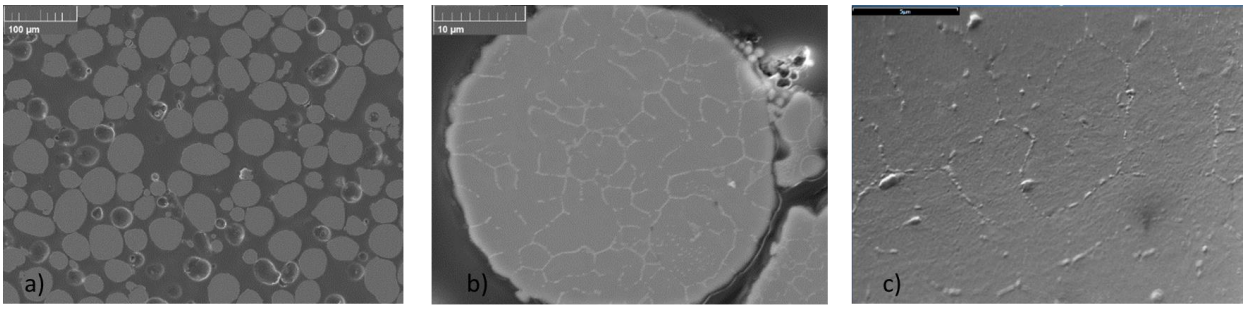

Figure 14 Cross-sections from as-received 6061 Al process powder a) shows low magnification micrographs of the average size, morphology and distribution b) interior granular structure of spherical ~ 30 micron particle, c) high magnification micrograph of micron sized internal grains and solute segregation on alloying constituents on BG .

2.3 Effects of Heat Treatment on Cold Sprayed Microstructure

Traditional models that predict the microstructural behavior of metals when exposed to temperatures between $0.4T_m$ - $0.6T_m$ have been the under-pinning of industrial heat treatments (HT), but do not accurately model the grain growth phenomenon seen at the extremely high dislocation densities as is the case with UFG materials [60]. Heat treating of bulk Al CS components allows areas within the bulk the ability to relive areas of extremely high dislocation density after impact through recovery and recrystallization (RXN) [44]. This can be seen through SEM imaging of bulk Al cross sections which show signs of recovery after heat treating at 200°C for various time lengths. Heat treatment effects on the microstructure can also be inferred by an increase in ductile failure mechanisms observed in micrographs of the fracture surface. Previous works on the annealing effects on aluminum microstructures provide insight into the grain growth of the bulk material, but little it still understood about the microstructural evolution of SPD processes [48], [61].

Traditionally, strength and toughness of a material can be increased at the expense of ductility, but ductility can be regained though the process of annealing. Retained internal strain due to the increased dislocation densities within the UFG microstructure are believed to be the driving force that lead to low temperature annealing effects. This phenomenon has been attributed to the abundant presence of smaller grains which have increased surface energy (γ) [62], [63]. Similar phenomenon can be observed in traditional Ostwald ripening of a two-phase solutions and in metallic alloys [64]-[66]. Experiments carried out by various research groups show the characteristic stages of recovery and recrystallization after heat treating samples at 200°C [33], [44], [67].

Recovery is the first portion of the annealing process by which internal strain is relieved as internal point defects self-diffuse to reduce the internal granular strain energy [6], [7]. Studies focusing on UFG materials suggest that the degree of recovery and recrystallization is dependent on the deformation regime, inferring that high deformation regimes are more prone to accelerated annealing effects at lower temperatures [53]. Researchers observed dislocation motion through transmission electron microscopy (TEM) as low as 70°C with more significant observable changes above 150°C [68].

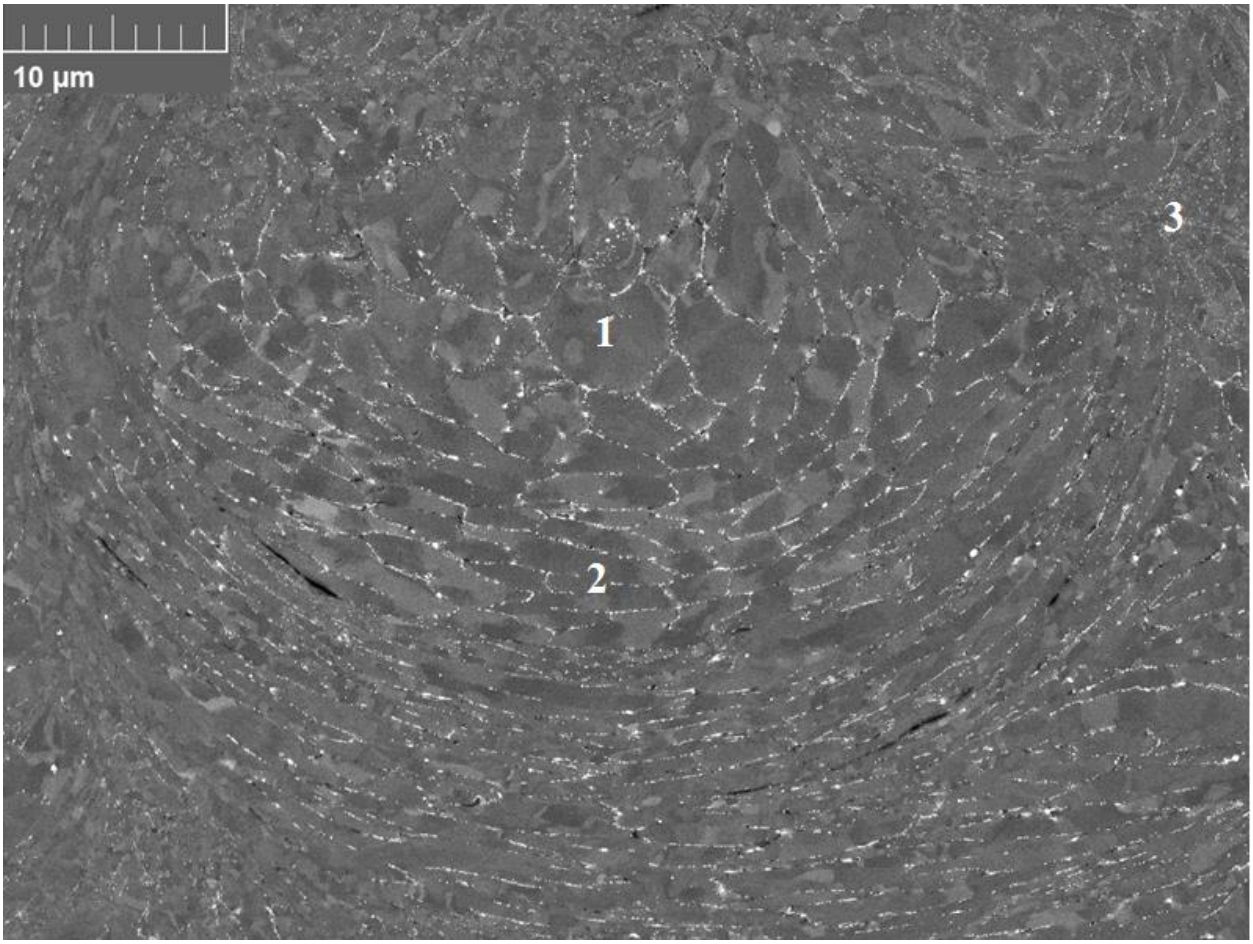

Figure 15 SEM micrograph of 10hr annealed samples. 1) low deformation 2) medium deformation 3) high deformation [33].

Recrystallization is the second portion of the annealing process and represents the bulk of the mechanism by which internal strain energy within the grains are reduced. Reorientation of the crystal structure is governed by nucleation and growth rate dynamics which is out of the scope of this project [6], [7], [69]. Recrystallization is coalescence of new defect free crystals within the grain exhibiting low quantities of defects and have properties more representative of the bulk then of cold worked microstructure. This has been observed in 6061 aluminum at 200°C though the reduction of average grain length and has been attributed to localized imbalances in surface tension of high and low angle grain boundaries [68]. Micrographs presented show the

evolution of the microstructure after heat treating at 200°C, approximately 45% of the melting temperature of 6061 aluminum. The SEM micrographs from bulk cross sections show that the UFG microstructure which exhibits exaggerated grain growth with respect to the degree of deformation.

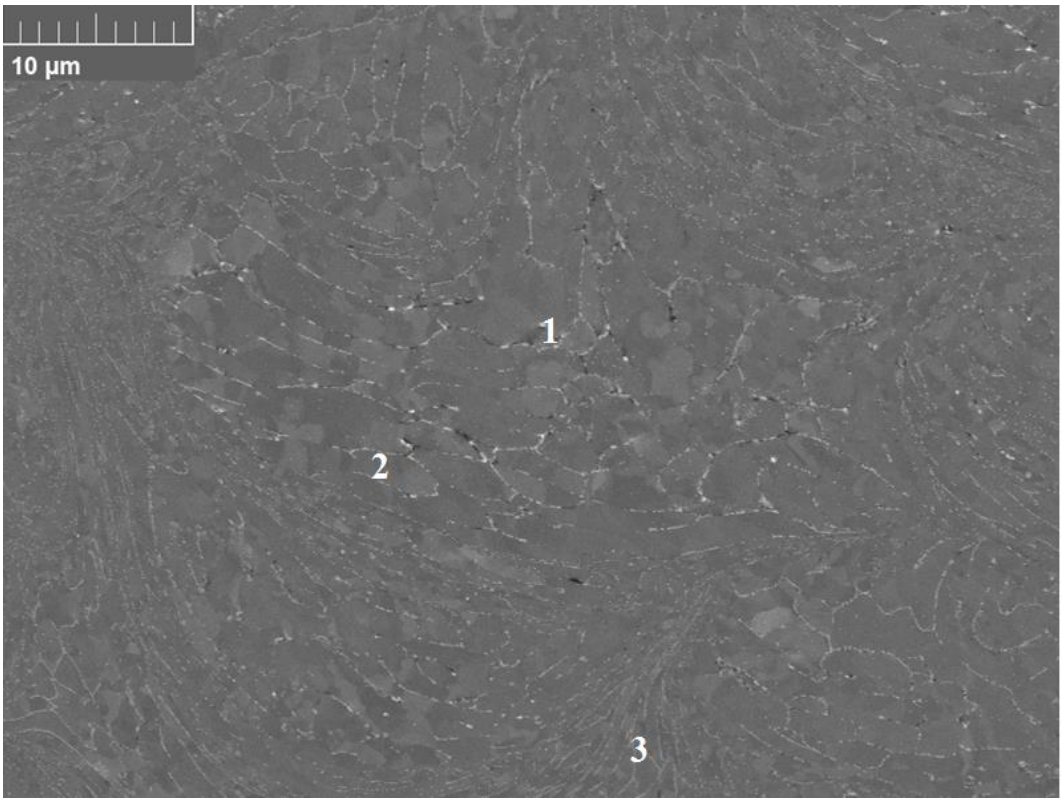

Figure 16 SEM micrograph of 100 hour annealed samples. 1) low deformation 2) medium deformation 3) high deformation [33].

Micrographs in Figure 16 of 6061 Al samples show the formation of voids at triple points as well as the inclusion of cracks of varying morphology within the microstructure. Larger cracks can inhibit particle on particle contact reducing the possibility of diffusion with neighboring particles resulting in large voids which can be seen in the fracture surface [70], [71], [72]. The

micrographs above illustrate the degree of the recrystallization within the more heavily deformed microstructure which relived some of the stresses imparted during the CS process after the heat treatment process. Similar observation into annealing CS aluminum alloys have shown that at low temperatures grain boundary migration is inhibited by significant grain boundary solute segregation and precipitates [67]. Evidence of the effects of the heat treatment process should manifest as an increase in DF within the bulk.

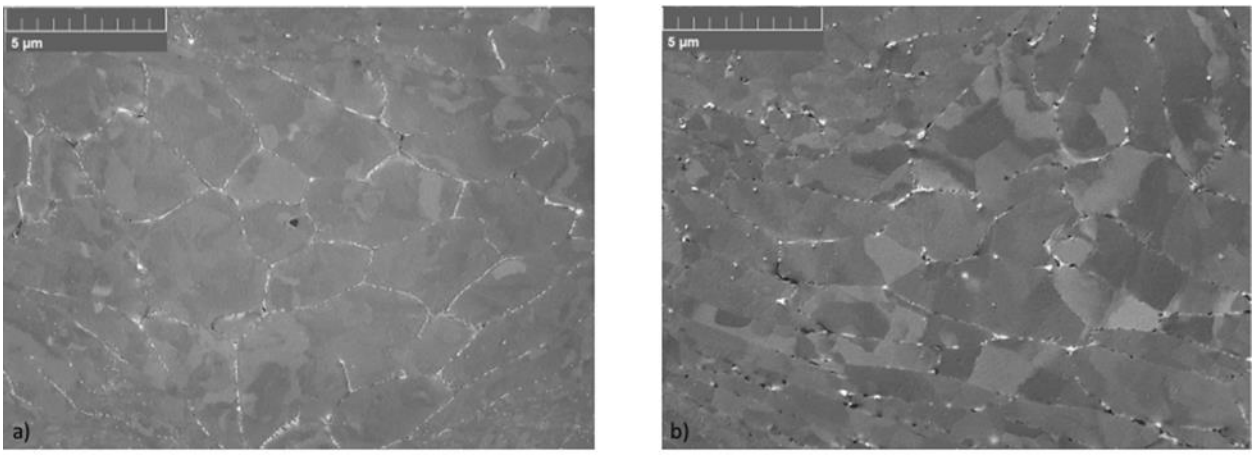

Figure 17 The microstructural evolution a) AR low deformation b)100HR annealed at 200°C low deformation [33].

2.4 Fracture Morphology of Aluminum in Wrought vs Cold Sprayed Form

Micrographs of a fracture surface can provide information about the relationship between the microstructure and failure of the bulk. Traditionally, macroscopic observation of the fracture surface is conducted by optical microscopy where indication of reduction in cross sectional area before final fracture (necking) or a dull appearance infers ductile failure. Ductile failure mechanisms are indicative of failure by shear, resulting in plastic deformation and a fibrous appearance macroscopically. Conversely, a shiny appearance in conjunction with sharp

faceted edges is characteristic of brittle failure. Although fractography is well-documented in wrought materials, little is known about the relationship between fracture and underlying CS microstructure.

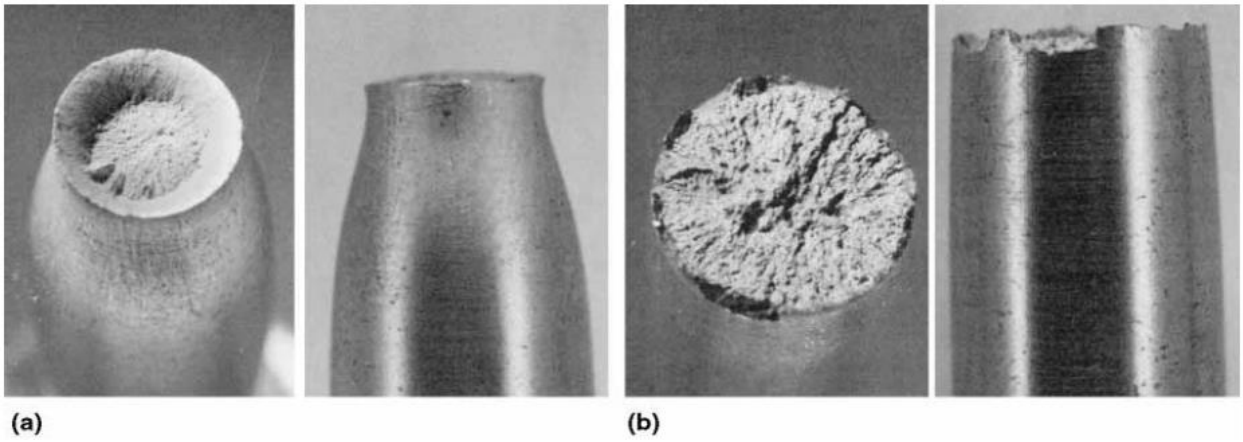

Figure 18 Fracture modes a) ductile failure displaying classic cup and cone morphology, b) brittle fracture surface [17].

Images presented in Figure 19 show the macroscale and microscale of a typical 6061 aluminum fracture surface. The macroscopic image in Figure 19a show the reduction if cross sectional area or necking seen above in Figure 18. Higher resolution images in Figure 19 show ductile failure features at various magnifications and illustrate the nature of ductile failure in wrought 6061 aluminum.

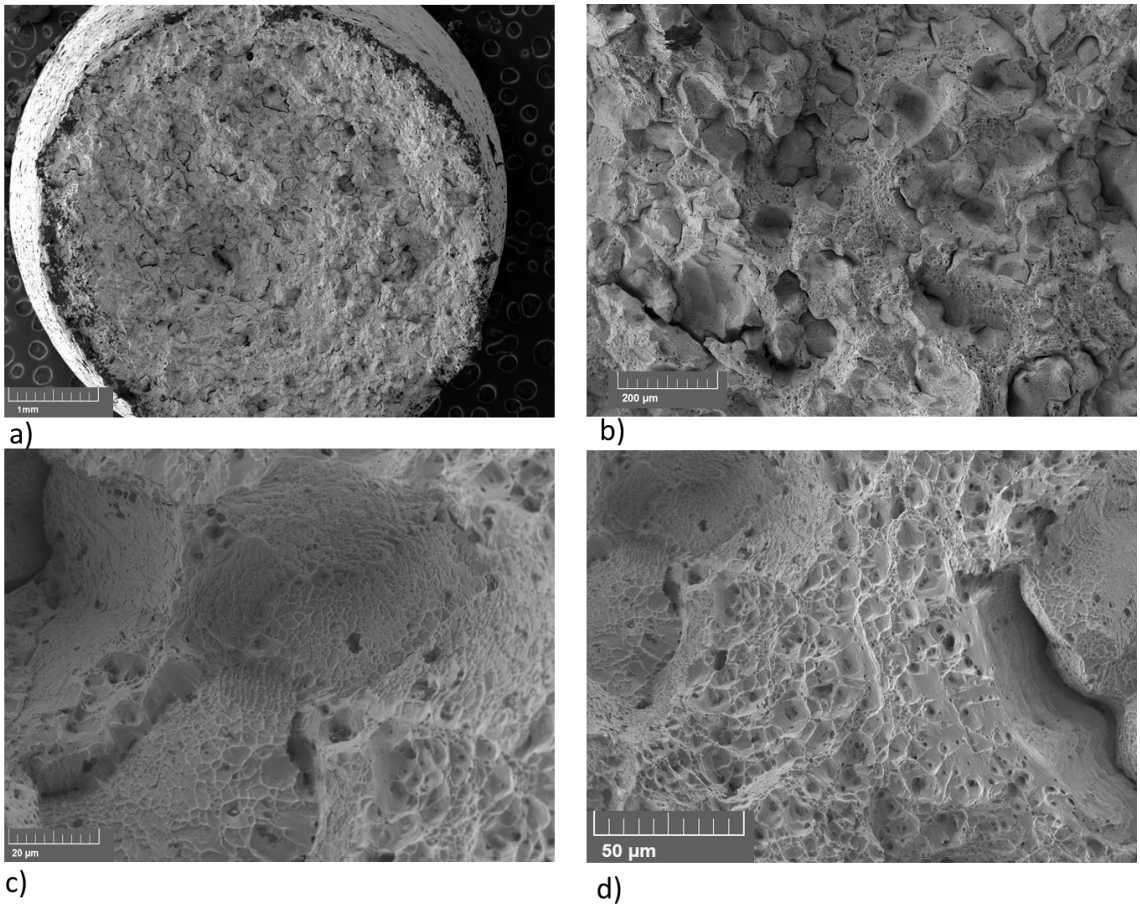

Figure 19 the fracture surface of wrought 6061 Al at increasing magnification.

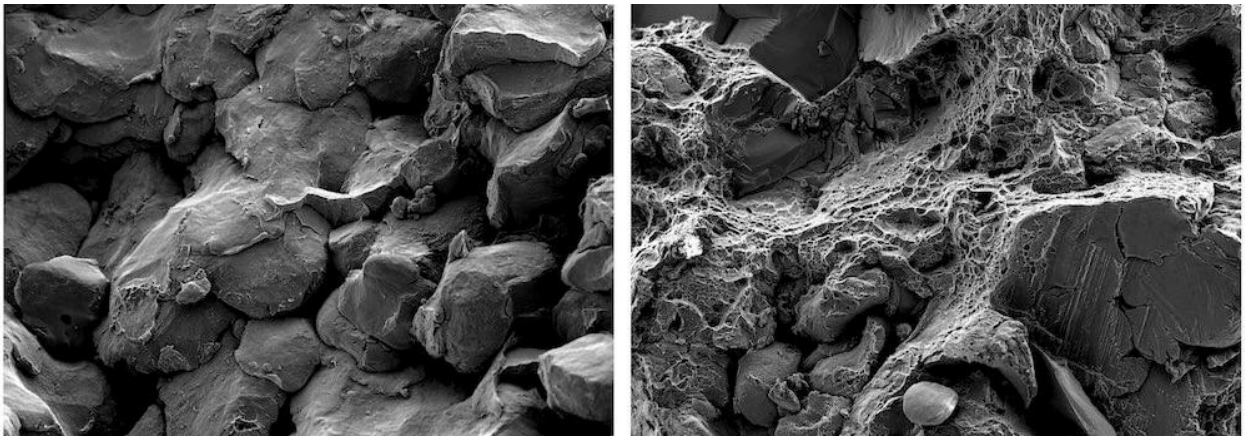

Figure 20 Micrographs of CS fracture surfaces taken at Trinity College in Dublin a) show interparticle fracture (IF) b) ductile fracture (DF) and cleavage plane fracture (CPF) [73].

Initial investigation into the microscopic features associated CS 6061 Al in Figure 20 show the disordered nature of a CS fracture surface which displays interparticle fracture (IF), ductile fracture (DF), and cleavage plane fracture (CPF) [73]. Intergranular failure is the least common failure mode seen in properly processed material. Brittle failure is observed from the presences sharp topographical features often displaying characters river marks or chevrons indicating the initial source of failure and is a result of fracture across preferred crystallographic planes, {110} in Al [74]. Brittle failure is not typical of ductile materials but can occur with enough normal stress is applied to the appropriate cleavage planes [74]-[77].

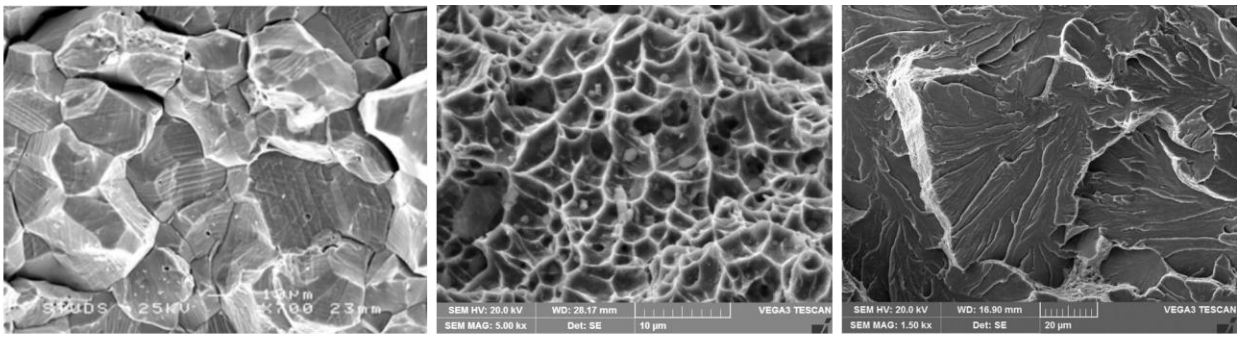

a) b) c)

Figure 21 Micrographs of fracture surfaces displaying a) intergranular failure, b) ductile failure, c) cleavage failure [22], [23].

Slip is the mechanisms by which single crystals deform and ductile failure (DF) can be observed. These mechanisms are shear processes that typically require closed packed planes, {111} in Al, critical shear stress values and specific directions (45°) [6], [7], [75]. Wrought 6061 aluminum typically displays DF as observed on the presence of micro void coalescence resulting in dimpled surface morphology. During this phenomenon small micro voids nucleate around inclusions within the bulk. In the continued presence of increasing tensile loading the voids

begin to coalesce resulting in the propagation of a crack tip through the material ending in complete material failure [8], [74], [76]. Fracture surface micrographs in Figure 21 b) show the surface morphology left because of DF. The influence of process parameters as well as post processing heat treatments should manifest themselves as observable microscopic details and changes within the fracture surface of 6061 CS bulk material.

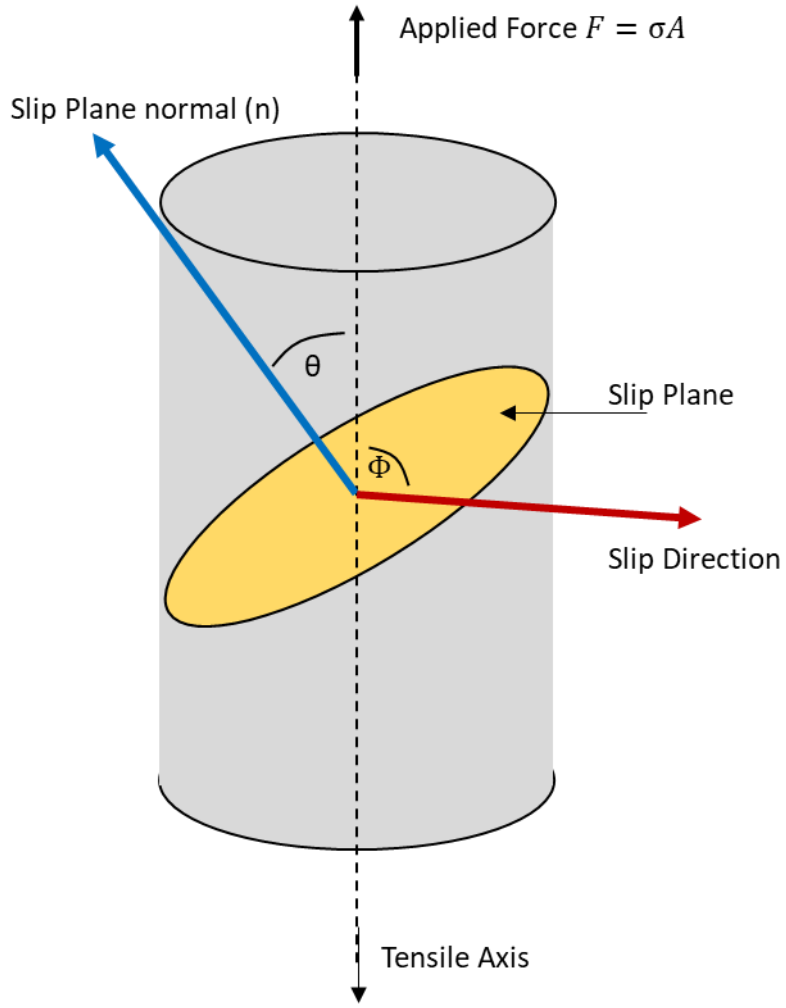

Figure 22 The slip plane and slip directions in accordance with Schmid's law .

Chapter 3: Methodology

3.1 Metallographic Specimen Preparation

The bulk consolidated material was provided by the ARMY research lab (ARL). Individual samples were created and MSERF by cutting them from the bulk using a low speed oil cooled saw. The low speed saw reduced the degree microstructural evolution resulting to heat generated through other cutting methods. Bulk samples were then heat treated in air for 10 and 100 hours respectively in a Thermo Fisher Scientific PID controlled tube furnace at 200°C. After heat treatment the samples were pulled in tension, fracture mode 1, to produce the two halves of the sample. One half was preserved for imaging using the MIRA 3 field emission gun and while the other half was prepared for metallographic preparation.

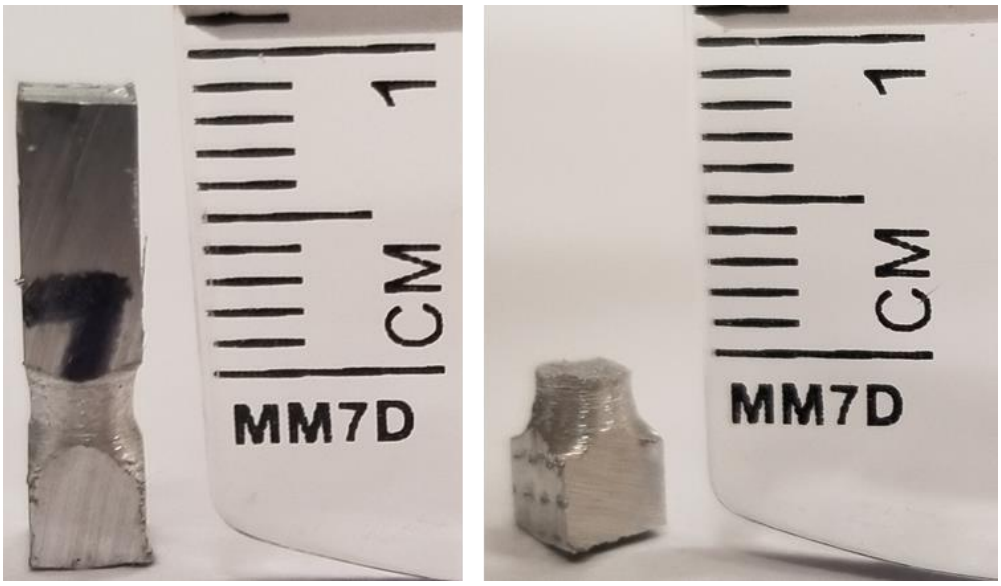

Figure 23 Samples removed from the consolidated bulk materials with notches. a) show the sample before fracture b) shows one half of the sample after fracture in mode 1.

Mechanical sample preparation was conducted on an Allied High Tech MetPrep3 with accompanying consumables. Samples were polished to 1200 grit polishing papers and subsequently polishing with cloths down to 0.04µm media. Rotational speed of the auto-polisher was set to 100 rpm for both the sample and sample holder with 2 LBF applied to the back of each sample.

Mechanical strain imparted though mechanical preparation was removed via Buhler Vibromet using .04µm silica media. The final step in the mechanical preparation of the samples selected to ESBD and SEM imaging is ION milling. This study used a Leica TIX 3 Ion mill out fitted with three guns operating at 4kV and 1.5A. The samples are set to rotate 360° and a 1.5° tilt.

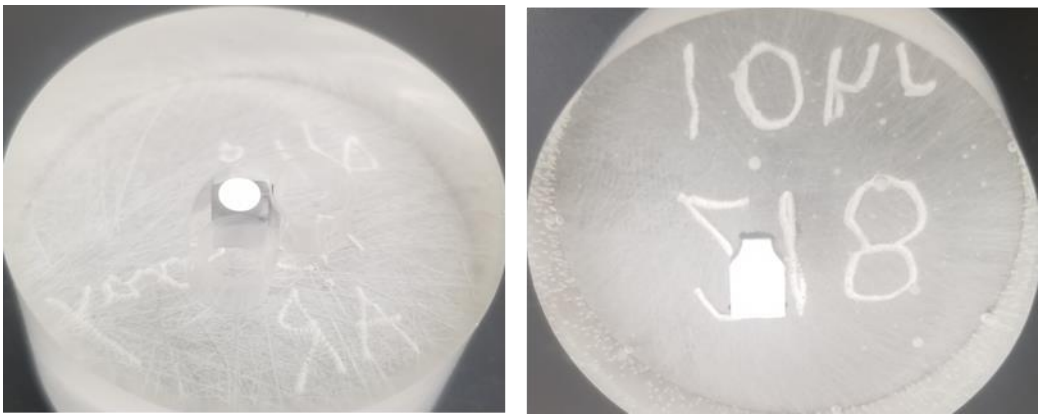

Figure 24 Both halves of the sample are shown after metallographic preparation. A) shows the side prepared for microstructural evaluation while b) has been prepared for EBSD and fracture path investigation.

3.2 Physical Measurements: Microhardness

Microhardness data was collected for each sample with a Tescan HMV-G microhardness tester equipped with a Vickers pyramidal microhardness indenter. Indentions are run in batches of 25 over an area of 200 by 200 microns. The indenter penetrates the flat sample surface with 0.05N or 490.3mN for a hold time of 10 seconds. Characteristic microhardness data collected from the samples is compared to data collected from wrought 6061 aluminum which is displayed below. Microhardness is a characteristic of a materials surface and not a bulk material property. It captures a materials resistance to penetration, but only obtains information form the localized are that interacts with the indenter. This results below are compared with the ASTMB308 values which is 107 HV.

Maximum value	112
Minimum value	105
Average	109.2
Standard deviation	2.24%
Coefficient of Variation	2.05%

3.3 Scanning Electron Microscopy and Electron Back Scattered Diffraction

All imaging was conducted using a Tescan MIRA 3 field emission gun outfitted with an annular back scatter detector, EBSD detector and Oxford EDS system. In preparation for inspection, process powder was mixed with a small amount of low curing temperature two-part epoxy and allowed to cure while dry process powder was mounted onto a 12mm SEM pin stub with carbon stick tabs. SE imaging of the fracture surfaces as well as microstructure of samples was conducted at low accelerating voltage of approximate 2kV with a beam intensity of approximate 10. BSE and EBSD images were taken at higher accelerating voltage and beam intensity at 12Kv and 12 respectively.

EBSD is a technique used to determine grain orientation within a crystalline sample. The sample is positioned in conjunction with a detector at a pre-determined angle 70° from the normal and working distance of 15mm. The electron beam interacts with the sample and the phosphorus screen on the detector searches for pre-indexed kikuchi band patterns. These patterns infer the orientation of the area indexed under the beam as the electron beam rasters across the sample surface. Resolution, ability to more confidently identify the microstructure, of small microstructural features requires a small spot size, physical diameter of the electron beam, as well as a small step size, distance until the next indexing area. If the spot size is larger then

the microstructural feature overlapping kikuchi bands can cause interreference resulting in no orientation detection or a wild spike. If the step size is too large either the bounds of the microstructural feature will not be indexed resulting in unclear bounds for microstructural features, or features may be passed over and not indexed at all. Another difficulty is depth of penetration, in order to achieve ample signal to noise ratio from the beam sample interaction the voltage must be increased to 12kV which increases the depth of penetration and possibility to obscure kikuchi patterns produced by small surface features.

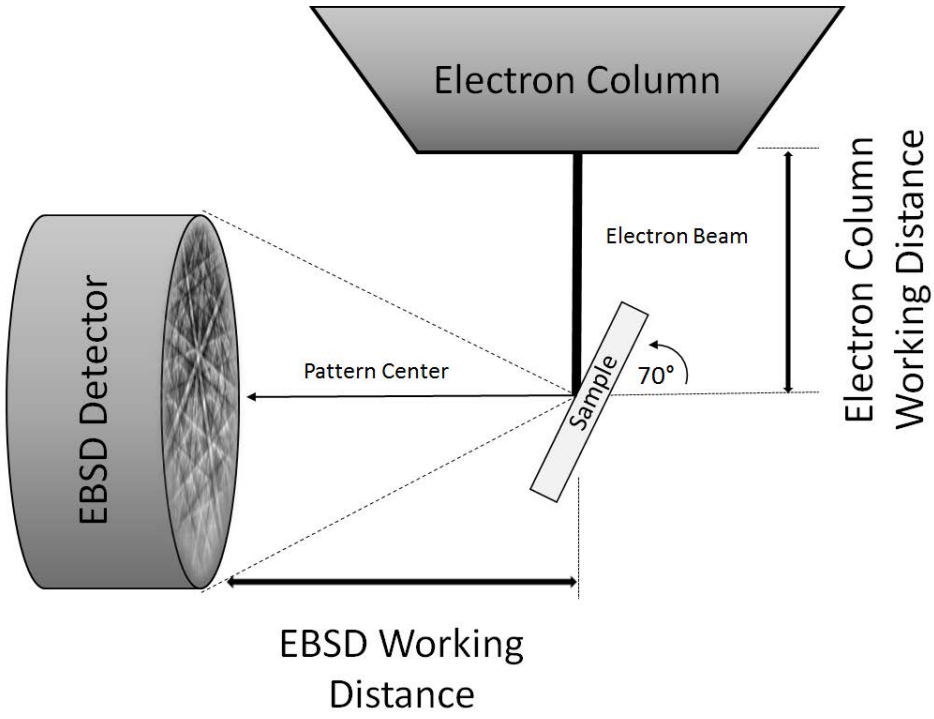

Figure 25 Illustrates the configuration of the sample beam interaction within the SEM chamber. This configuration is essential to proper indexing of the kikuchi patterns.

Chapter 4: Results and Discussions

4.1 SEM Analysis of the Microstructure

Images taken from as-spray direction used in conjunction with SEM images previously taken by the research group are presented below in Figure 26 and begin to illustrate the non-homogeneous microstructure in 3-D. The round circular nature of the orthogonal particle impact can be seen in the Z direction, with the characteristic round droplet shape observed in the X and Y directions.

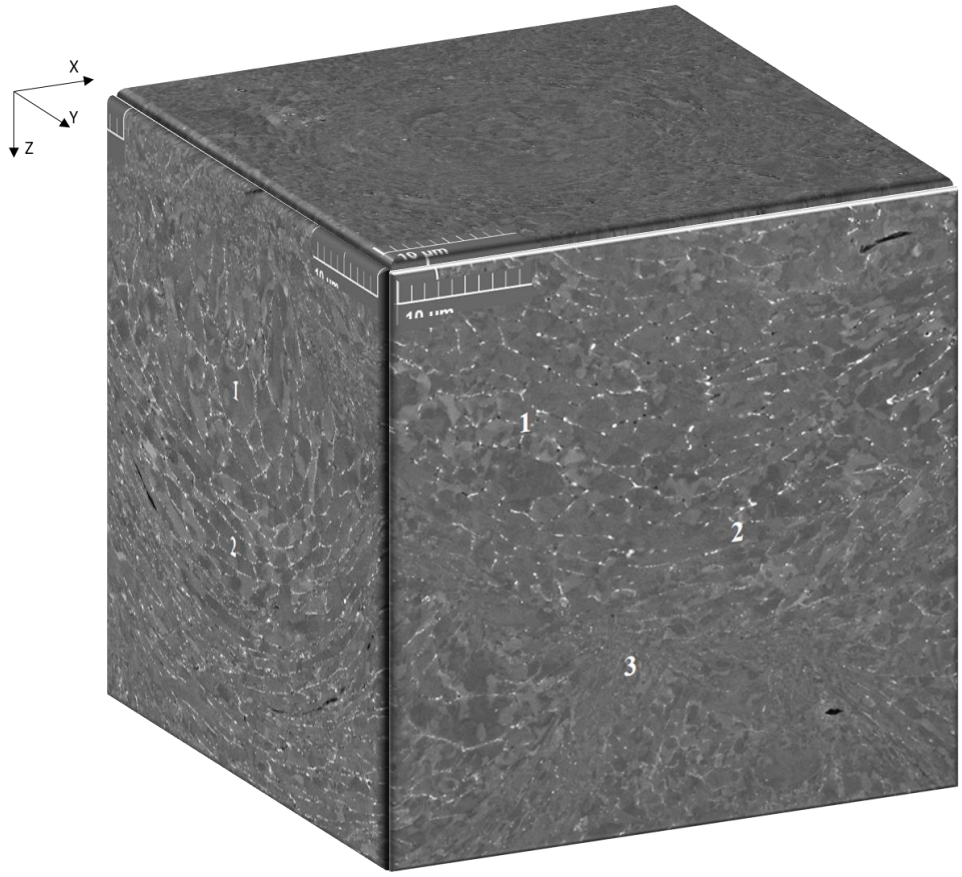

Figure 26 Is a 3-D view of the microstructure based on orthographic projection which utilizes 2-D images obtained through SEM of the characteristic microstructural features in the X,Y,Z directions respectively.

Micro-hardness utilizing the size of indenter in conjunction with the force required to produced accurate and repeatable indentions was too large for the microstructural regimes within the specimen. SEM images of the flat microstructure were taken prior to microhardness indention. After indention the area of interest was re-imaged which provided pre and post indention micrographs of the microstructure. The area fraction of microstructural regime captured was then determined using image J post processing analysis.

The 10 HT samples produced the most clear and representative indentions, but after examination of the data no statistically significant hardness data was collected to show a

correlation between the area fraction of microhardness regime to increased hardness values. A higher resolution technique such as nano-indention or atomic force microscopy techniques could be used gain more insight. Micro hardness data for the 10-hour heat tread samples is presented be low in **Error! Reference source not found.** which shows an average micron hardness of 103.1HV which is lower than wrought samples, but still within 1 standard deviation of the average.

Table 2 Statistical analysis of the hardness data collected form 10 hr HT samples.

Maximum value	116
Minimum Value	94.4
Average	103.10
Standard deviation	5.77%
Coefficient of variation	5.60%

4.2.1 As Received Samples (Non-Heat Treated)

Stitched micrographs in Figure 27 show the microstructure in the as-sprayed direction of the CS 6061 Al in which the non-homogenous microstructure can be observed. At low magnification the metallographically prepared samples show what appear to be large areas LDR with mixed deformation modes in-between. The LDR represents approximately half of the surface area within the micrograph and are homogeneously distributed throughout the microstructure. The 2-D landscape shows LDR with a range of diameters from 15-35 µm, which is consistent with process powder dimensions. Higher magnification micrographs provide more insight into the microstructure of the mixed mode area.

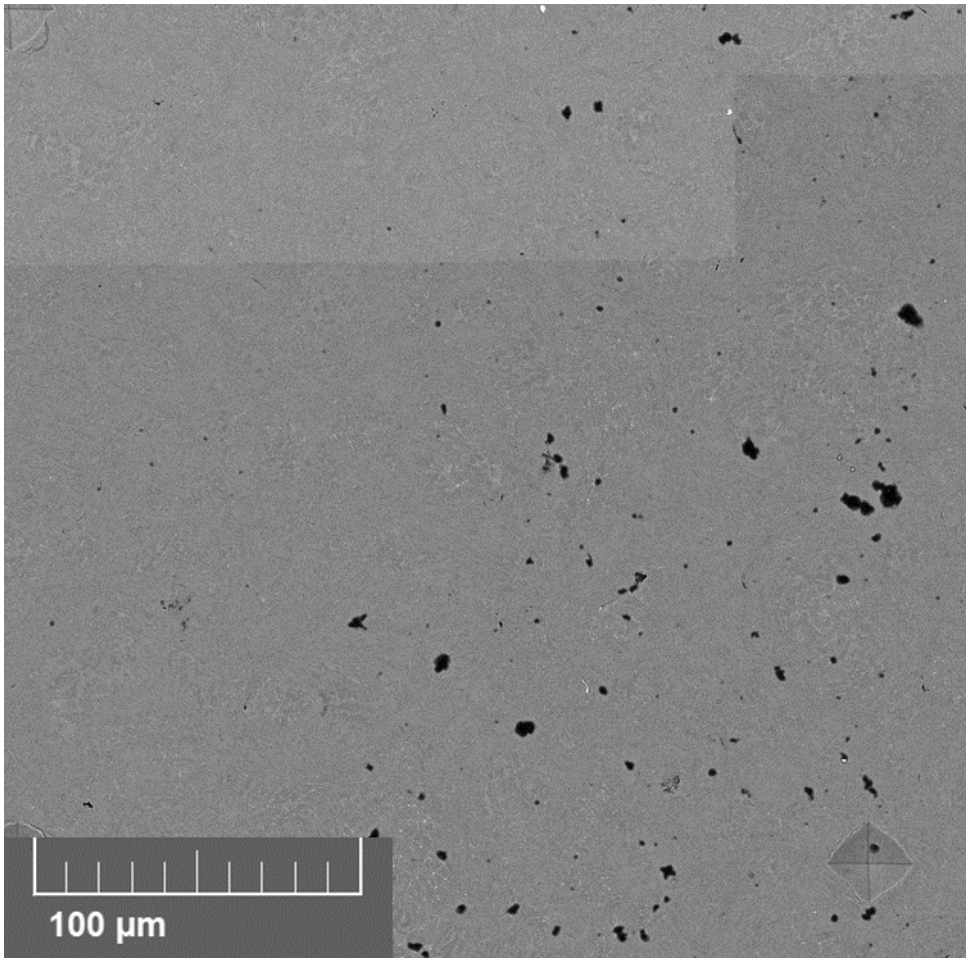

Figure 27 A stitch of several micrographs that depict the AR microstructure. The area captured within the image is approximately 200x200 microns and captures multiple deformation regimes.

Higher resolution micrographs presented below show all the major deformation regimes captured in one image and gives more insight into the mixed mode regions as well as providing more detail about the LDR. The microstructural area labeled LDR in Figure 28 shows an area which exhibited little change though deposition. This area defined as the LDR are present in most of the upper portion of the micrograph extending well over 50µm along the abscissa. Within the LDR the individual grains are defined by presence of alloying constituent element which appear lighter and can be seen in SE mode due to their higher atomic densities. In the AR

micrographs the distribution of these alloying constituents is not homogenous throughout the bulk. Furthermore, large differences in contrast within the grains indicate the existence of retained internal stress within the individual grain resulting in the formation low angle grain boundaries (LAGB) which this is line with experiments conducted by Rockni et al on-process powder. These could also be explained by residual stresses retained as a result of mechanical preparation.

The HDR is also presented in the micrograph and represents a large surface area fraction of the image where the Intermedium Deformation Regime (IDR) is dominated by the presence of UFG. Very little of the alloy constituent elements can be seen within the IDR therefor the bulk of the grains are defined by their degree of misorientation. The IDR can be seen exhibiting an elongated area with dimensions of approximately 7μm in width and lengths more than 10μm. The characteristic flowing nature of the IDR suggest that these areas area formed from metallic flow phenomenon at extremely high strain rates.

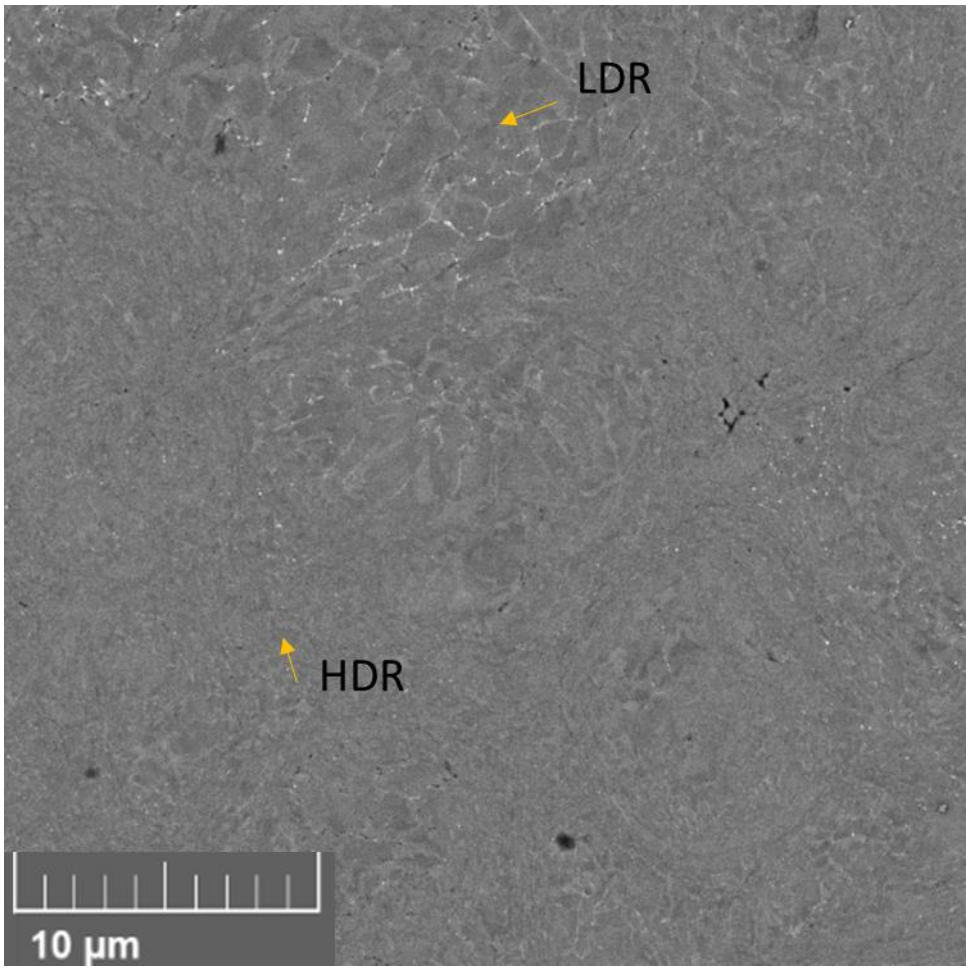

Figure 28 A higher magnification SE image which shows a microstructural landscape dominated by both LDR and HDR areas. This image shows little in the way of MDR which are seem in conjunction with IDR.

While in Figure 28 the LDR and HDR are the predominantly featured microstructures, Figure 29 shows an area within the microstructure that is more evenly distributed. Captured within the micrograph is a fiduciary indent of approximately 10X10 µm which sits adjacent to a circular LDR approximately 13µm in diameter. The MDR can be more easily seen within the IDR and shows similarities to the HDR, but with larger grains. The MDR as well as the HDR exhibit what can be described as elongated microstructural regimes in where their area fraction is less localized and “flows” in-between more localized LDR.

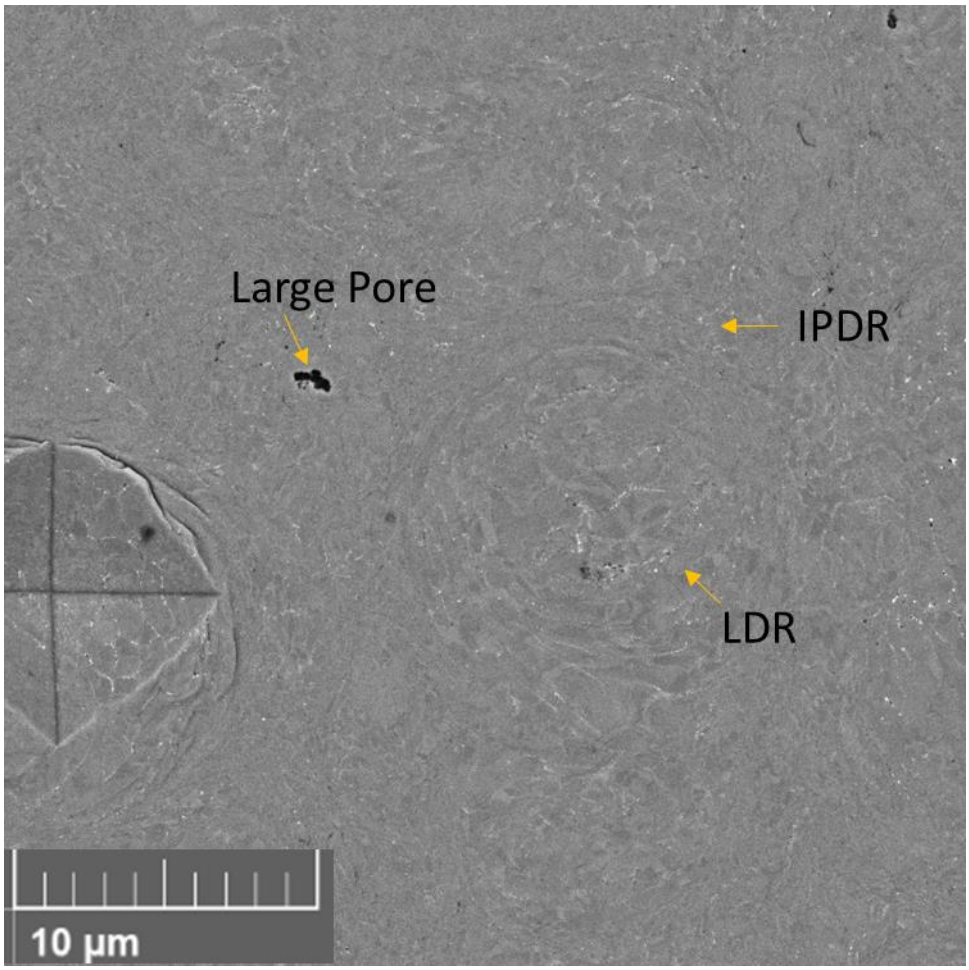

Figure 29 Reveals a more evenly distributed microstructure. LDR and IDR and highlighted as well as a large defect in the form of a pore.

4.2.2 10 Hour Heat Treated Samples

The high-resolution low magnification stitched SE images of the 10-hour heat treated microstructure show a larger size and distribution of the circular LDR. The bulk sample after low temperature heat treatment and illustrates the porous nature of the microstructure. The stitched micrographs also show large areas of up to approximately 30 microns in diameter which correspond with low deformation as notated by large grained areas with well-defined

boundaries and large observable changes in contrast inferring the continued presence of LAGB. Areas between round microstructural features which are home to the MDR and HDR begin to form more coherent matrix more representative of a quasi-bimodal microstructure.

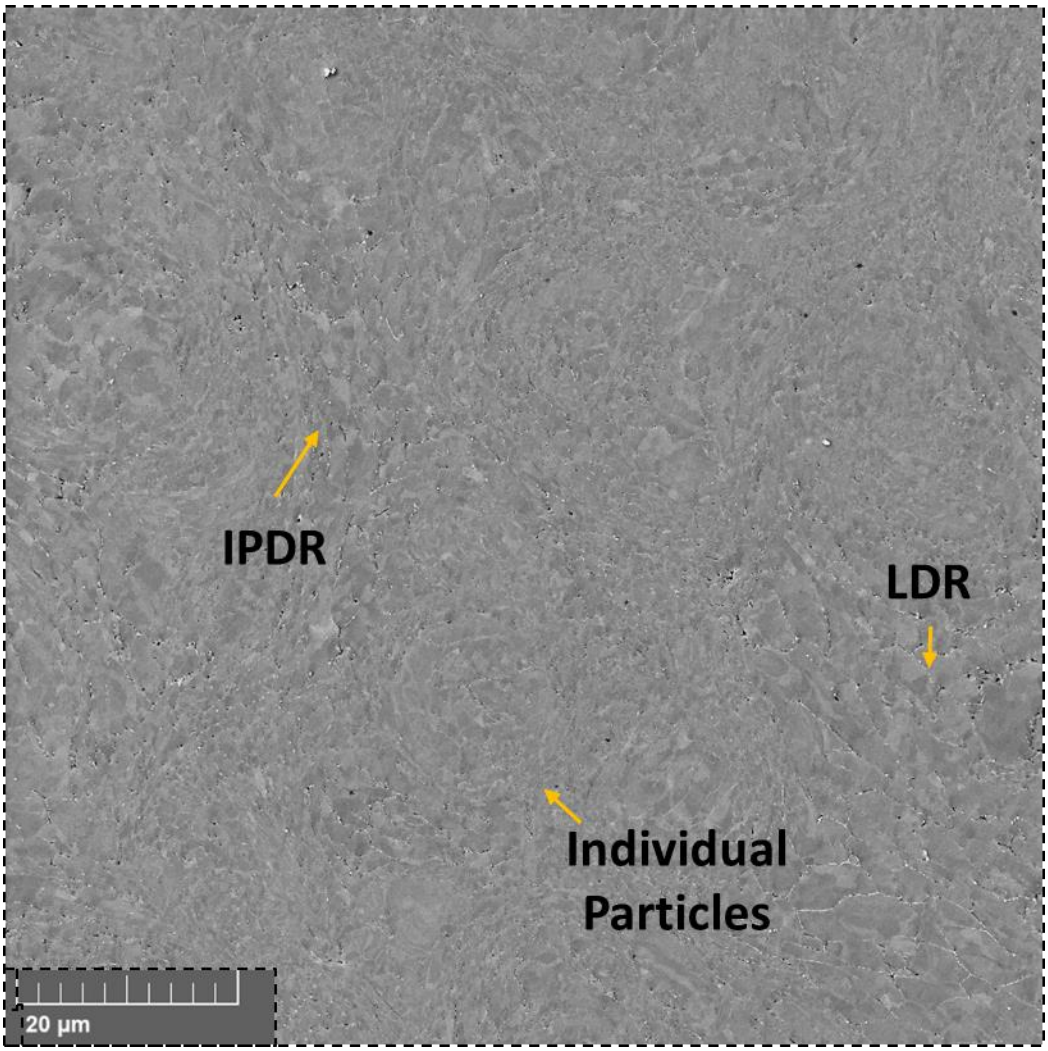

Figure 30 Cross sections of 10-hour samples heat treated at 200C. Highlighted are the inter-particle zone which is comprised of medium and high deformation regime. Low deformation regimes are characterized by the large grained which are similar in size to grains seen in process powders.

The higher magnification images in Figure 31 shows the size and distribution of the fine-grained regimes within the bulk. Coarse grained circular features, possibly orthogonal impact

zones, range in size from 15-30 microns in diameter and are visible with Inter-particle deformation region (IDR) of varying in size regime from MDR to HDR.

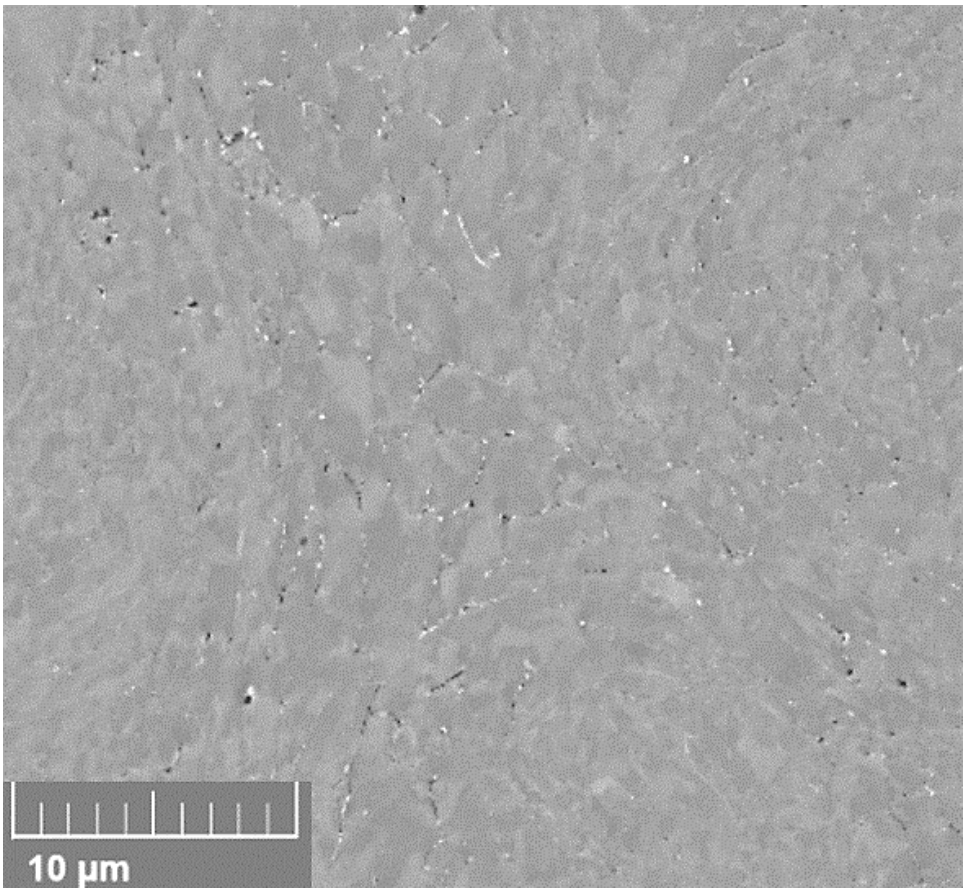

Figure 31 Cross sections of 10-hour samples heat treated at 200C. Highlighted are the inter-particle zone which is comprised of medium and high deformation regime. Low deformation regimes are characterized by the large grained which are similar in size to grains seen in process powders.

The inter-particle deformation regions range in grain size and morphology with some grains displaying elongation while others are more uniform after HT. It is important to consider that cross sections of elongated microstructures can present themselves as a more uniform or round by varying the viewing axis. The junction of a three LDR is shown above in Figure 31 which depicts the microstructure between particles after the 10-hr heat treatment. The MDR which

makes up the bulk of the inter-particle zone can be observed with surrounding HDR. Microstructural defects and sub-micron pores are visible with precipitates tending to consolidate along MDR grain boundaries. Large holes and alloying constituents are observed more frequently in MDR with HDR as compared with the AR samples. Some of the pores in the image can be attributed to porosity while others to the removal of mechanically superior intermetallic compounds during mechanical preparation.

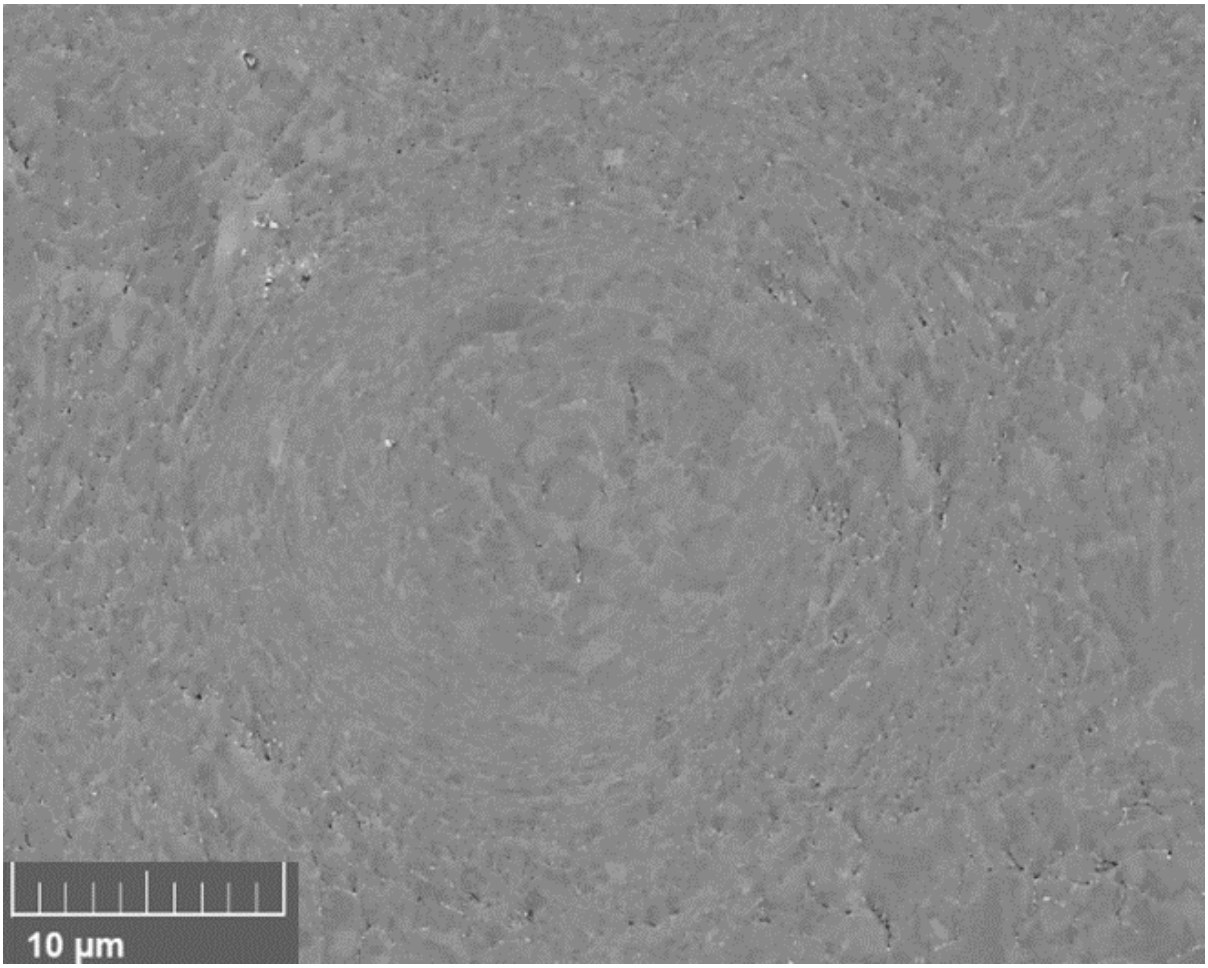

Figure 32 The cross section of a particle splat. The size and morphology of the microstructural feature is consistent with that of the process powder. Multiple layers of microstructural regime can be seen in the micrograph.

Figure 32 shows the cross section of a particle impact zone which displays the characteristic microstructural features imparted through SPD associated with the CS process. The size and morphology of the circular microstructural features suggest that this is associated with orthogonal particle impact. The absence of large elongated or consistent defects at the peripheral edges near HDR to MDR transition also support a particle impact as opposed to an imbedded particle that did not achieve sufficient velocity for deposition. HDR surrounding the particle impact zone show little in the way of GB precipitates and large intergranular defects. Pores and defects can be observed on the peripheral edges of the impact where transition of grain regime is more distinct.

Figure 33 highlights an area characterized as LDR which displays many grains defined by the presence of defects along GB. The size of the grains varies as well with the smallest having an approximate diameter of 5µm and the largest of over 15µm which are much larger than LDR observed in the AR samples. Some of the grains within the microstructure can be seen with LAGB observed by the gradients present within the grain structure.

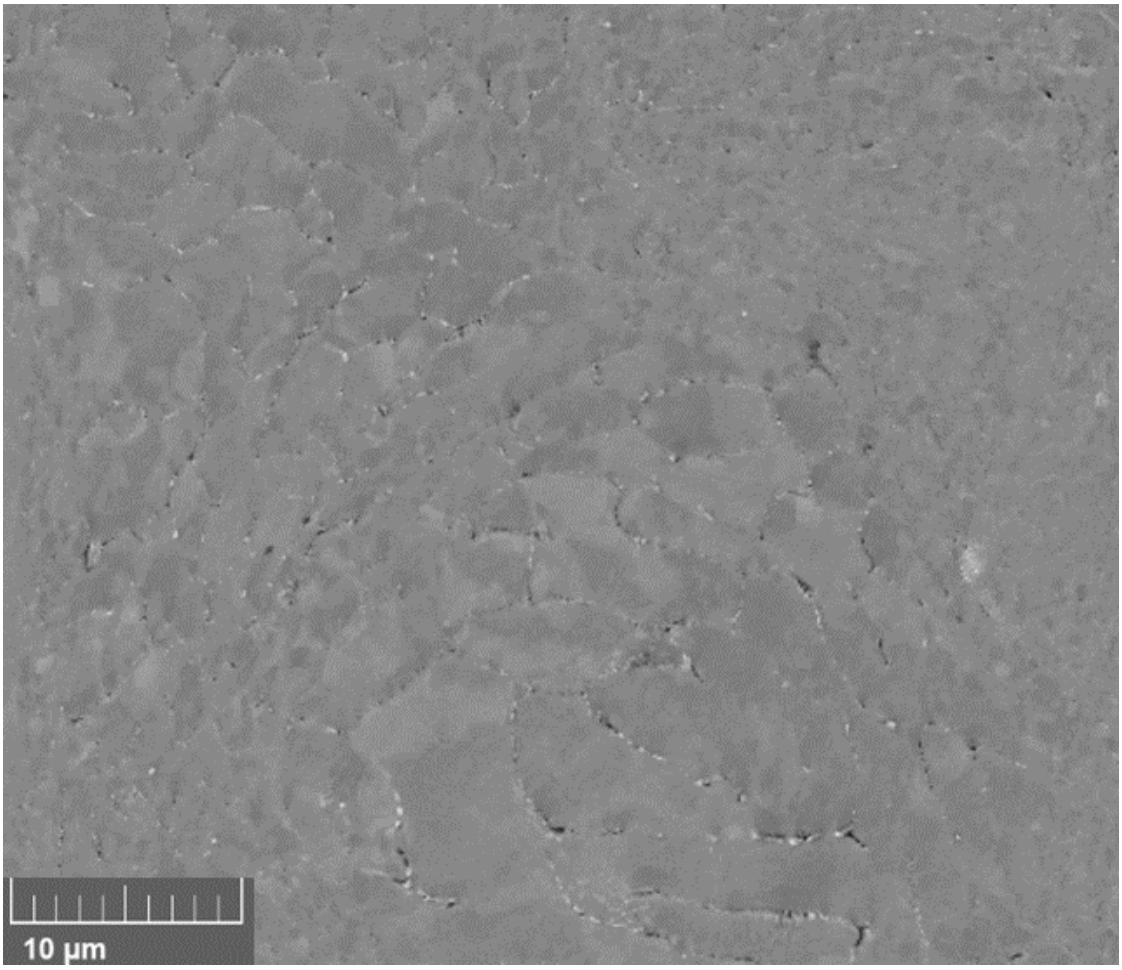

Figure 33 High magnification micrographs of the 10-hour heat treated samples show transition areas between low and high deformation regimes. The low deformation regimes which consist of the large grain areas show increased distribution of intergranular defects.

4.2.3 100 Hour Heat Treated Samples

The microstructure of the 100-hour heat treated sample can be seen in Figure 34 which shows a more uniform size and distribution of morphological features as compared to the 10-hr

and AR samples. The cross section shows round microstructural features of approximately 30µm in diameter which is consistent with the 10-hr heat treated samples. Unlike the 10-hr samples, the distribution of the features is more homogeneous through the micrograph. Areas characterized previously as interparticle areas show little or no significant sized defects but show a reduction in surface area seen in the image.

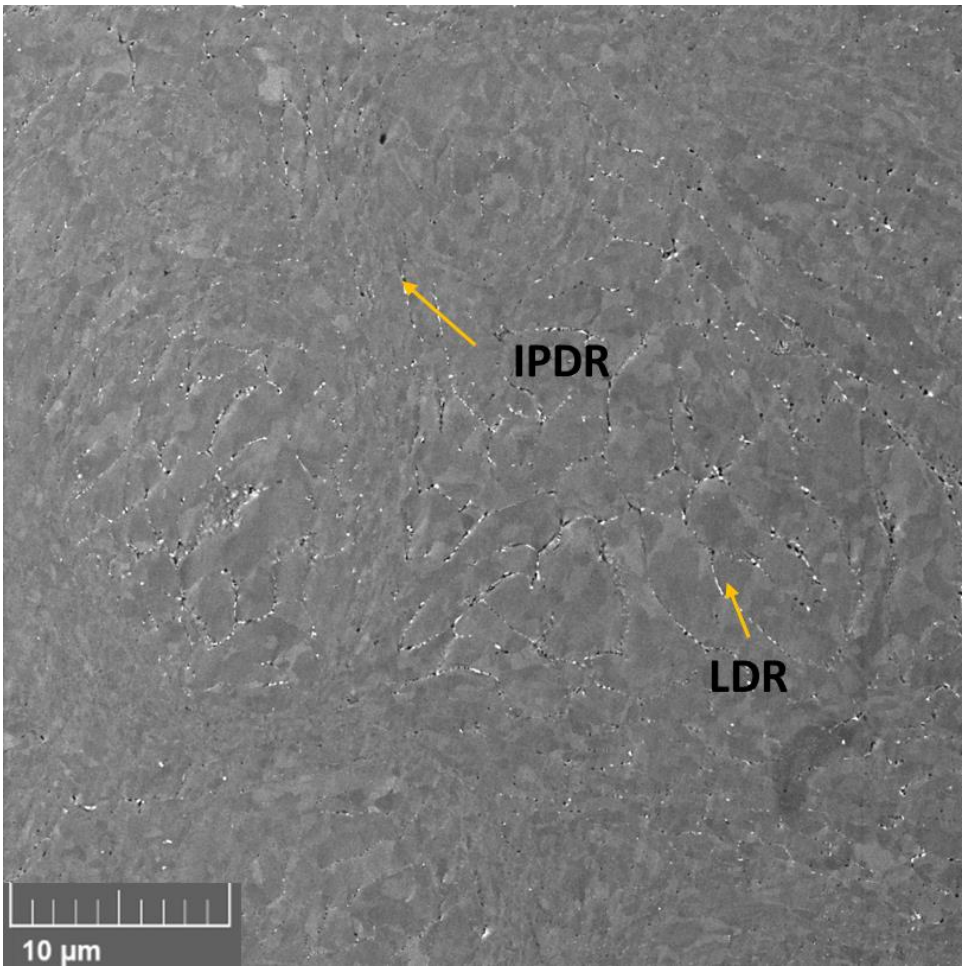

Figure 34 Is a higher magnification which highlights a more complex region of the microstructure. All the deformation regimes can be seen in the figure which also show areas of stark regime transition.

The round features that scatter the surface of the cross section display a wide range of grain size. The interparticle areas are most characteristic of the HDR which is consistent with the

10-hr samples. Round features with diameters larger than 20 μm tend to consist of LDR while MDR tends to dominate features with perceivable cross sections. The interparticle areas which consist of finer grains can be seen surrounding the round features creating quasi composite consisting of an HDR matrix reinforced with LDR and MDR. The HDR areas seen in Figure 35 form channels betwixt the courser grained areas ranging in width from 4-8μm, but extending for larger length throughout the microstructure. Micrographs in Figure 35 show a round microstructural feature which displays similar morphology to the 10-hr sample. The defects and particulates can be seen in all deformation regimes within the cross section but are more heavily distributed throughout the LDR and MDR.

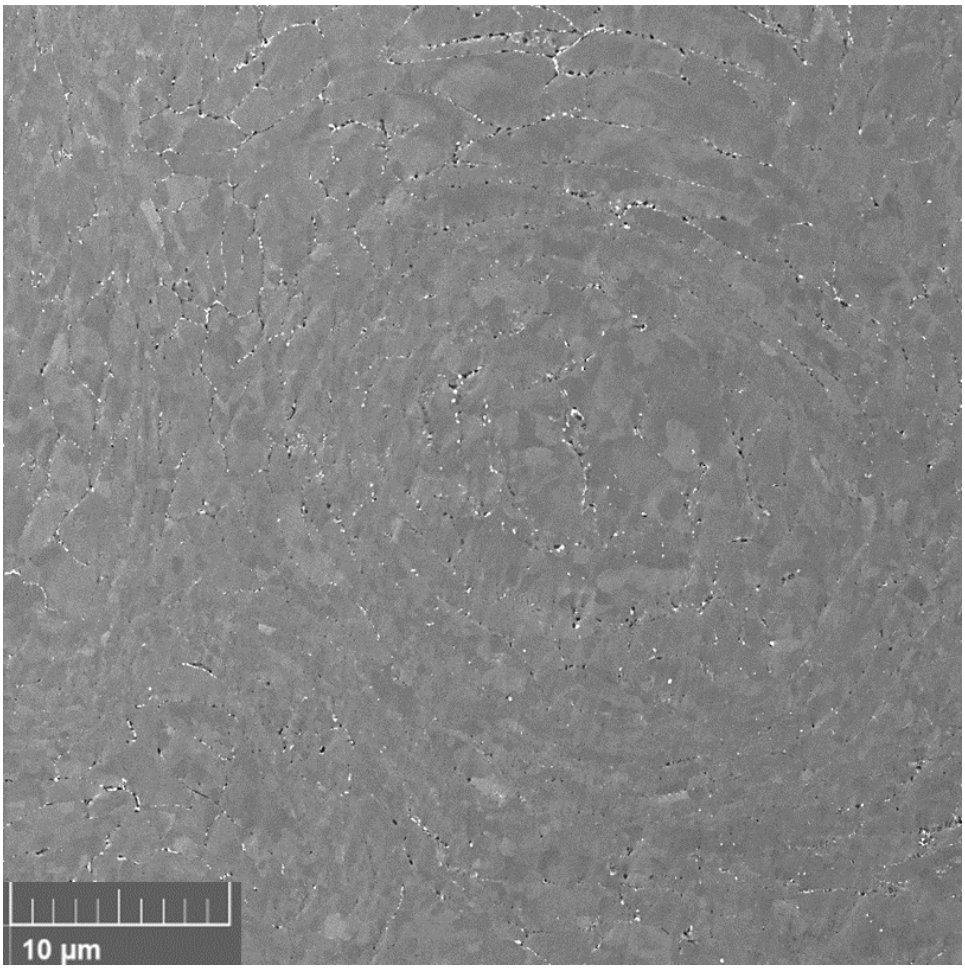

Figure 35 High resolution micrographs show the characteristic round microstructural surface of the 100-hr heat treated samples. Higher magnification images show the range of grain size regimes associated with the microstructural features. Defects and precipitates can be observed coalescing along GBs within the bulk.

4.3 Fractography

4.3.1 Fracture Surface of As-Received Samples

The macroscopic appearance of the AR CS fracture surface was found to display primarily ductile failure modes with HT samples displaying non-characteristic surface appearance.

Micrographs of the fracture surface in Figure 36 show a morphology dominated by butte-like structures of varying sizes with faceted edges showing signs of dimple rupture and stepping. The top of the micrograph shows the large surface of a mostly non-deformed powder particle deeply embedded within the bulk. Also seen in Figure 36 is the presence of ductile failure by way of micro void coalescence through the observation of dimple rupture in the fracture surface. The average size of the dimples is submicron in nature but can be seen sparsely throughout the fracture surface. The large wall seen in the bottom left corner of the micrograph displays localized areas of ductile failure transitioning up the fracture surface with dimple elongation parallel to the force applied for failure. A mostly deformed particle can also be seen exhibiting dimple rupture and material deformation near the adiabatic shear jet site.

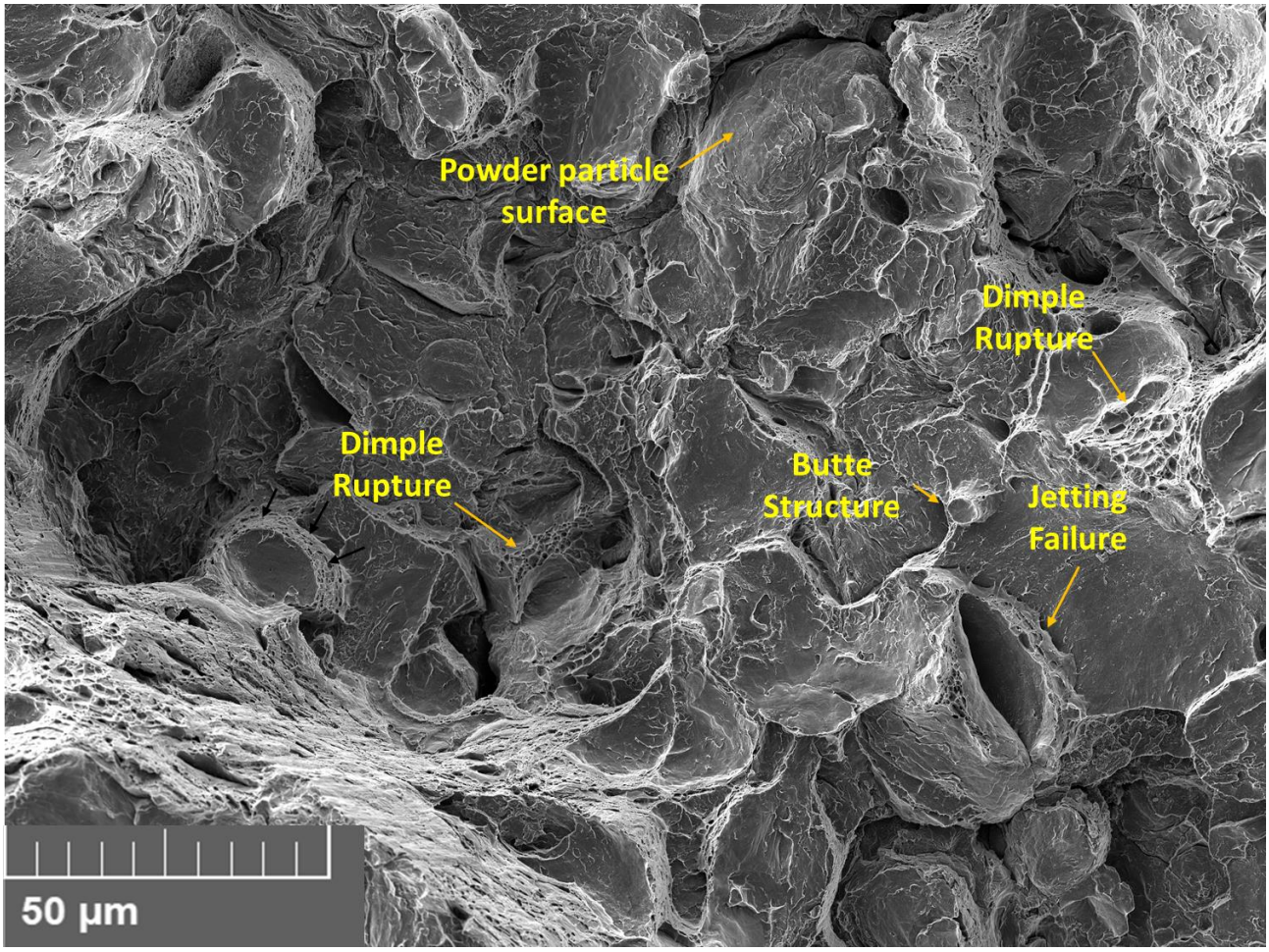

Figure 36 The AR fracture surface resulting from fracture mode 1 displays a wide range of fracture features of varying size and morphology. Fracture features of interest include surface areas of undeformed powder particle large butte-like structures and smaller features such as dimple rupture and jetting failure.

Higher magnification images in Figure 37 show a small butte structure with a round plateau approximately 5 µm in diameter with the largest being approximately 10x25 µm ellipse The small butte displays small diffuse shear lipping around the base of the structure suggesting some form of metallurgical bonding. A hole located at the top center of the image is of similar size and morphology to the small butte suggesting that morphological features are inversely related. The fracture surface also displays a range of surface are sub-micron dimple rupture which presents itself in a roughly equilateral triangle with side length of approximately 25µm.

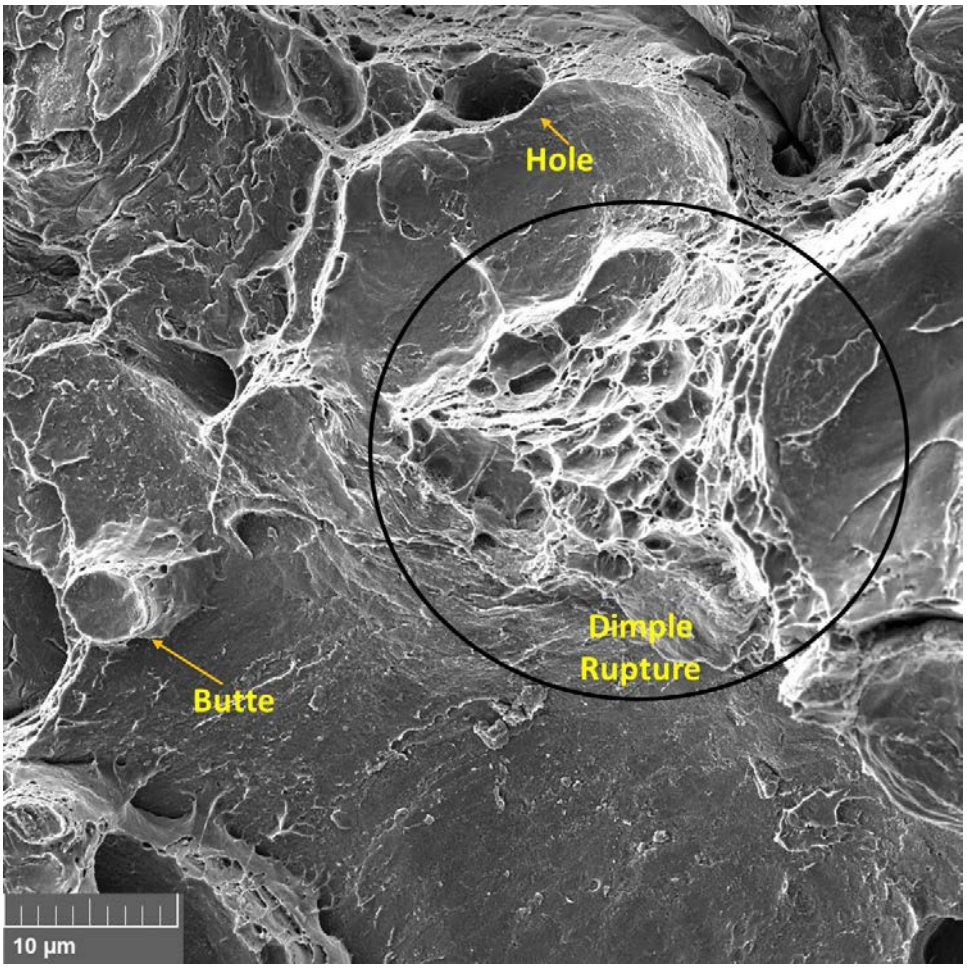

Figure 37 Is a higher magnification image of the AR fracture surface. A small butte-like structure can be observed at the bottom left corner with a potential corresponding hole located at the top center of the image. Large areas showing ductile failure can be seen adjacent to large areas which display little or not evidence of bonding.

Observable within the fracture surface is the failure of an individual splat approximately 30-40 microns in diameter which is consistent with process particle dimensions. In Figure 38 the formation of material jets can be seen close to an area of failure. The delamination of the splat reveals a small portion of the underlying surface which displays no signs of local ductility, but

instead has a smooth mechanically flattened appearance. Directly adjacent to the splat are two distinctively different areas of surface morphology. To the left of the splat concave areas with butte-like features with complex surfaces exhibiting diffuse shear lips and relatively smooth orthogonal faces. Conversely to the right of the splat the convex featureless surface which looks relatively undisturbed by particle impact.

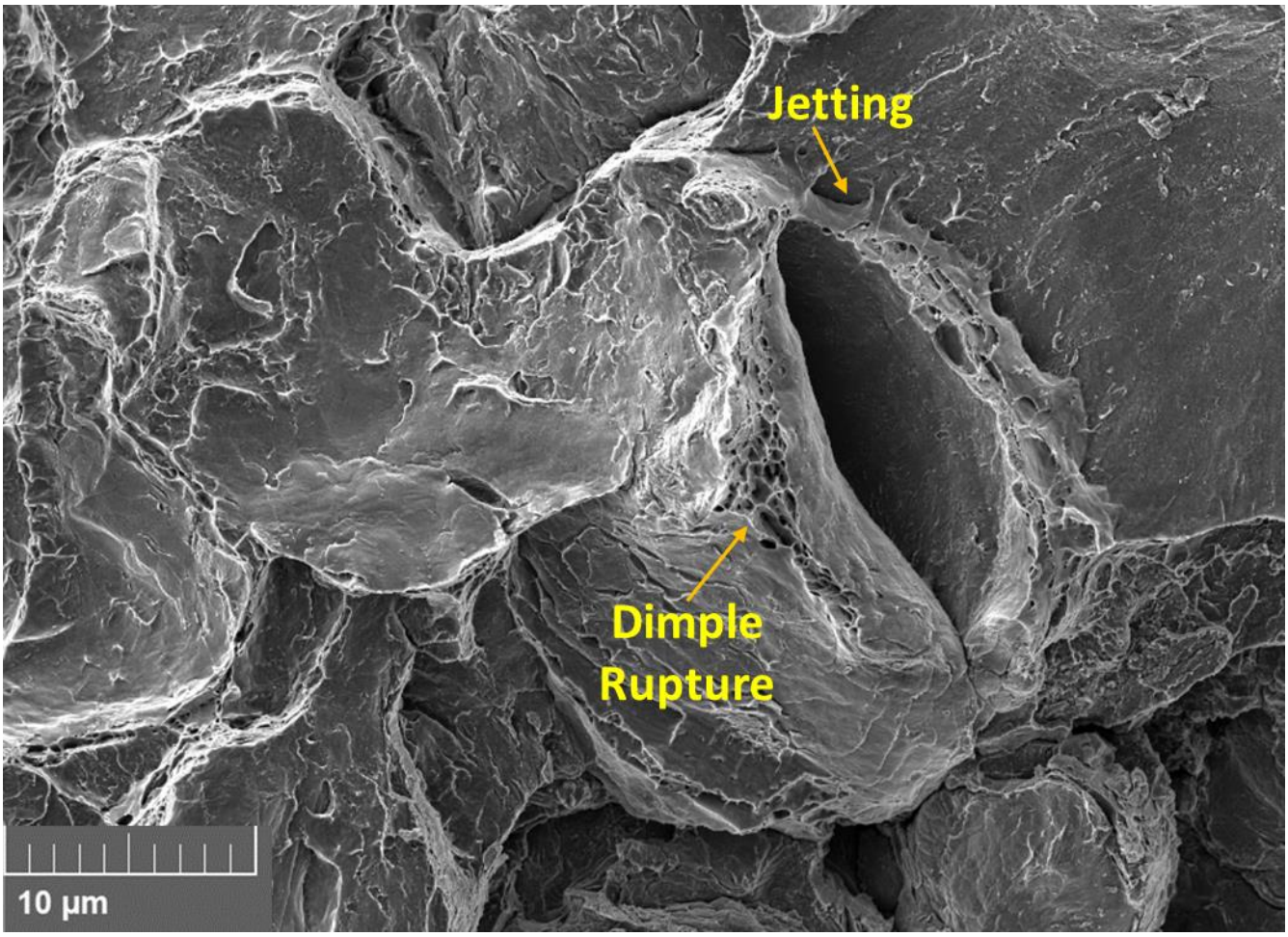

Figure 38 The jetting failure from Figure 37 at higher magnification which displays a flattened morphology characteristic of SPD and the CS process. Dimple rupture on the up turned edges is visible along with smooth flat interior morphology underneath the splat.

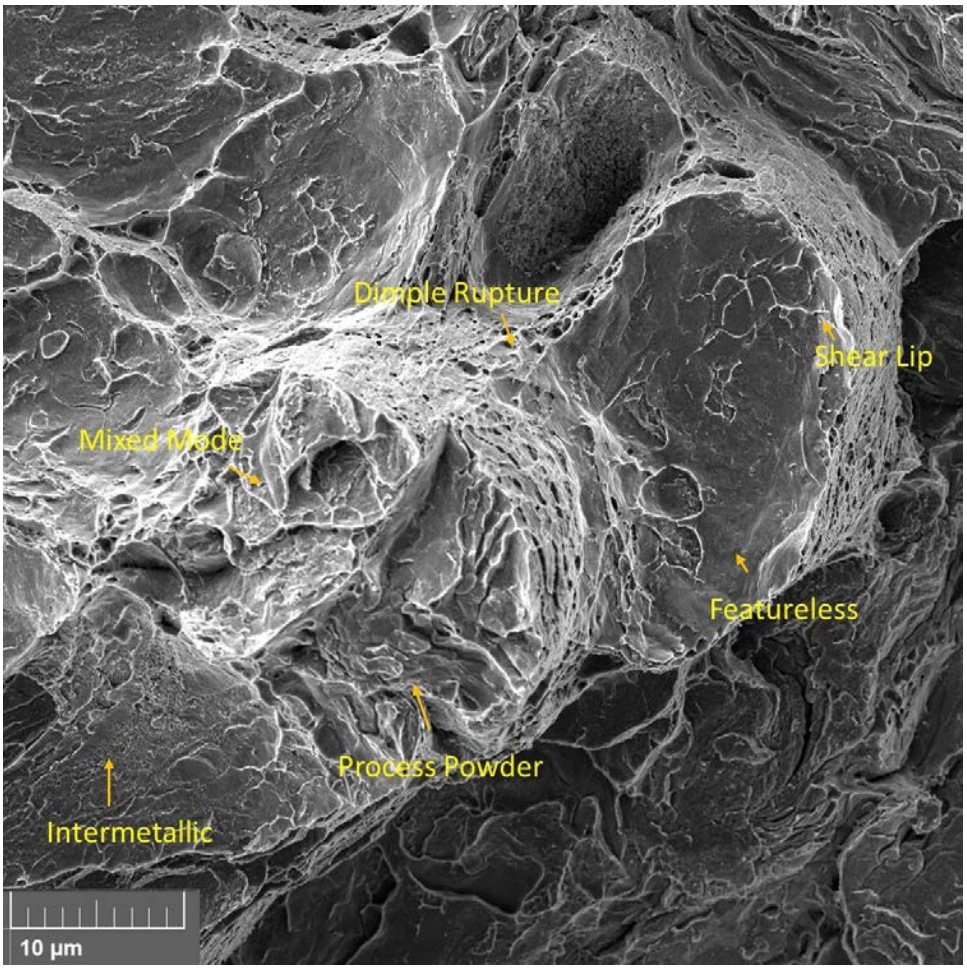

4.3.2 Fracture Surface of 10-hour Heat Treated Sample

Micrographs of the 10-hour heat treated fracture surface show a similar morphology to the AR samples which display large butte-like structures of varying size. The size and distribution of the average butte is homogeneous with the largest diameter approximately 30µm and the smallest being approximately 15µm. The plateaus of the buttes display a range of morphological features including smooth surfaces, shear lipping, and/or complex stepping. Areas between

buttes resemble the size and morphology of IDR with surfaces displaying characteristics of ductile failure and mixed mode failure.

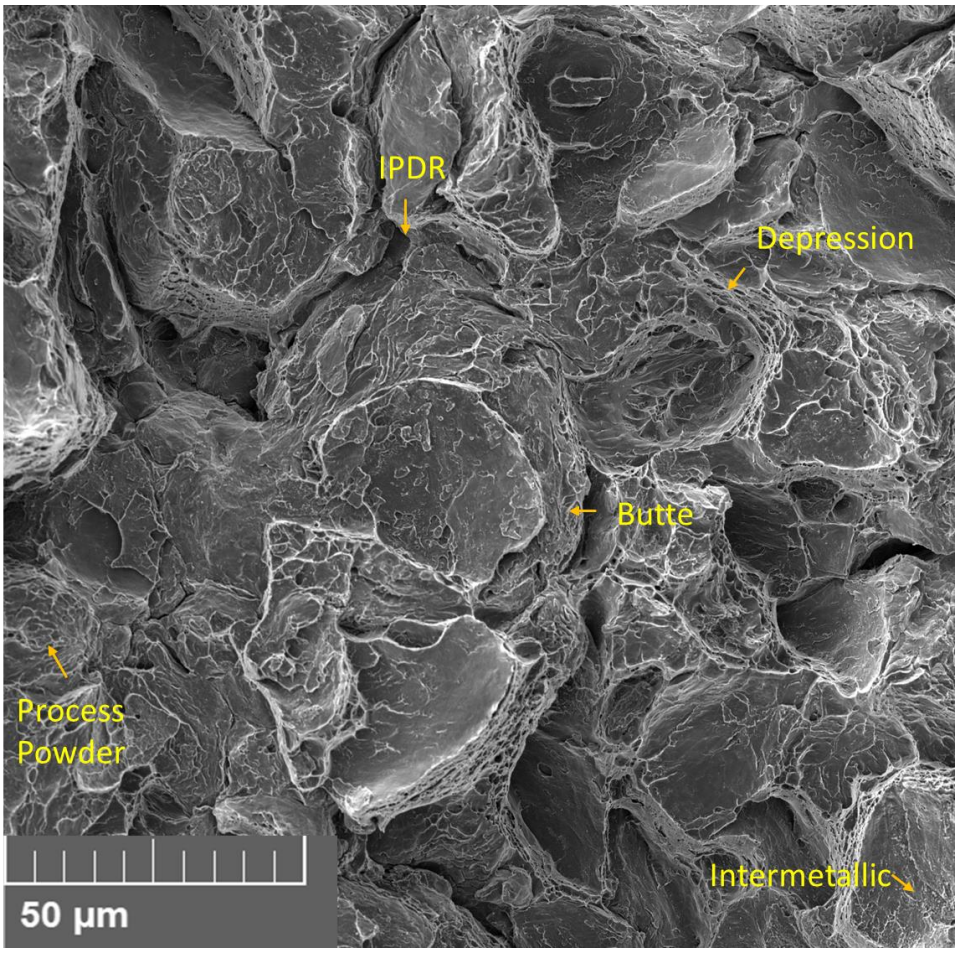

Figure 39 The fracture surface of the 10-HR heat treated sample after failure in fracture mode 1. Larger macroscopic fracture features are more easily visible at lower magnification while smaller features of interest are identified by boxes

Higher magnification micrographs in Figure 40 show the topography of more complex regions within the fracture surface and highlight the areas which exhibits ductility in the 10-hour sample. The upper left corner the micrograph shows a butte sized hole which displays the

characteristics of ductile failure. Within the microstructural feature are signs of localized ductility visible through the creation of micron length shear lips. A larger shear lip can be observed on the surface of an approximately 10-micron butte in the central portion, with more signs of ductile failure throughout the fracture surface. The characteristic powder particle surface in conjunction with morphologically flat areas and a large 10-micron defect can be seen in the lower right corner of the image.

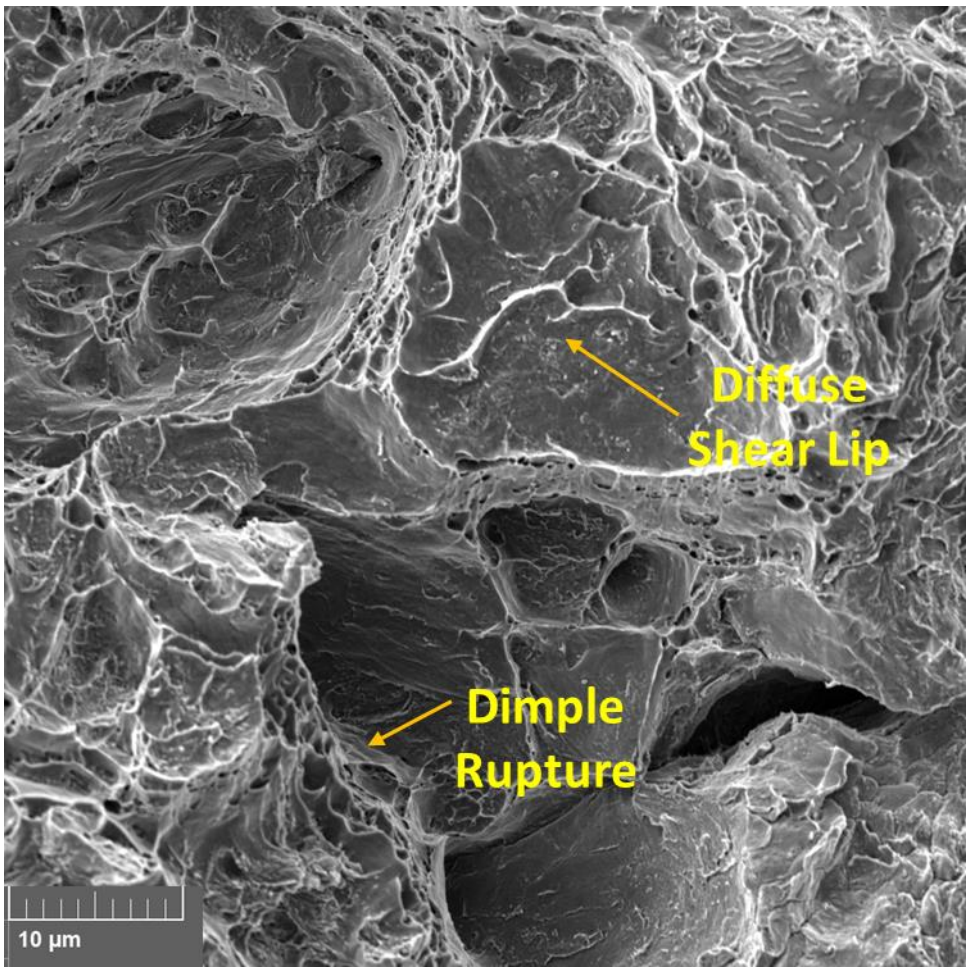

Figure 40 Is an inlay from Figure 39 which shows the morphology of the 10-HR heat treated fracture surface. Larger scale features such as particle pullout are seen along with evidence of ductile failure such as dimple rupture and presence of shear lips.

The figure below highlights areas within the bulk fracture surface that display non-characteristic failure mechanisms. The smooth face and secondary cracking observed across large surface areas displaying little or no dimple rupture are larger in size and not the correct morphology to be characterized as process powder particles. In the upper central portion of Figure 41 is a powder particle size hole which shows no signs of ductility.

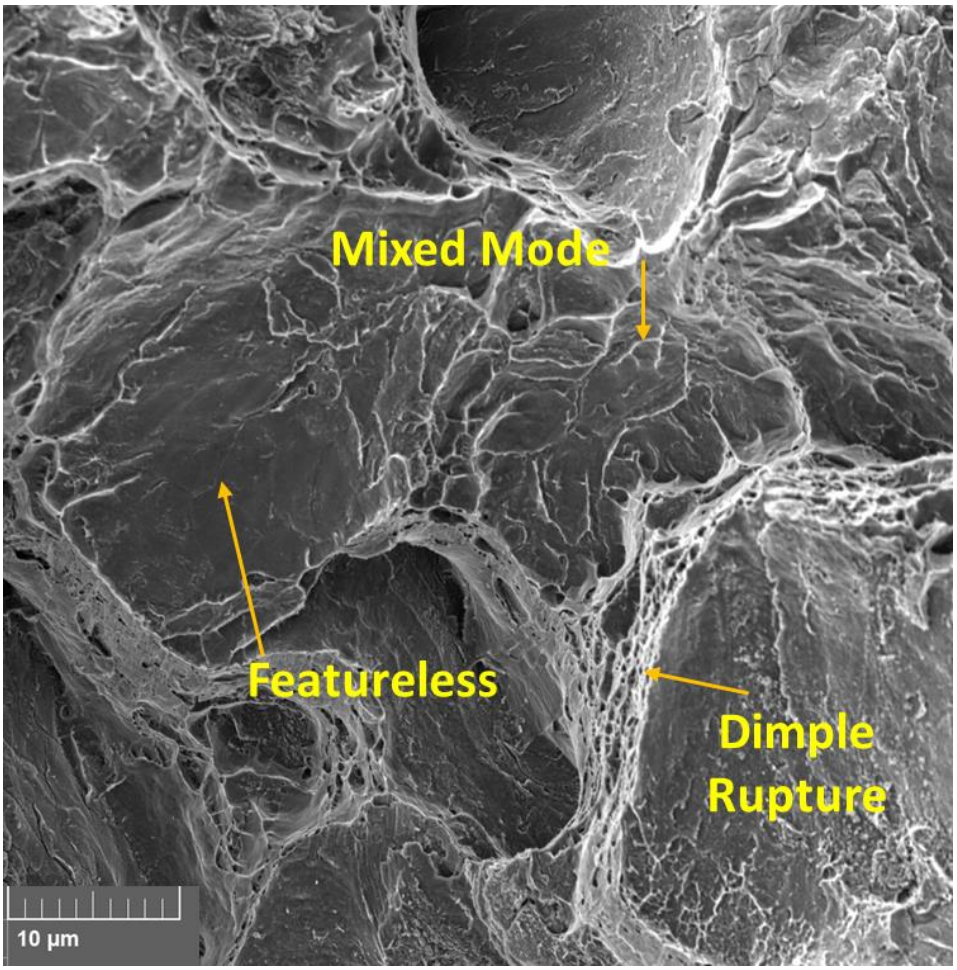

Figure 41 Is the second inlay from Figure 39 which shows an area within the bulk that shows less direct evidence of ductile failure. Flat areas void of microstructural features can be observed near areas with more complex stepped surface morphology.

The micrograph in Figure 42 shows an area of the 10-hour heat treated sample that is consistent with the bulk of the sample but depicts a more extreme landscape. The characteristic

surface morphology of a powder particle can be seen in the top central portion of the micrograph displaying non-characteristic failure in the areas associated with MDR and HDR or jetting. Below the splat is a large process powder sized depression displaying cup and cone morphology with diffuse shear lipping covering the surface.

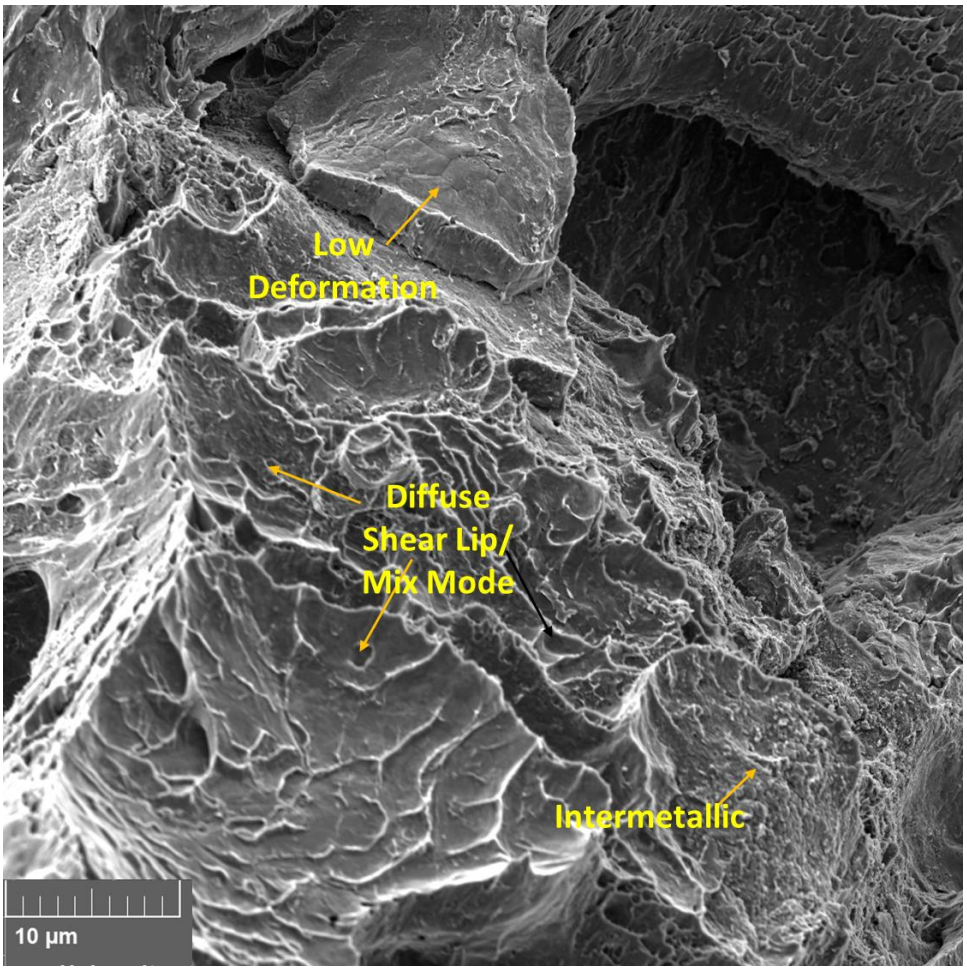

Figure 42 Is of a second site sample from within the 10-HR bulk and shows a tortuous land scape that shows signs of ductility across various size scales. Points of interest in the image include an individual splat which exhibits failure along peripheral edges and small particulates on the surface.

4.3.3 Fracture Surface of 100-hour Heat Treated Samples

Samples heat treated for 100 hours show morphological features consistent with the AR and 10-hour samples with Figure 43 showing the characteristic plateaus of numerous buttes. The buttes seen in the upper left corner of the micrograph have a distinct concavity and size which is much larger than the size of the process powder. The plateau of the buttes in this area has a complex surface with little in the way of disuse shear lips and some more local regions presenting as featureless in nature. More centrally located within the micrograph is a plateau area with a different complex surface in which stepping on multiple scale regimes can be observed. Dimple rupture on multiple scales can also be seen in the fracture surface with dimpling relegated to areas between and adjacent to buttes. The morphology of the areas between the buttes associated with the IDR has also changed when compared with the 10-hour samples. The width and length of the areas is more consistent with the morphology of the IDR and the surfaces are less angular, more orthogonal, and seem to exhibit complex surfaces and a larger distribution of diffuse shear lipping not seen in the 10 hour sample.

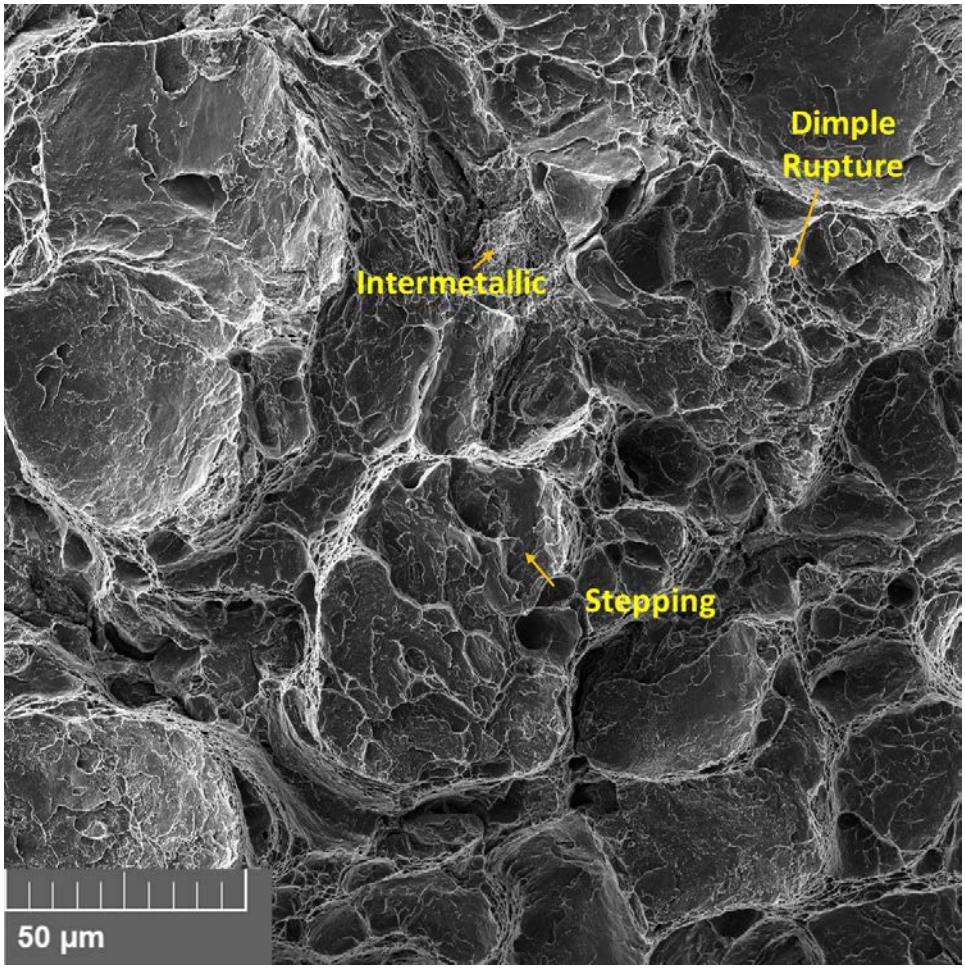

Figure 43 A low magnification microscopic image of the 100-hour HT fracture surface. Characteristic butte structures can be seen with varying degrees of stepping, as well as intermetallic compounds on the surface.

The butte and portion of the fracture surface that is most characteristic of ductile failure is presented in Figure 44 below. At higher magnification the fracture surface of the 100 HR samples shows evidence of ductile failure by way of dimple rupture. The size, scale, and distribution of the shear lips as well as diffuse shear lips on the complex surfaces can be observed throughout the entire image. The fracture surface shows multiple size scales of ductile failure as well with large cups exhibiting size ranges of 10-30µm and much smaller features

within large cups ranging from 2-5µm. Large areas littered with intermetallics are also visible in central lower potion of the image juxtaposed to an interesting flap like fracture feature.

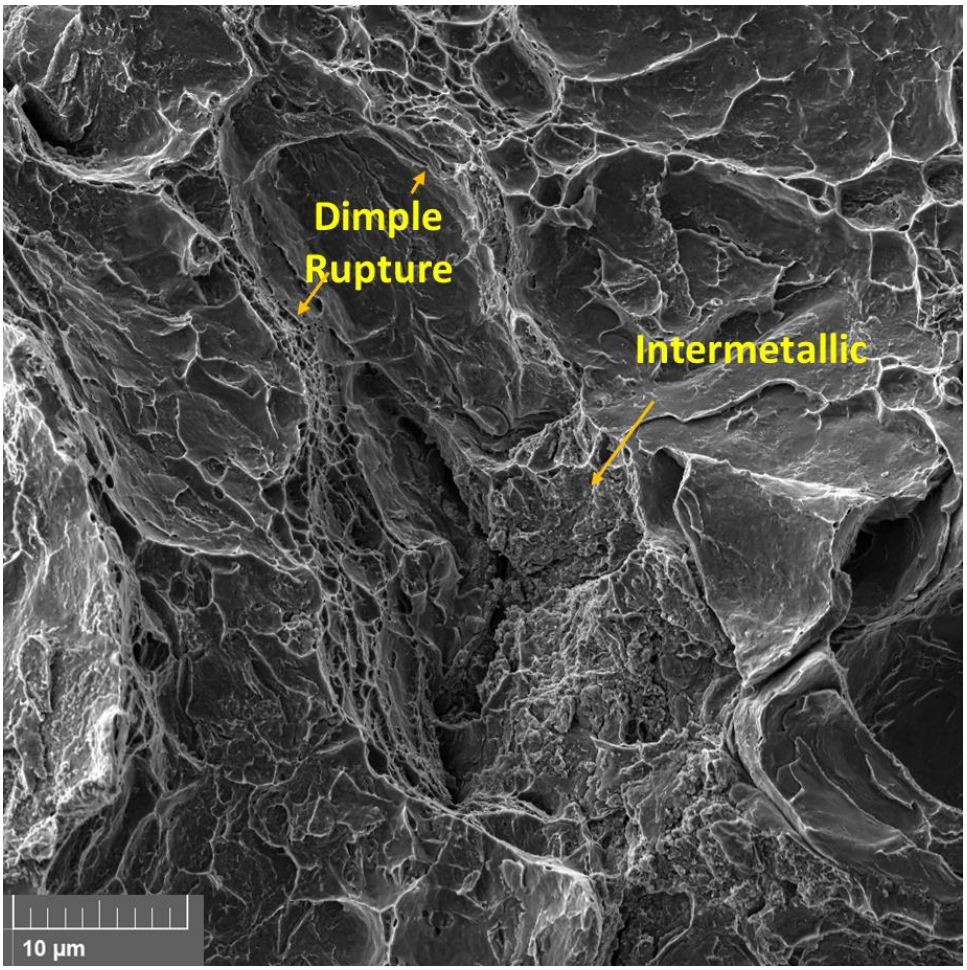

Figure 44 Higher magnification images which show clear signs of ductile failure. Intermettalics can be seen adjacent to a overlapping flap of seemly ductile material.

Another of the buttes that displays non-characteristic failure is show below in Figure 45. The plateau of this butte shows a complex surface in which the crack propagated up and over the microstructural feature rather than cleaving through the butte.

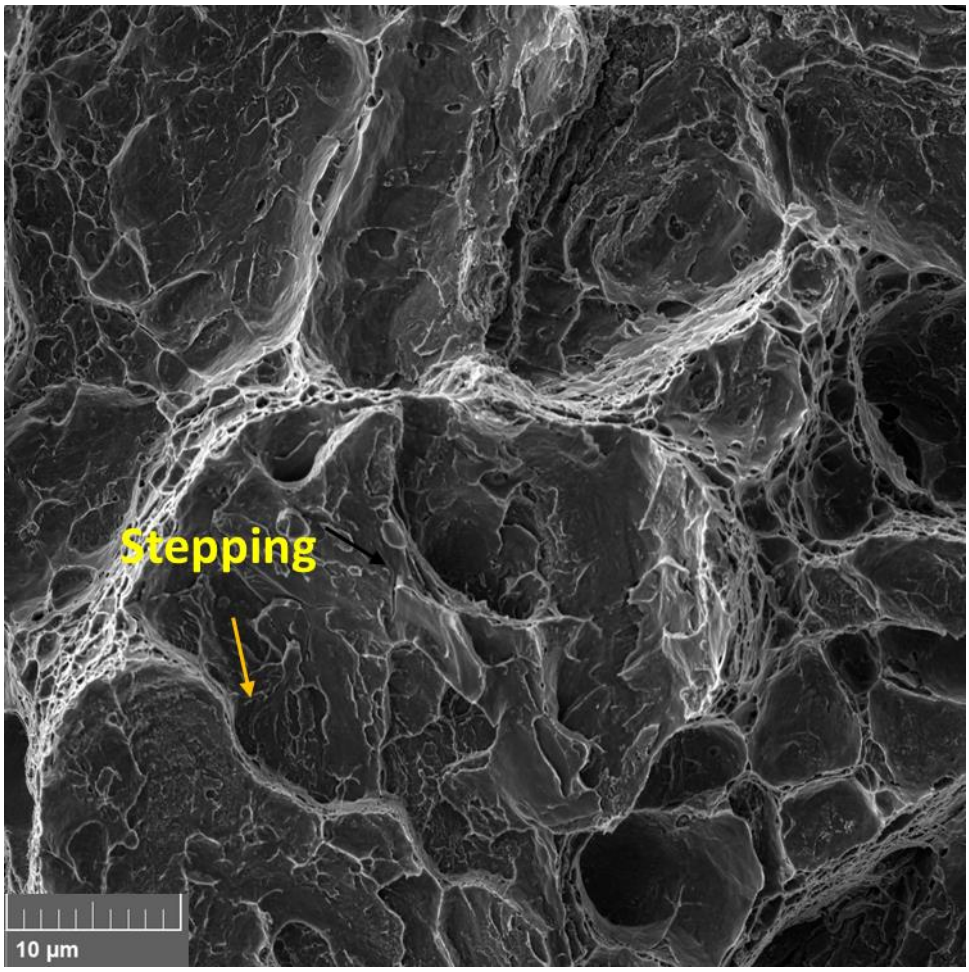

Figure 45 Micrographs of microstructural fracture features that show less signs of ductile failure.

4.4 Electron Back Scattered Diffraction of Sub-Fracture Microstructure

4.4.1 EBSD - As Received Samples

Cross section of the fracture surface at low magnification are presented below in **Error! Reference source not found.**, with the top image showing the edge on view of the fracture

surface in the parallel to the as-sprayed direction. The second image is of the cross section of the fracture surface in the (X,Y) orientation. White boxes outline areas within the fracture surface where EBSD data was directly taken from. The macroscopic presentation of the fracture surface shows a fracture line with Sharpe angular and small distinct fractures.

Below in Figure 48 is the first site for the AR samples which was chosen due to its location on the fracture surface and its correlation to its underlying microstructural feature, a butte. The size and morphology of the fracture feature seen in the SE image are of the same approximate size of the butte features observed in the fracture surface. As can be seen in Figure 48 the extreme degree of edge rounding seen at this magnification drastically reduced the SEM capability to resolve kikuchi patterns. The maps produced show grain sizes that suggest the area indexed underneath the butte-like structure falls into the LDR, but little was gained from direct observations of fracture feature with a low amount of edge retention. The size and scale of the area around the core of the EBSD map are consistent with the size and morphology of other regions, but scan time and required beam parameters related to indexing fine grains within the imaged area would be poor.

Higher magnification EBSD scans with smaller step size were taken to ascertain more information on the underlying microstructure of the indexable area. Shown in Figure 49 is transition area or area where the SEM struggled to resolve band patterns and shows an area with a relatively small grain structures displaying a large degree of misorientation along the unresolved area suggesting that misorientation may not be the dominating factor in prediction crack path propagation. The size and morphology of the indexed area within Figure 49 suggest

that with alterations to the scanning conditions smaller grains could be resolved withing the non-indexed area. The contract change in the SEM image are consistent with the transition zones from LDR to MDR/HDR.

The images in Figure 50 below show the second site from the AR sample which consists of an area of the fracture surface where the crack propagation resulted in a less free standing fracture feature, and focusing efforts on indexing a less pronounced fracture feature. The EBSD image shows the existence of a very fine microstructure beneath the fracture surface consistent with HDR and LDR. A step size of 0.5µm use to acquire data from the large image and thus the post processed image provides part of the microstructural information. Raw data is also show below and the characteristic round tear drop shape of the underlying XY microstructure can be observed along the primary crack with the crack path seeming to pass through the IDR. At lower magnifications which less stringent beam conditions the RAW data provides more insight into the under lying microstructure associated with failure.

Site 3 was chosen as a mixed mode spot as it has similar morphological characteristics to both site 1 and site 2 while also displaying a large secondary crack. Initial EBSD images of the surface show similar results seen in sites 1 and site 2 with a what present as MDR and HDR beneath the fracture surface. Little information about the bulk material was gained from scanning such large areas with at high resolution, but raw data provides insight into gross

morphological characteristics of the underlying microstructure similarly seen in the previous microstructure. Unlike the previous underlying microstructure, the primary fracture feature seen in the RAW data of the AR sample shows elongation of the underlying bulk material and not the characteristic tear drop shape. While the raw data suggests there may be the presence of UFG, the beam conditions and the 0.5 µm step size suggest these are highly misoriented LDR grains.

While edge rounding remains a persistent problem with imaging the absolute edge of the fracture surface, the SEM was able to better resolve the microstructure surrounding secondary cracks. The secondary crack in Figure 54 presents a microstructure most like that of the MDR but does show the presence of sub-micron grains. The grain size along the crack tends to be of micron size in nature and display a large degree of misorientation to grains on the adjacent side of the secondary crack.

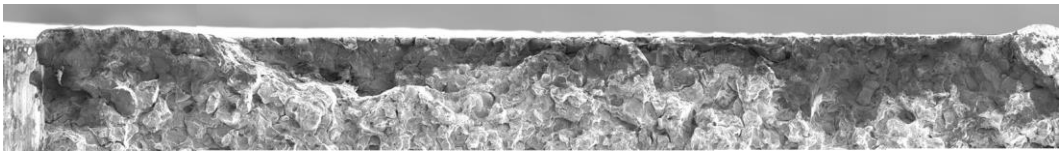

Figure 46 The edge of the fracture surface is visible from a top down orientation. This perspective of the fracture surface is parallel with the as-spray direction, and the morphology is similar to what was seen in prior fracture surface images

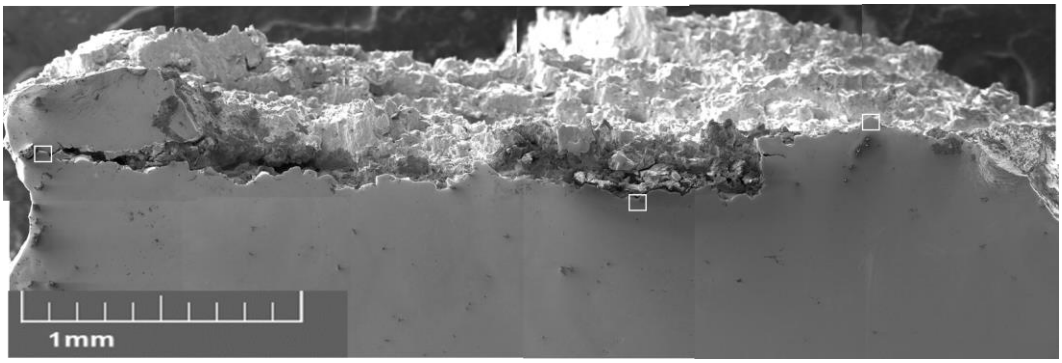

Figure 47 The same edge of the fracture surface seen above, but oriented perpendicular to the As- sprayed direction. White boxes highlight the areas selected for EBSD.

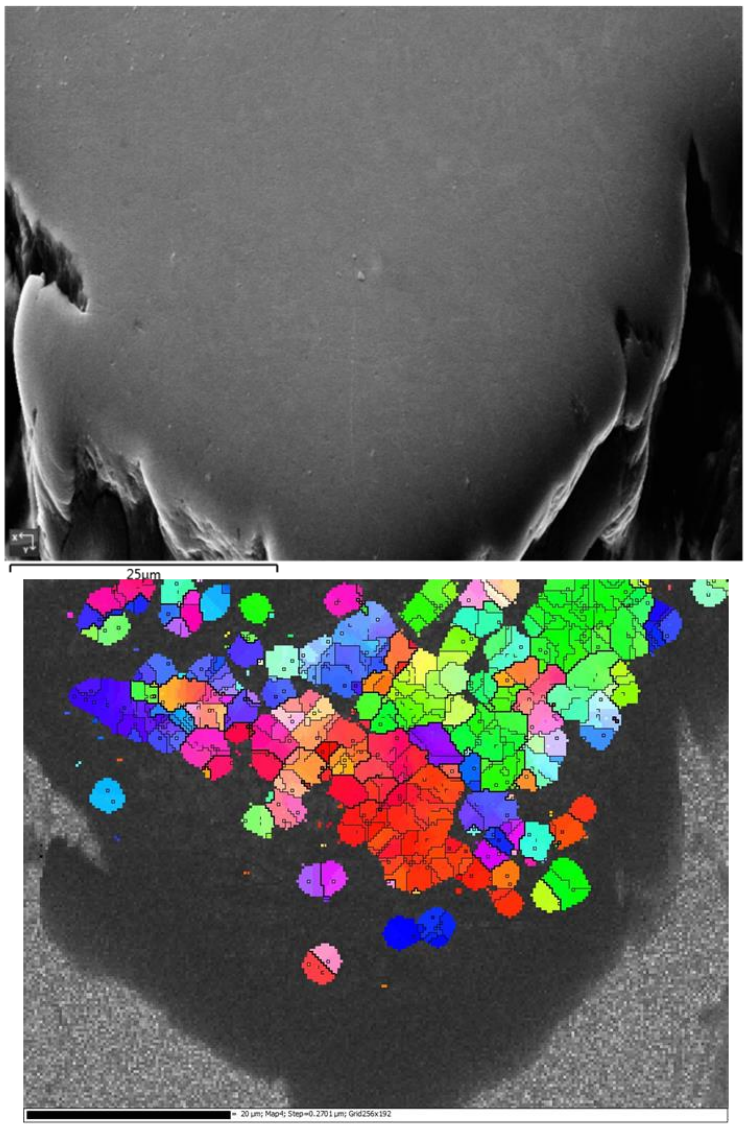
25µm
IPF colouring
Z0
Aluminium
111
001
101

Figure 48 SE images followed by the post processed EBSD map. This site highlights the difficulties encountered with high resolution EBSD because of edge rounding.

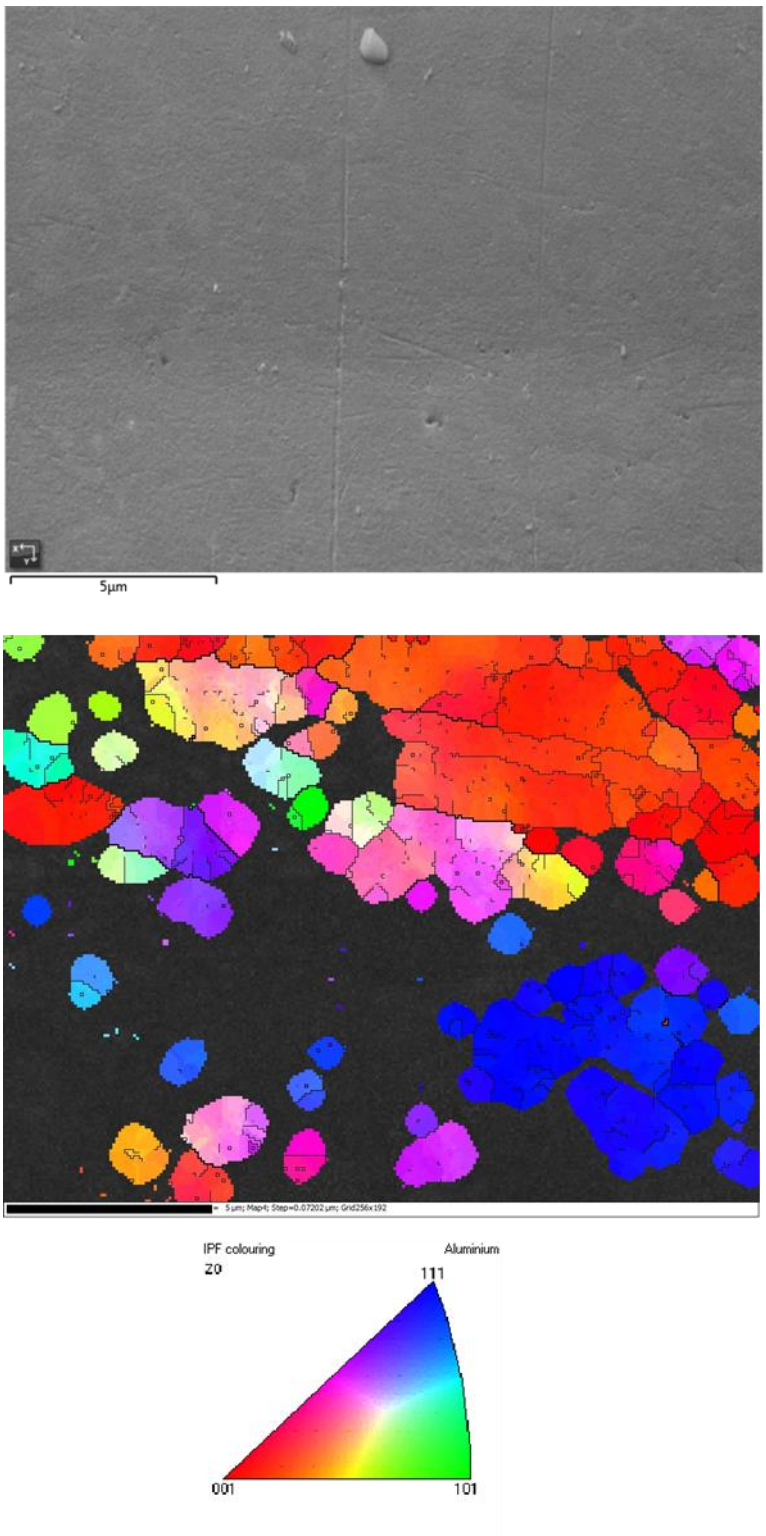

Figure 49 Higher magnification characterization of the bulk microstructure. The size and morphology suggest this belongs to the MDR.

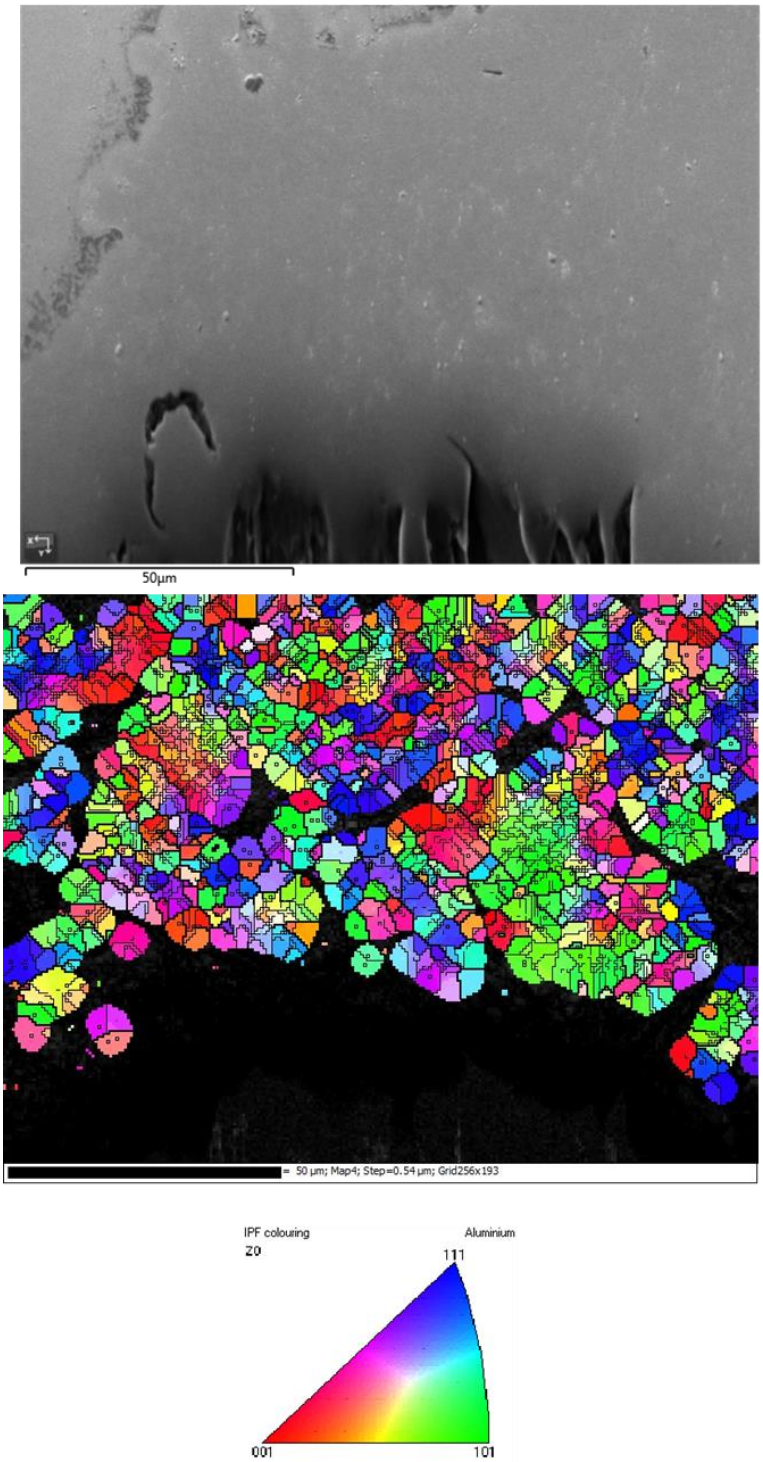

Figure 50 SE top image, taken at lower magnification with step size .54 m, shows the edge rounding associated with the fracture surface while the corresponding EBSD map below shows the underlying microstructure.

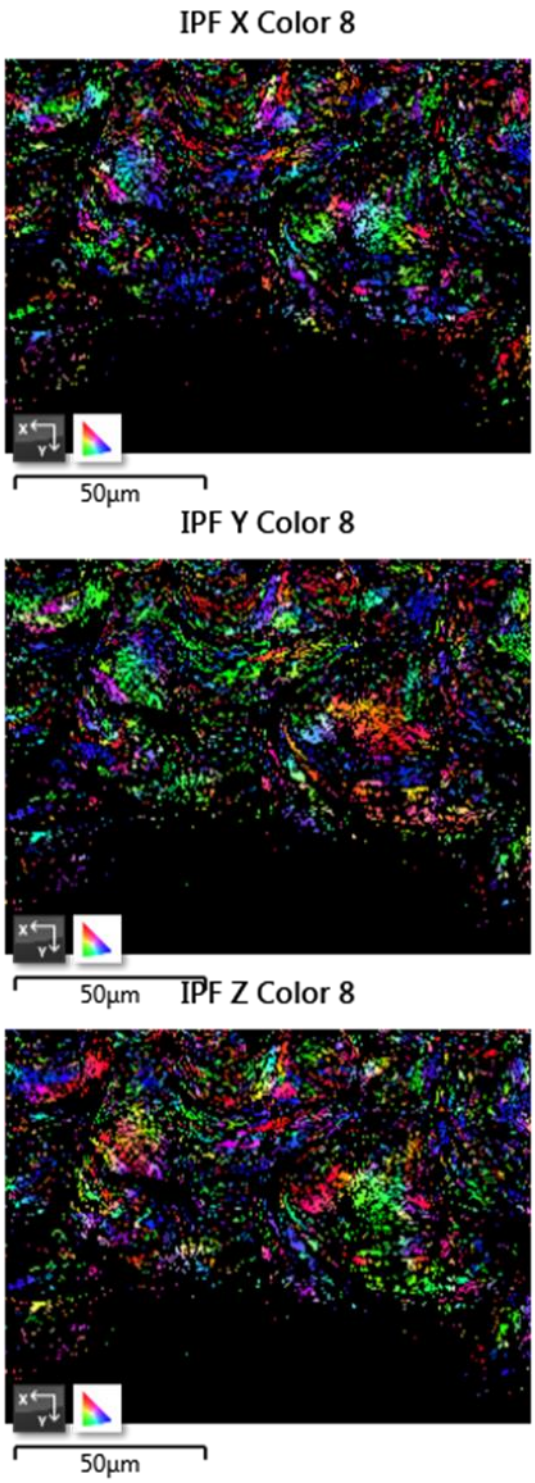

Figure 51 The unprocessed orientation map collected from site 2 and highlights the characteristic nature of the CS microstructure in the XY direction.

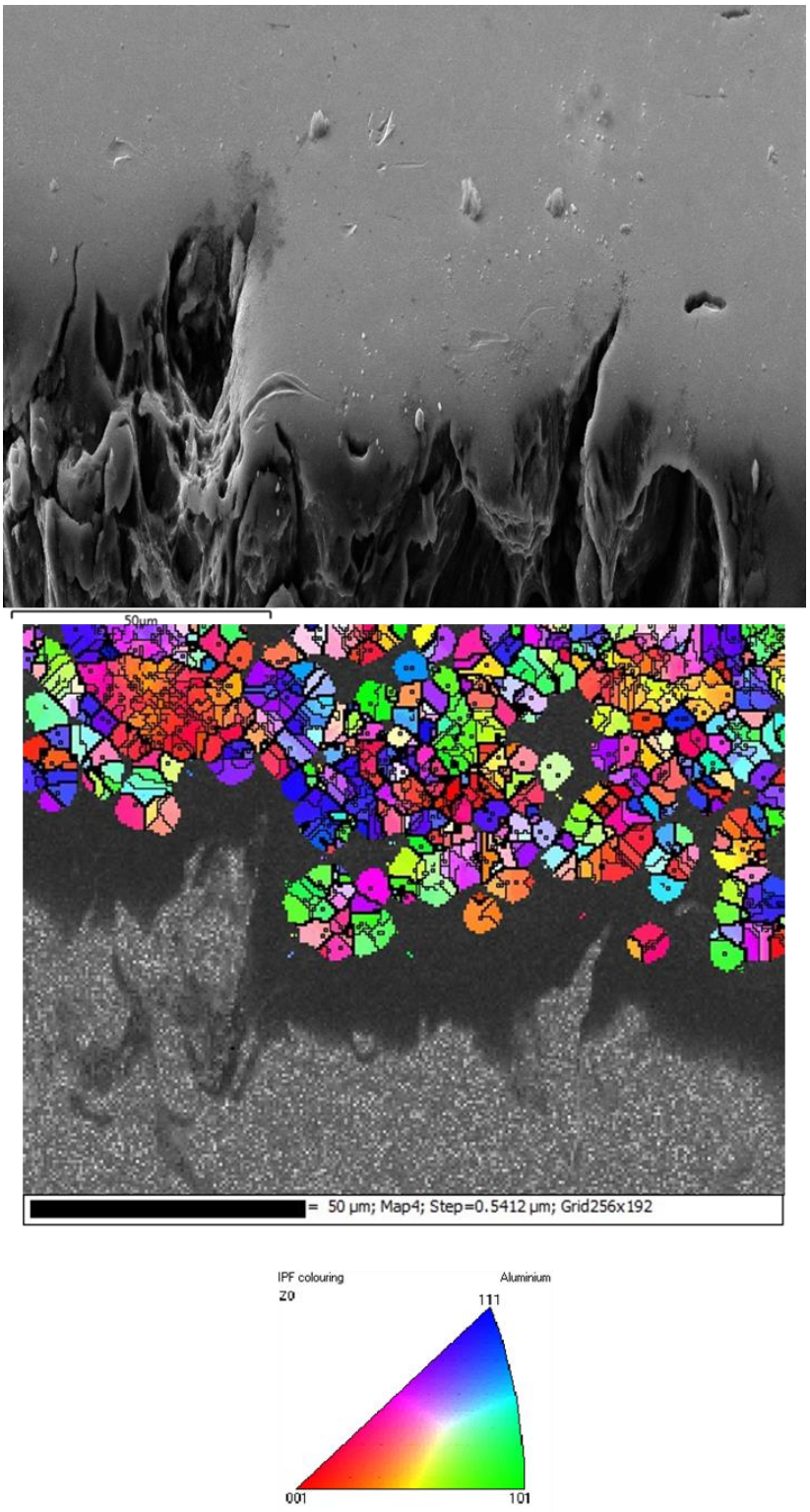

Figure 52 Site 2 which was chosen as it is similar in appearance, size, and morphology as complex butte-like structure that may exhibit stepping like fracture behavior. The top SE image shows the primary fracture path with side cracking.

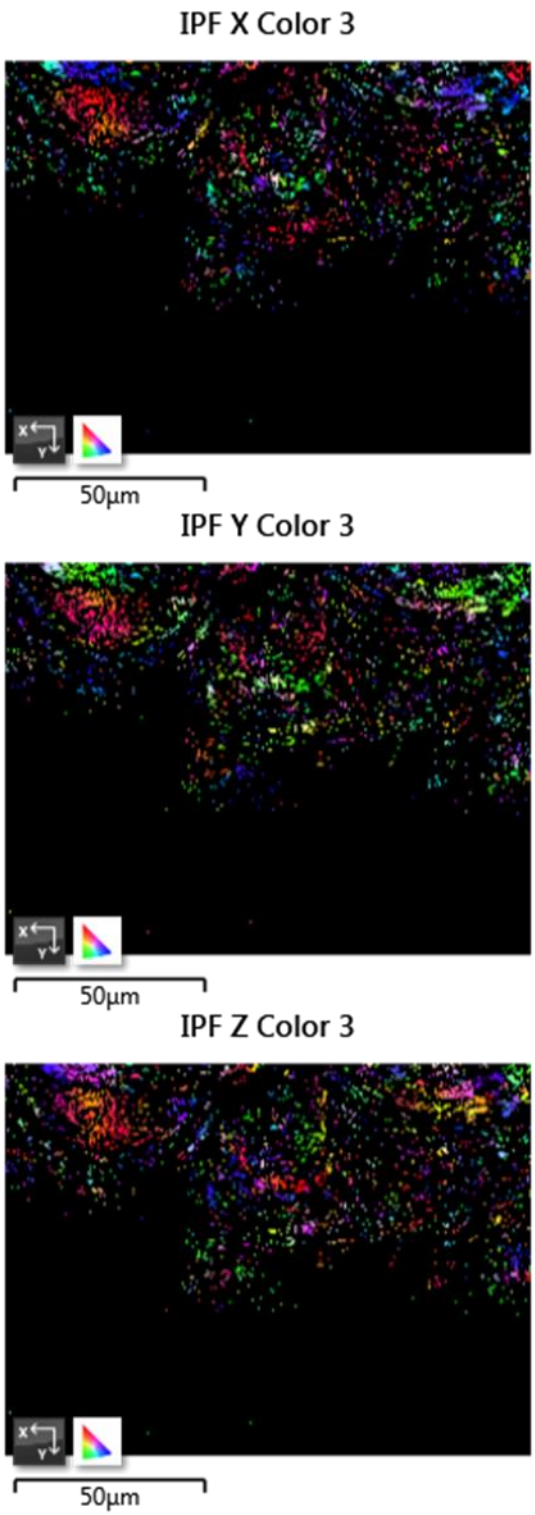

Figure 53 The unprocessed orientatio map associated with site 3. Morphology of this fracture feature exhibits less round morphological features.

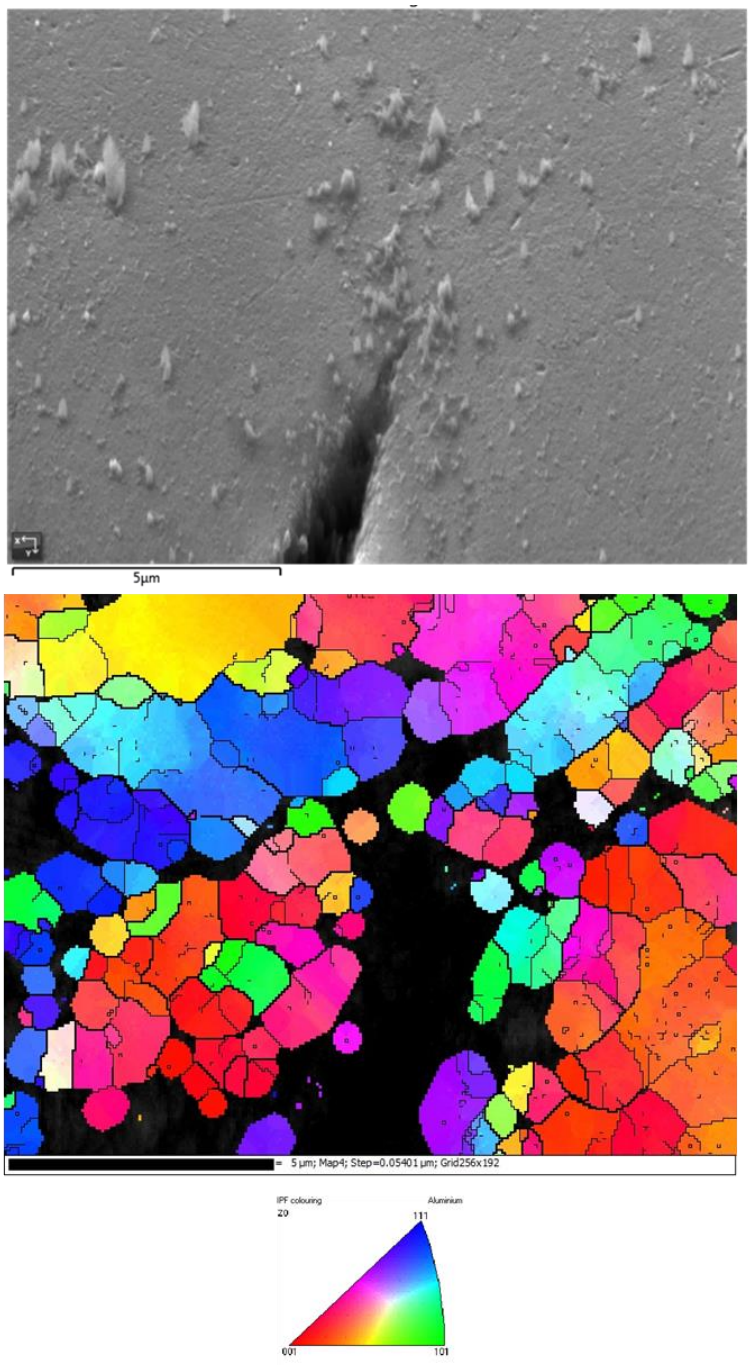

Figure 54 A secondary crack in the AR fracture cross section. Post-processed EBSD maps show the grain orientation and morphology of the AR microstructure surrounding the secondary crack. Top SE image shows particulates which are most likely remnant polishing media

4.4.2 EBSD - 10HR HT Samples

Difficulties in indexing the absolute edge of the fracture surface led to more investigation into secondary cracking seen within the bulk. The first site selected from the 10 hr HT was a deep secondary crack with notable rounding around the edges. The EBSD map in Figure 55 shows the indexed grains surrounding the secondary crack lay within the MDR and HDR.

The second secondary crack site selected can be seen below in Figure 56. The secondary crack can be seen propagating completely around a splat sized fracture feature of approximately 25-35 µm. The EBSD image of the fracture feature indicate that the affected area is most closely associated with again with the MDR and HDR.

Another scan aimed at indexing a potential butte complex can be seen below in Figure 57. The absolute edge of the fracture can be seen relatively well preserved with little signs of edge rounding. The EBSD image shows indexed grains that fall within the HDR. This fracture feature is most similar in morphological size and shape with either a butte complex or a splat at approximately 30 µm.

A last scan which indexes the absolute edge of the fracture surface was taken at site 4 where the sample geometry and beam sample orientation optimization were maximized. The SEM was able to resolve some of the microstructure beneath the fracture surface with the majority if the grains indexed falling in the MDR and HDR.

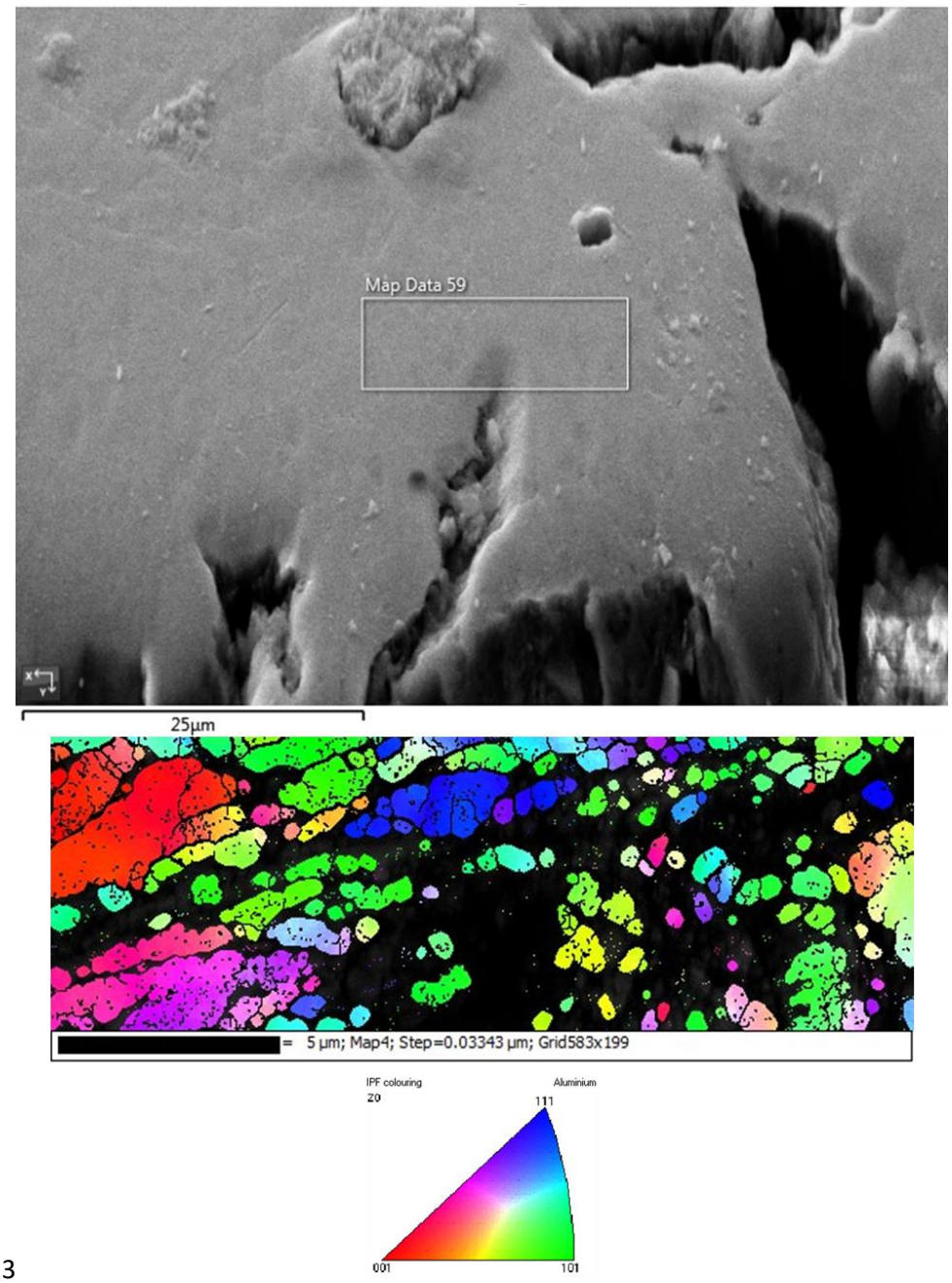

3

Figure 55 A secondary crack formed after failure of the 10hr HT 6061 CS Al. The top image is the SE SEM image which shows the area chosen for EBSD. The corresponding EBSD map is presented with the accompanying

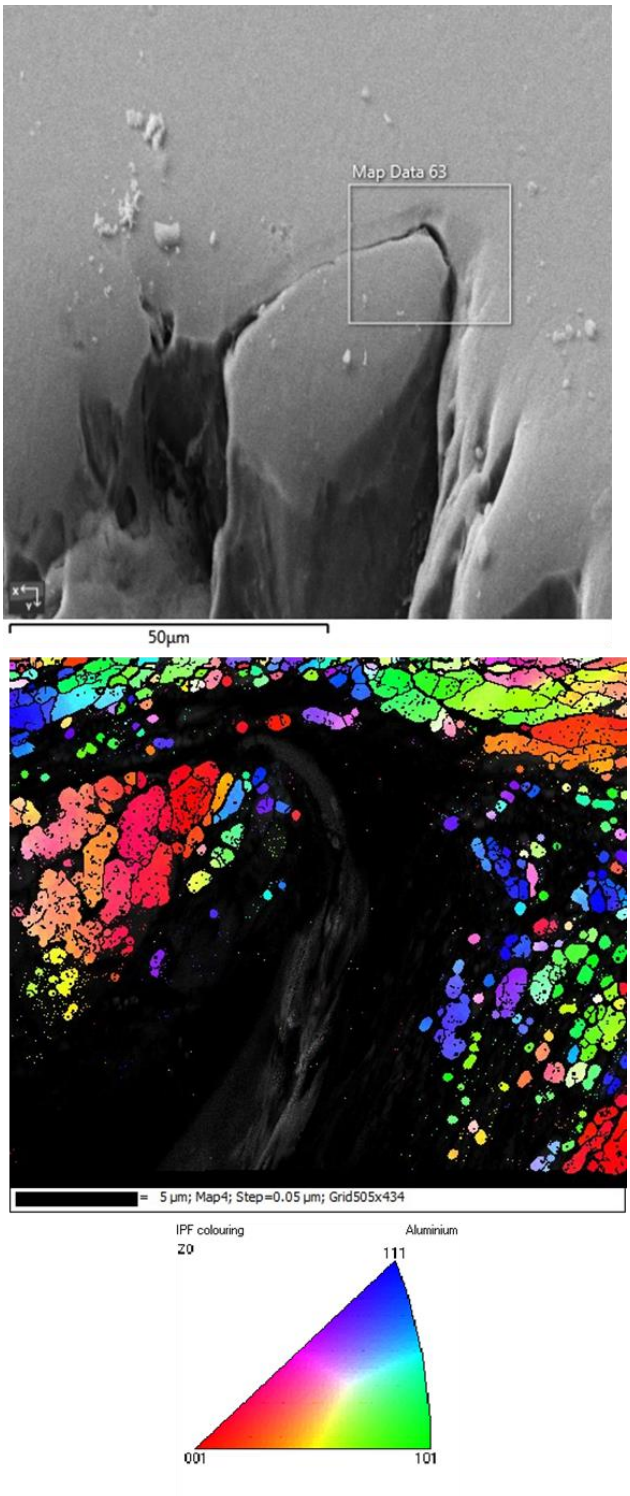

Figure 56 An approximately splat sized fracture feature which the crack has propagated through. The top SE image is of the primary crack with secondary surrounding a larger microstructural feature with similar dimensions to a particle.

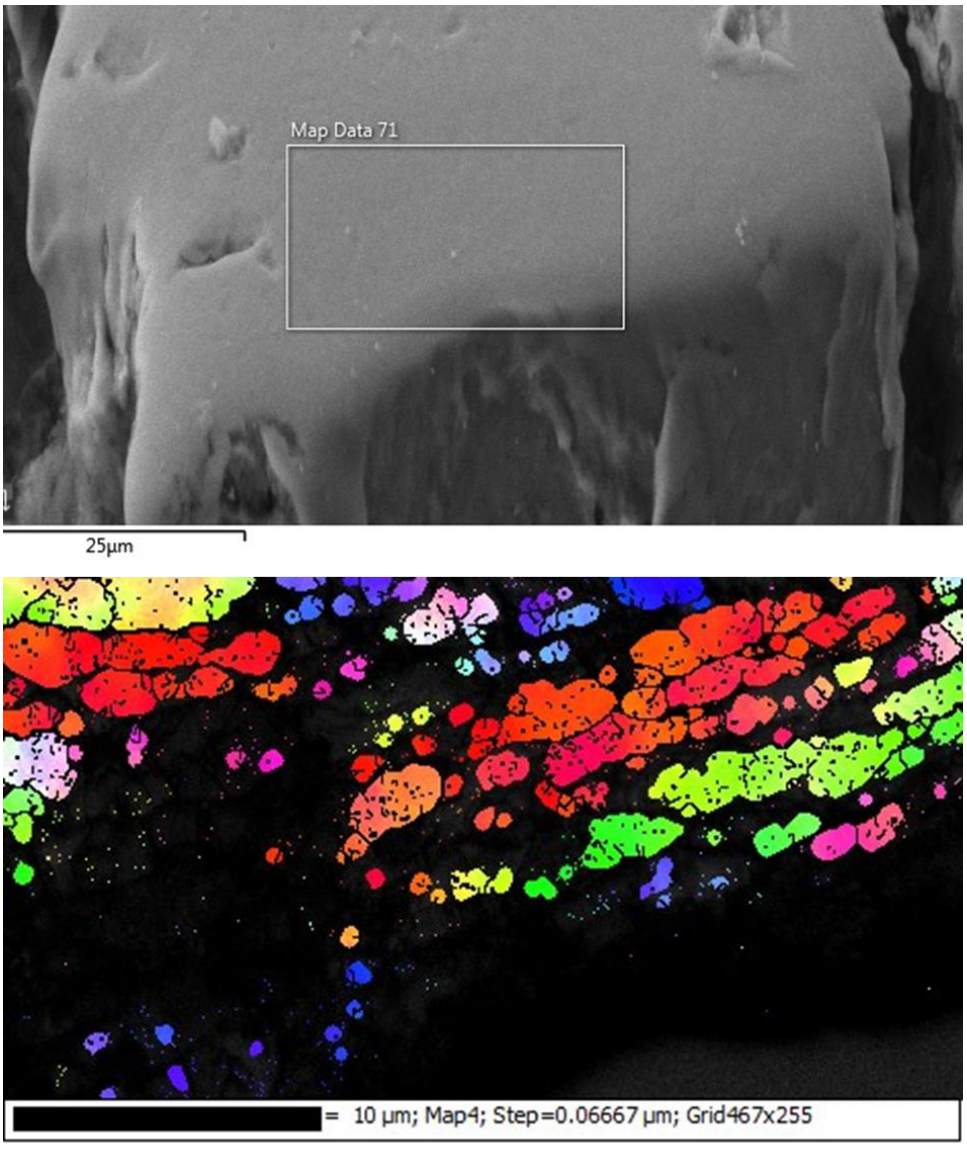

Figure 57 Site 3 which is morphologically like a large butte structure or individual splat. The EBSD image suggest this area is of the HDR

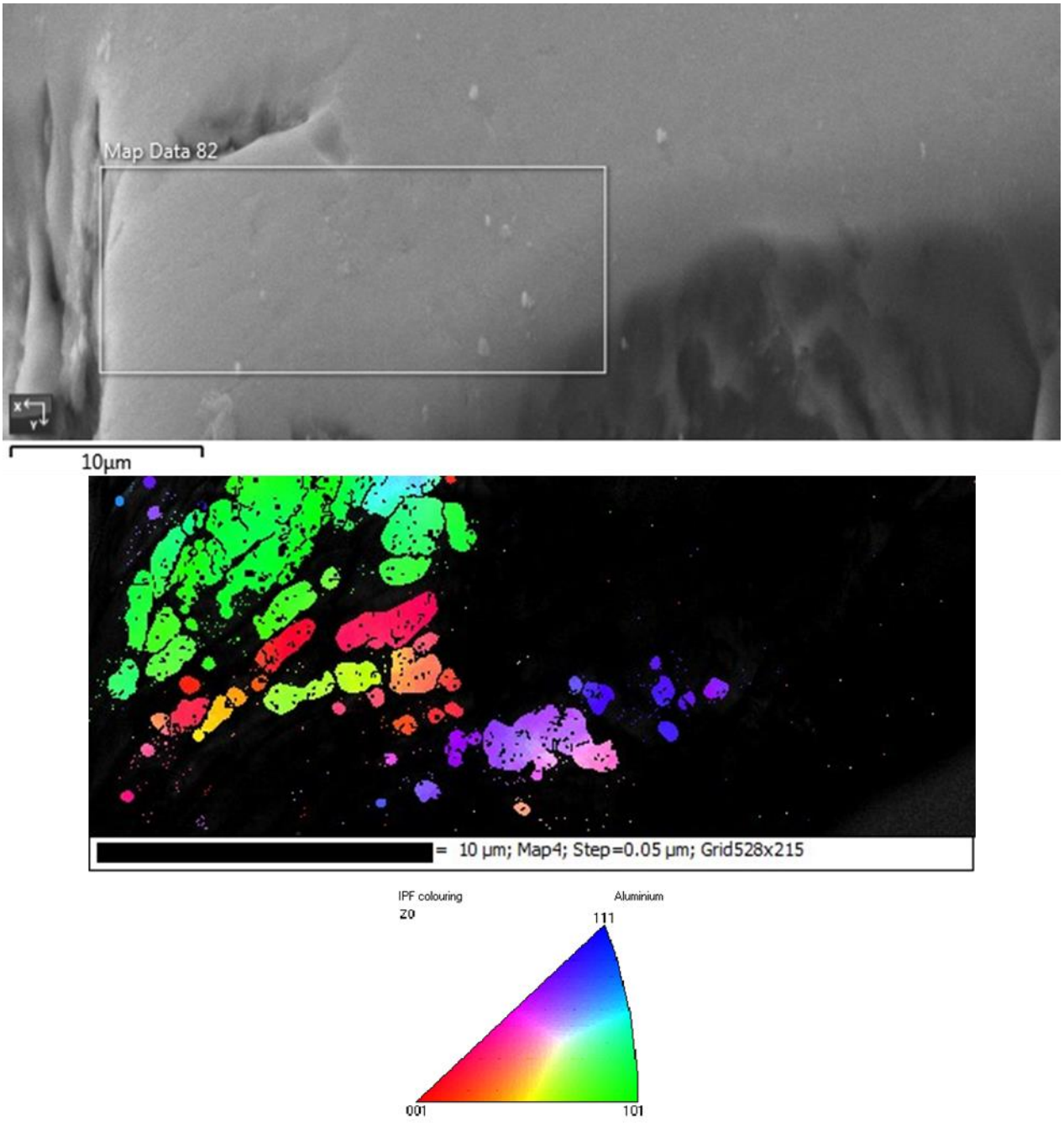

Figure 58 The SE SEM image of the primary crack. This EBSD scan was optimized such that the absolute edge of the fracture surface could be indexed. The corresponding EBSD map below shows the underlying microstructure associated close to the fracture edge.

4.4.3 EBSD - 100HR HT Samples

The first area investigated on the 100 hr HT sample is an area which encompasses the edge of a secondary crack which has propagated from the primary and can be seen below in Figure 59. This area was selected because the edge retention of this area was well preserved and free of oxides and intermetallic compounds. The EBSD map in Figure 59 shows resolved grains which are best categorized ad MDR and HDR with the range of size within the EBSD image suggesting that this is also a IDR.

The second site from the 100 hr sample is the edge of the primary crack. The total size and morphology of the fracture feature at approximatly 35 μm and is cosistent with the butte structure found throughout the fracture surface. The EBSD image of the primary crack suggests that the microstruture adjacent to the crack is associated with th HDR and MDR. The EBSD map aslo shows a high degree of mis-orentation within the IDR.

Site 3 captures a small portion of a tertiary crack associated with a much larger tertiary crack. The morphology and positioning of the feature with respect to the larger crack suggests that this is a tertiary crack as opposed to an entrained defect. The EBSD map of the feature shows that the tertiary crack is preferentially propagating through the IDR in the area which exhibit the smallest average grain size. This area also exhibits a large degree of mis-orientation with respect to individual grains indexed within the image.

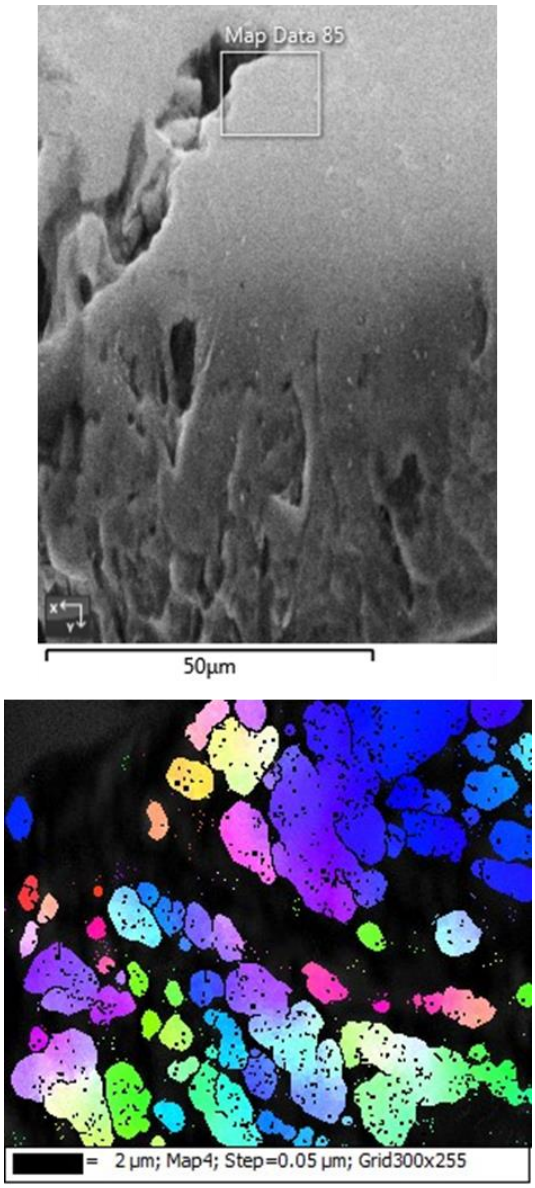

Figure 59 Site 1 chosen for the 100hr sample the top image shows the EBSD map with respect to the secondary and primary cracks. The edge of a secondary crack can be seen with the EBSD map below showing micron and sub-micron grains characteristic of the IDR seen in fig (!35).

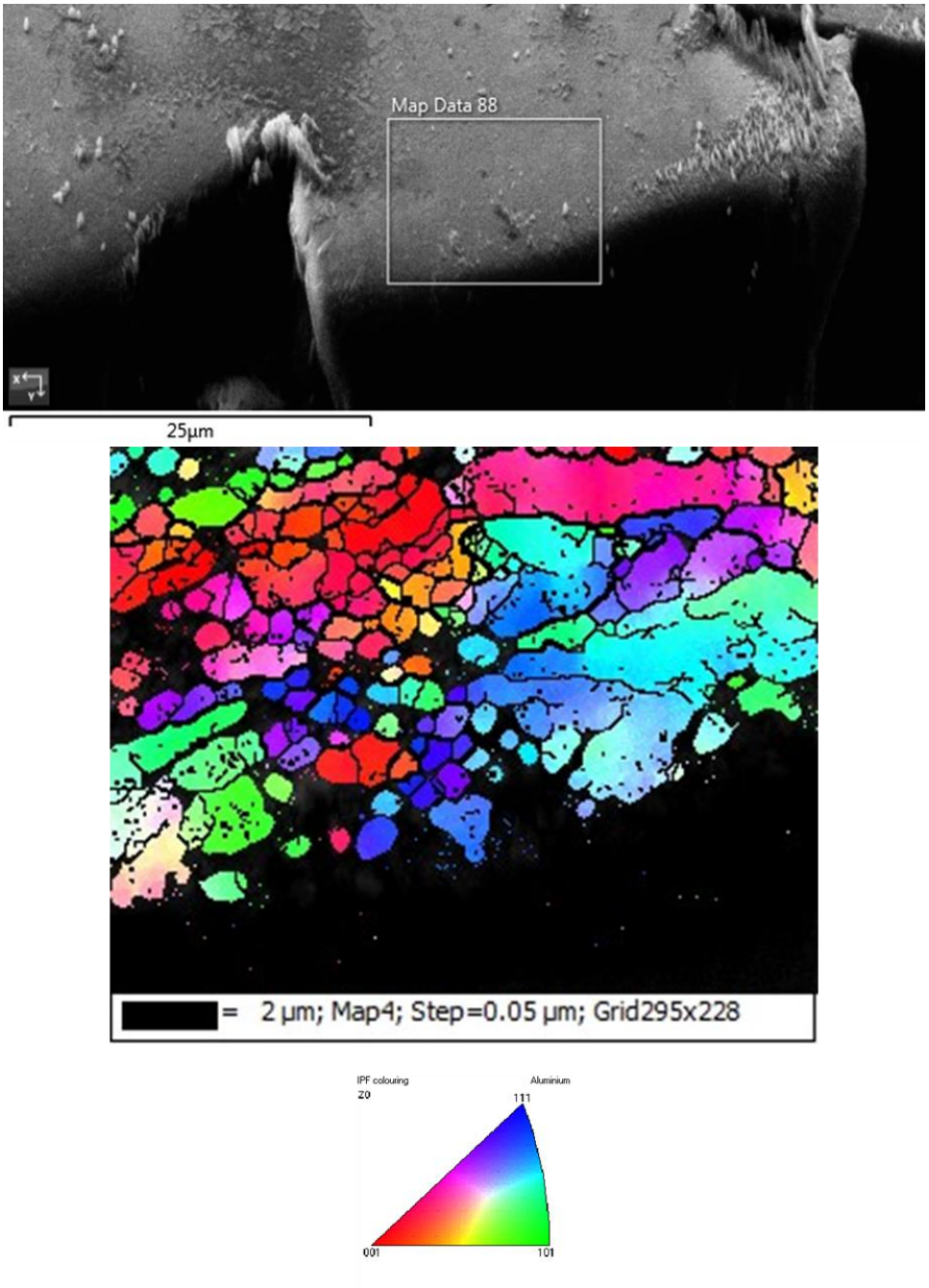

Figure 60 Top image shows the fracture surface edge of the 100 hr sample in SE mode. EBSD maps along the primary crack shown below suggest the microstructure is HDR and MDR.

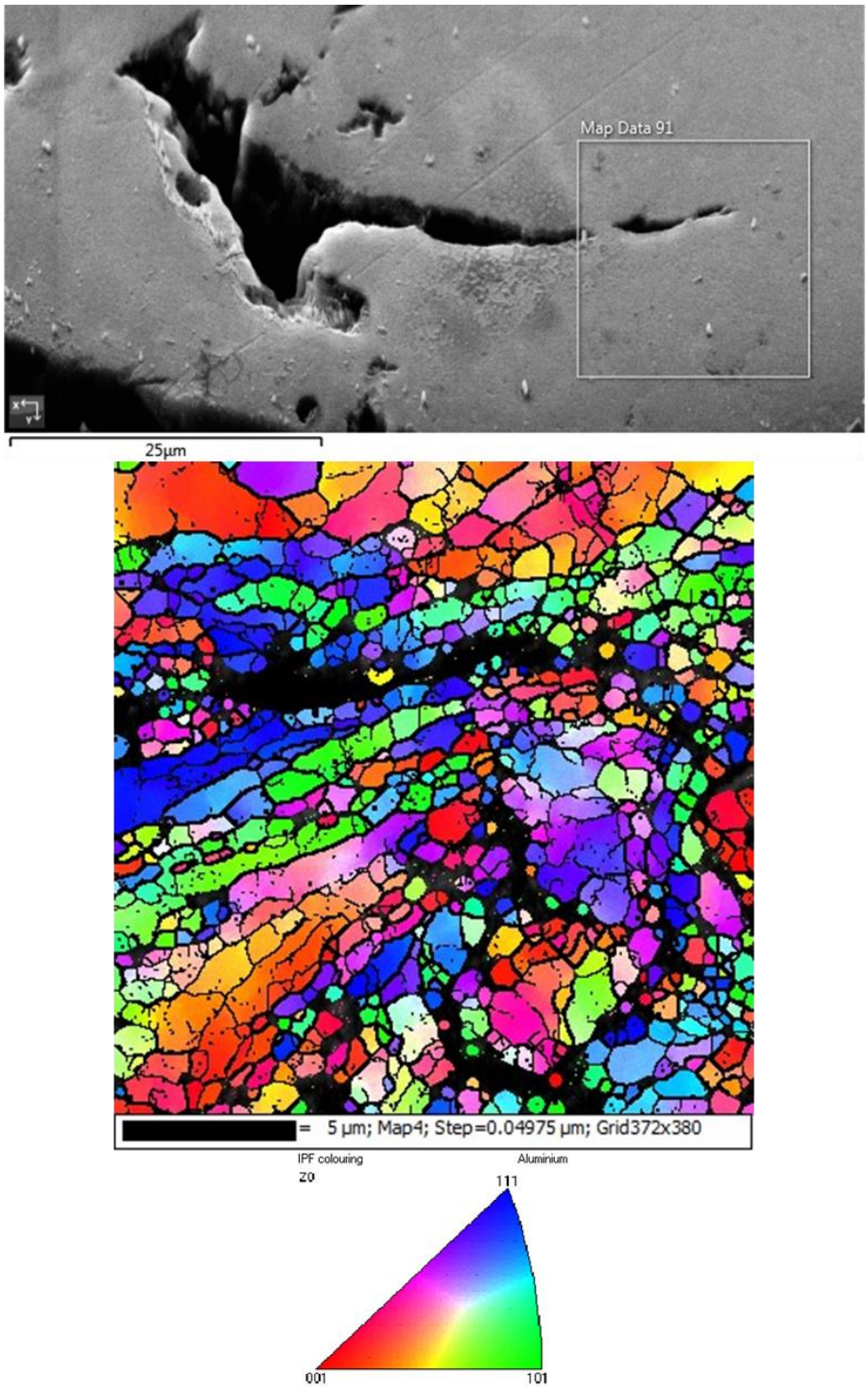

Figure 61 SE SEM images of site 3 for the 100 hr sample captures an entire tertiary crack just beneath the primary crack. The EBSD map below shows the tertiary crack propagating through the HDR within the IDR.

Chapter 5: Conclusions and Future Work

Low temperature HT of the bulk CS components allowed for some degree of recrystallization, and possible changes in diffusion bonding between previously unfused particles which can be seen through the microstructural evolution of the bulk material in metallographically processed samples, and changes in fracture behavior. Entrained oxides and intermetallics were observed to be distributed in plane between deformed regions in the IDR which are believed to pin grain boundaries and inhibit grain growth, preserving the morphology of the IDR during low temperature heat treatment. Low temperature HT increases the amount of ductile fracture features seen in the fracture surface imaging which should translate directly to improved tensile properties.

The fracture surface for all samples displays characteristic butte-like structures with complex geometry's often exhibiting evidence multiple failure mechanisms. The microstructure underneath the butte-like structures seen throughout the fracture surface seem to be associated with the IDR as morphologically similar fracture features indexed show the presence of MDR and HDR regions. Propagation through these complex 3-D areas within the bulk lead to the characteristic stepping seen in the fracture surface as the crack navigates its way through the IDR along the path which exhibits the smallest average grain size. This is supported by the indexing of secondary crack which show preferential formation within the smallest grain regime available. Cracks within the bulk CS material seem to propagate through the IDR where material

is pushed or essentially extruded between previously deposited particles. Tertiary cracking confirms that crack propagation within the bulk appears to concentrate in the areas within the smallest grain regime and more specifically between areas which exhibit the smallest diameters.

Nano-Indention or atomic force microscopy techniques would be more useful in quantifying the actual hardness of the IDR. The size and depth of the areas within the bulk microstructure are too fine for traditional micro-hardness. Initial investigation into quantifying the surface area fraction of microhardness indents show that for statistically valid measurements of microhardness large sample sizes should be used as differences in hardness per grain regime are approximately 10%.

It is theorized from the observed effects of low temperature heat treatment that the application of traditional powder metallurgy processing techniques such a sintering, could facilitate further diffusion bonding between impinged powder particles. Improved interparticle bonding should increase the possibility of enhanced mechanical properties. The resulting bulk components created from joining similar materials can exhibit little to no bond line and failure appears in the bulk rather than trans-granularly or along the bond line [70]. Further studies of higher temperature a longer duration heat treatments could better elucidate these phenomena.

References

[1] A. Papyrin *et al*, *Cold Spray Technology.* 2007Available: https://ebookcentral.proquest.com/lib/[SITE_ID]/detail.action?docID=281984.

[2] J. Villafuerte, *Modern Cold Spray.* 2015.

[3] V. K. Champagne, *The Cold Spray Materials Deposition Process : Fundamentals and Applications.* 2007Available: https://ebookcentral.proquest.com/lib/[SITE_ID]/detail.action?docID=1639744.

[4] D. Goldbaum, "Micromechanical Testing of Cold Sprayed Ti Splats and Coatings." , McGill University, 2012.

[5] Ferguson B. Lynn *et al*, "A through-process model for cold sprayed aluminum alloys," in June 16, 2014, pp. 1.

[6] W. D. Callister and D. G. Rethwisch, *Materials Science and Engineering.* (9th edition ed.) Hoboken, NJ: Wiley, 2014.

[7] D. R. Askeland and W. J. Wright, *Theœ Science and Engineering of Materials.* (7. ed., SI ed.) Boston, Mass: Cengage Learning, 2016.

[8] M. A. Meyers and K. K. Chawla, *Mechanical Behavior of Materials.* Cambridge: Cambridge University Press, 2008.

[9] DOD, "Department of Defense (DOD) Manufacturing Process Standard Documents," *Manufacturing Process Standards,* Apr 24, 2015.

[10] DOD, "Detail Specification Aluminum-Based Powders for Cold Spray Deposition," *A Dictionary of Mechanical Engineering,* May 12, 2014.

[11] F. Meng, S. Yue and J. Song, "Quantitative prediction of critical velocity and deposition efficiency in cold-spray: A finite-element study," *Scripta Materialia,* vol. 107, pp. 83-87, 2015. Available: http://dx.doi.org/10.1016/j.scriptamat.2015.05.026. DOI: 10.1016/j.scriptamat.2015.05.026.

[12] M. Grujicic *et al*, "Adiabatic shear instability based mechanism for particles/substrate bonding in the cold-gas dynamic-spray process," *Materials and Design,* vol. 25, *(8),* pp. 681-688,

2004. Available: https://www.sciencedirect.com/science/article/pii/S026130690400069X. DOI: 10.1016/j.matdes.2004.03.008.

[13] H. Assadi *et al*, "Bonding mechanism in cold gas spraying," *Acta Materialia,* vol. 51, *(15),* pp. 4379-4394, 2003. Available: https://www.sciencedirect.com/science/article/pii/S135964540300274X. DOI: 10.1016/S1359-6454(03)00274-X.

[14] (1 April). *The International Traffic in Arms Regulations (ITAR)*. Available: https://www.pmddtc.state.gov/?id=ddtc_kb_article_page&sys_id=%2024d528fddbfc930044f9ff621f961987.

[15] T. Stoltenhoff, H. Kreye and H. Richter, "An analysis of the cold spray process and its coatings," *J Therm Spray Tech,* vol. 11, *(4),* pp. 542-550, 2001. Available: https://search.proquest.com/docview/233453400. DOI: 10.1361/105996302770348682.

[16] D. Wolfe *et al*, "Investigation and characterization of Cr3C2-based wear-resistant coatings applied by the cold spray process," *J Therm Spray Tech,* vol. 15, *(3),* pp. 400-412, 2006. . DOI: 10.1361/105996306X124400.

[17] V. K. Champagne and D. J. Helfritch, "A demonstration of the antimicrobial effectiveness of various copper surfaces," *Journal of Biological Engineering,* vol. 7, *(1),* pp. 8, 2013. Available: https://www.ncbi.nlm.nih.gov/pubmed/23537176. DOI: 10.1186/1754-1611-7-8.

[18] J. Karthikeyan, "4 - the advantages and disadvantages of the cold spray coating process," in *The Cold Spray Materials Deposition Process*Anonymous Elsevier Ltd, 2007, pp. 62-71.

[19] S. Klinkov and V. Kosarev, "Measurements of cold spray deposition efficiency," *J Therm Spray Tech,* vol. 15, *(3),* pp. 364-371, 2006. Available: https://search.proquest.com/docview/875623569. DOI: 10.1361/105996306X124365.

[20] K. Ogawa and D. Seo, "Repair of Turbine Blades Using Cold Spray Technique," 2011. Available: https://www.openaire.eu/search/publication?articleId=intech_____::023d8fafb44e0dbb4497fb8129024860.

[21] H. Assadi *et al*, "Cold spraying A materials perspective," *Acta Materialia,* June 27, 2016.

[22] T. Schmidt *et al*, "Development of a generalized parameter window for cold spray deposition," *Acta Materialia,* vol. 54, *(3),* pp. 729-742, 2005. Available: https://www.sciencedirect.com/science/article/pii/S1359645405005975. DOI: 10.1016/j.actamat.2005.10.005.

[23] M. Rokni, C. Widener and V. Champagne, "Microstructural Evolution of 6061 Aluminum Gas-Atomized Powder and High-Pressure Cold-Sprayed Deposition," *J Therm Spray Tech,* vol. 23, *(3),* pp. 514-524, 2013. . DOI: 10.1007/s11666-013-0049-y.

[24] A. Heidarzadeh and T. Saeid, "Correlation between process parameters, grain size and hardness of friction-stir-welded Cu–Zn alloys," *Rare Metals,* vol. 37, *(5),* pp. 388-398, 2018. Available: https://search.proquest.com/docview/2030106500. DOI: 10.1007/s12598-016-0704-9.

[25] F. M. White, *Fluid Mechanics.* (Seventh edition ed.) 2011.

[26] S. V. Falkovich, "On the theory of the laval nozzle," National Advisory Committee for Aeronautics, AFMDC Technical Library, Tech. Rep. 10, April 1,. 1946.

[27] J. R. Davis, *Handbook of Thermal Spray Technology.* (1. printing ed.) 2004.

[28] V. K. Champagne, *The Cold Spray Materials Deposition Process.* (1. publ. ed.) Cambridge: Woodhead, 2007.

[29] D. Helfritch and V. Champagne U.S. Army Research Laboratory, Aberdeen Proving Ground, MD, "Optimal Particle Size for the Cold Spray Process," *Thermal Spray 2006: Science, Innovation, and Application (ASM International),* pp. 103-107, 2006.

[30] X. Ning, J. Jang and H. Kim, "The effects of powder properties on in-flight particle velocity and deposition process during low pressure cold spray process," *Applied Surface Science,* vol. 253, *(18),* pp. 7449-7455, 2007. Available: http://dx.doi.org.dax.lib.unf.edu/10.1016/j.apsusc.2007.03.031. DOI: 10.1016/j.apsusc.2007.03.031.

[31] W. Wong *et al*, "Effect of Particle Morphology and Size Distribution on Cold-Sprayed Pure Titanium Coatings," *J Therm Spray Tech,* vol. 22, *(7),* pp. 1140-1153, 2013. . DOI: 10.1007/s11666-013-9951-6.

[32] D. Helfritch and V. Champagne, "A model study of powder particle size effects in cold spray deposition," Dec. 1,. 2008.

[33] C. Cushway, "The Microstructural Annealing Response of Cold Gas Dynamically Sprayed Al 6061 " unpublished.

[34] B. Crossland, "The Development of Explosive Welding and its Application in Engineering," *Metals and Materials,* vol. 9, pp. 401-403, 1971.

[35] W. Li, C. Li and H. Liao, "Significant influence of particle surface oxidation on deposition efficiency, interface microstructure and adhesive strength of cold-sprayed copper coatings," *Applied Surface Science,* vol. 256, *(16),* pp. 4953-4958, 2010. Available: http://dx.doi.org/10.1016/j.apsusc.2010.03.008. DOI: 10.1016/j.apsusc.2010.03.008.

[36] Christine Borchers *et al*, "Formation of persistent dislocation loops by ultra-high strain-rate deformation during cold spraying," *Acta Materialia,* April 19, 2005.

[37] G. P. Dinda, H. Rösner and G. Wilde, "Synthesis of bulk nanostructured materials by repeated cold-rolling," *Materials Science & Engineering A,* vol. 410, pp. 328-331, 2005. Available: https://www.sciencedirect.com/science/article/pii/S0921509305008610. DOI: 10.1016/j.msea.2005.08.091.

[38] M. Rokni, C. Widener and V. Champagne, "Microstructural Evolution of 6061 Aluminum Gas-Atomized Powder and High-Pressure Cold-Sprayed Deposition," *J Therm Spray Tech,* vol. 23, *(3),* pp. 514-524, 2014. . DOI: 10.1007/s11666-013-0049-y.

[39] P. Nautiyal *et al*, "In situ mechanical investigation of the deformation of splat interfaces in cold sprayed aluminum alloy," *Materials Science & Engineering A,* 2018.

[40] P. C. King, S. H. Zahiri and M. Jahedi, "Focused ion beam micro-dissection of cold-sprayed particles," *Acta Materialia,* vol. 56, *(19),* pp. 5617-5626, 2008. Available: https://www.sciencedirect.com/science/article/pii/S1359645408005338. DOI: 10.1016/j.actamat.2008.07.034.

[41] K. Kim *et al*, "Grain refinement in a single titanium powder particle impactedat high velocity," *Scripta Materialia,* pp. 768-771, 2008.

[42] B. Han *et al*, "Deformation behavior of bimodal nanostructured 5083 Al alloys," *Metall and Mat Trans A,* vol. 36, *(4),* pp. 957-965, 2005. Available: https://search.proquest.com/docview/213744706. DOI: 10.1007/s11661-005-0289-7.

[43] F. C. Liu and Z. Y. Ma, "Contribution of grain boundary sliding in low-temperature superplasticity of ultrafine-grained aluminum alloys," *Scripta Materialia,* vol. 62, *(3),* pp. 125-128, 2009. Available: https://www.sciencedirect.com/science/article/pii/S1359646209006411. DOI: 10.1016/j.scriptamat.2009.10.010.

[44] Y. H. Zhao *et al*, "Mechanical behavior, deformation mechanism and microstructure evolutions of ultrafine grained Al during recovery via annealing," *Materials Science & Engineering A,* Nov 21, 2019.

[45] A. P. Zhilyaev *et al*, "Influence of ECAP processing parameters on texture and microstructure of commercially pure aluminum," *Materials Science & Engineering A,* vol. 441, *(1),* pp. 245-252,

2006. Available: https://www.sciencedirect.com/science/article/pii/S0921509306017448. DOI: 10.1016/j.msea.2006.08.029.

[46] B. Newbury and M. Notis, "The history and evolution of wiredrawing techniques," *Jom,* vol. 56, *(2),* pp. 33-37, 2004. Available: https://search.proquest.com/docview/232570342. DOI: 10.1007/s11837-004-0142-2.

[47] M. Merklein *et al*, "Bulk forming of sheet metal," *CIRP Annals - Manufacturing Technology,* vol. 61, *(2),* pp. 725-745, 2012. Available: https://www.sciencedirect.com/science/article/pii/S0007850612002065. DOI: 10.1016/j.cirp.2012.05.007.

[48] Z. C. Cordero, B. E. Knight and C. A. Schuh, "Six decades of the Hall-Petch effect - a survey of grain-size strengthening studies on pure metals," *International Materials Reviews,* vol. 61, *(8),* pp. 495-512, 2016. Available: http://www.tandfonline.com/doi/abs/10.1080/09506608.2016.1191808. DOI: 10.1080/09506608.2016.1191808.

[49] C. S. Pande and K. P. Cooper, "Nanomechanics of Hall–Petch relationship in nanocrystalline materials," *Progress in Materials Science,* vol. 54, *(6),* pp. 689-706, 2009. Available: https://www.sciencedirect.com/science/article/pii/S0079642509000206. DOI: 10.1016/j.pmatsci.2009.03.008.

[50] M. A. Haque and M. T. A Saif, "Mechanical behavior of 30–50 nm thick aluminum films under uniaxial tension," *Scripta Materialia,* vol. 47, *(12),* pp. 863-867, 2002. Available: https://www.sciencedirect.com/science/article/pii/S1359646202003068. DOI: 10.1016/S1359-6462(02)00306-8.

[51] S. H. Whang, *Nanostructured Metals and Alloys.* (1. publ. ed.) Oxford [u.a.]: Woodhead, 2011.

[52] C. E. Carlton and P. J. Ferreira, "What is behind the inverse Hall–Petch effect in nanocrystalline materials?" *Acta Materialia,* vol. 55, *(11),* pp. 3749-3756, 2007. Available: https://www.sciencedirect.com/science/article/pii/S1359645407001590. DOI: 10.1016/j.actamat.2007.02.021.

[53] C. M. Hefferan *et al*, "Observation of recovery and recrystallization in high-purity aluminum measured with forward modeling analysis of high-energy diffraction microscopy," *Acta Materialia,* vol. 60, *(10),* pp. 4311-4318, 2012. Available: https://www.sciencedirect.com/science/article/pii/S1359645412002765. DOI: 10.1016/j.actamat.2012.04.020.

[54] B. A. Bedard *et al*, "Microstructure and Micromechanical Response in Gas-Atomized Al 6061 Alloy Powder and Cold-Sprayed Splats," *Journal of Thermal Spray Technology,* vol. 27, *(8),* pp. 1563-1578, 2018. . DOI: 10.1007/s11666-018-0785-0.

[55] F. Khodabakhshi *et al*, "Hardness−strength relationships in fine and ultra-fine grained metals processed through constrained groove pressing," *Materials Science & Engineering A,* vol. 636, pp. 331-339, 2015. Available: https://www.sciencedirect.com/science/article/pii/S0921509315003846. DOI: 10.1016/j.msea.2015.03.122.

[56] P. D. Eason *et al*, "On the characterization of bulk copper produced by cold gas dynamic spray processing in as fabricated and annealed conditions," *Materials Science & Engineering A,* vol. 528, *(28),* pp. 8174-8178, 2011. Available: http://dx.doi.org/10.1016/j.msea.2011.07.012. DOI: 10.1016/j.msea.2011.07.012.

[57] J. Lubliner, *Plasticity Theory.* 2008Available: https://books.google.com/books?id=MkK-BLbHtcAC.

[58] K. Spencer, D. M. Fabijanic and M. X. Zhang, "The use of Al–Al2O3 cold spray coatings to improve the surface properties of magnesium alloys," *Surface & Coating Technology,* Aug. 3, 2009.

[59] J. Dunkley, "Blown to atoms: how to make metal powders," *Metal Powder Report,* vol. 57, pp. 18-19, Nov. 1,. 2002.

[60] R. L. Fullman, "Metal interfaces," *American Society for Metals, Metals Park, OH,* 1952.

[61] C. Walde *et al*, "Characterizing the Effect of Thermal Processing on Feedstock Al Alloy Powder for Additive Manufacturing Applications," *Journal of Materials Engineering and Performance,* vol. 28, *(2),* pp. 601-610, 2018. . DOI: 10.1007/s11665-018-3550-0.

[62] L. Ratke and P. W. Voorhees, *Growth and Coarsening.* Berlin/Heidelberg: Springer Berlin Heidelberg, 2002.

[63] M. R. Rokni *et al*, "An investigation into microstructure and mechanical properties of cold sprayed 7075 Al deposition," *Materials Science & Engineering A,* vol. 625, pp. 19-27, 2015. Available: https://www.sciencedirect.com/science/article/pii/S0921509314014270. DOI: 10.1016/j.msea.2014.11.059.

[64] C. J. Kuehmann and P. W. Voorhees, "Ostwald ripening in ternary alloys," *Metallurgical and Materials Transactions A,* vol. 27, *(4),* pp. 937-943, 1996. Available: https://www.osti.gov/biblio/250721. DOI: 10.1007/BF02649761.

[65] P. W. Voorhees, "The theory of Ostwald ripening," *Journal of Statistical Physics,* vol. 38, *(1-2),* pp. 231-252, 1985. . DOI: 10.1007/BF01017860.

[66] B. Ivanskii and R. Vengrenovich, "To the theory of Ostwald ripening in metallic alloys," *Phys. Metals Metallogr,* vol. 117, *(8),* pp. 756-765, 2016. Available: https://search-proquest-com.dax.lib.unf.edu/docview/1813209282. DOI: 10.1134/S0031918X16080044.

[67] M. R. Rokni *et al*, "Microstructure and mechanical properties of cold sprayed 7075 deposition during non isothermal annealing," *Surface & Coating Technology,* 2015.

[68] M. R. Rockni, C. A. Widener and V. R. Champagne, "Microstructural stability of ultra fine grained coldsprayed 6061aluminum alloy," *Applied Surface Science,* Dec 1, 2013.

[69] R. E. Reed-Hill and R. Abbaschian, *Physical Metallurgy Principles.* (3. ed. ed.) 1992.

[70] T. Shimatsu and M. Uomoto, "Atomic diffusion bonding of wafers with thin nanocrystalline metal films," *Journal of Vacuum Science & Technology B: Microelectronics and Nanometer Structures,* vol. 28, *(4),* pp. 706-714, 2010. Available: http://dx.doi.org/10.1116/1.3437515. DOI: 10.1116/1.3437515.

[71] Anonymous *Powder Metallurgy.* (2nd ed.) Materials Park, OH: ASM International, 2017.

[72] Z. X. Guo and N. Ridley, "Modelling of diffusion bonding of metals," *Materials Science and Technology,* vol. 3, *(11),* pp. 945-953, 1987. . DOI: 10.1179/026708387790221035.

[73] (13 June). *The Development of Cold Spray towards the Next Generation of Additive Manufacturing*. Available: https://www.tcd.ie/mecheng/research/stam/research/projects/current/cold-spray.php.

[74] S. Avner, *Introduction to Pyhsical Mettallurgy.* McGraw Hill, .

[75] M. De Graef and M. E. McHenry, *Structure of Materials.* 2012Available: https://ebookcentral.proquest.com/lib/[SITE_ID]/detail.action?docID=989092.

[76] W. Becker and R. Shipley, *ASM Handbook Volume 11: Failure Analysis and Prevention* . (1st ed.) 2002Available: http://10.11.35.11:4599/catchpage/URL.jsp?BID=40785864.

[77] W. Becker, "PRINCIPLES OF FAILURE ANALYSIS Ductile and Brittle Fracture," *ASM International,* 2002.